12-14-2018 1:00 PM

# The mitochondrial calcium uniporter regulator 1 (MCUR1) matrix domain is a self-associated multimer sensitive to divalent cations

Naveed Siddiqui
*The University of Western Ontario*

Supervisor
Stathopulos, Peter B.
*The University of Western Ontario*

Graduate Program in Physiology and Pharmacology
A thesis submitted in partial fulfillment of the requirements for the degree in Master of Science

## Recommended Citation

Siddiqui, Naveed, "The mitochondrial calcium uniporter regulator 1 (MCUR1) matrix domain is a self-associated multimer sensitive to divalent cations" (2018). *Electronic Thesis and Dissertation Repository*. 5912.
https://ir.lib.uwo.ca/etd/5912

# Abstract

Mitochondria are primarily appreciated for the generation of adenosine triphosphate (ATP), a chemical store of energy required by all cells. These organelles, however, also play key roles in apoptosis, autophagy and shaping cytosolic calcium ($Ca^{2+}$) signaling via $Ca^{2+}$ uptake into the mitochondrial matrix. This $Ca^{2+}$ uptake is mediated chiefly via the mitochondrial $Ca^{2+}$ uniporter (MCU), an inner mitochondrial membrane protein that oligomerizes to form a $Ca^{2+}$ selective pore. MCU is regulated by several protein binding partners, including the recently identified MCU regulator-1 (MCUR1). MCUR1 stabilizes a higher order MCU heterocomplex through interactions with MCU and other protein regulators. I hypothesize that the evolutionarily conserved matrix region of MCUR1 contains domains vital for protein and ion interactions which regulate MCU complex formation and function. My biophysical characterization of the MCUR1 matrix domain which includes the coiled-coil domains (i.e. residues 161-338) revealed that this conserved region forms a highly $\alpha$-helical and self-associated multimer that is conformationally sensitive to divalent cations. Additionally, my solution nuclear magnetic resonance spectroscopy-driven structural elucidation of the MCUR1 matrix region which excludes the coiled-coil domains (i.e. residues 161-209) revealed that this region of MCUR1 forms a compact triple helix which is structurally homologous to the HdeB acid stress chaperone protein despite very low sequence identity. These findings represent the first structural data on MCUR1 and provide a strong framework for future functional studies to assess the significance of MCUR1 oligomerization and ion sensitivity on MCU heterocomplex assembly and activity which has been implicated in numerous cancers as well as metabolic, neurodegenerative and cardiovascular disorders.

# Keywords

Mitochondrial calcium uniporter regulator 1, solution nuclear magnetic resonance spectroscopy, structure, stability, coiled coils, oligomerization, divalent cation sensitivity.

# Acknowledgments

First and foremost, I would like to thank and appreciate the guidance and support granted to me by my supervisor Dr. Peter B. Stathopulos. His vast knowledge and strong grasp over the field of structural biology and biochemistry has been an incredible source of assistance and advancement throughout my master's program. His encouraging feedback and patience have allowed me to gain command over numerous laboratory techniques and strengthen my critical thinking abilities. I am also grateful for his undue support and encouragement towards the production of academic literature and oral presentations that have greatly enhanced my communication and writing skills. Furthermore, I would like to acknowledge my esteemed committee members, Dr. Donglin Bai, Dr. Nica Borradaile, and Dr. Murray Junop, for their availability and the provision of critical feedback towards my project.

Additionally, I want to strongly appreciate the technical assistance provided by Lee-Ann Brier, facility manager at the Biomolecular Interactions and Conformations Facility, and Dr. Liliana Santamaria, facility manager at the Biomolecular NMR facility. Their strong practical knowledge and considerate nature was essential for the timely collection of data.

Furthermore, I cannot discount the contribution of the past and present members of the Dr. Stathopulos lab: Jinhui Zhu, Steve Chung, Matthew Novello, Tom Lin, Allen Feng, Rachel Lee, Vickie Hung, and MengQi Zhang. It was a pleasure to have the support of and spend time with such immensely talented and warmhearted individuals. I would also like to thank the lab volunteers Shilpa Jyothi Kumar and Ryan Park for all their assistance in protein purification protocols that greatly increased the efficiency and productivity of my work by allowing me to focus on other areas of research.

Lastly, I want to thank my family for their unwavering support and encouragement throughout my life. Their love and trust has always provided me the strength to tackle any obstacle and encouraged me towards constant self-development.

# Table of Contents

# List of Tables

# List of Figures

# List of Abbreviations

| | |
|---|---|
| [$Ca^{2+}$] | $Ca^{2+}$ concentration |
| 3D | three dimensional |
| AIF | apoptosis inducing factor |
| ANS | 8-anilinonapthalene-1-sulfonic acid |
| ARC | arachidonic acid activated channels |
| ATP | adenosine triphosphate |
| BME | β-mercaptoethanol |
| BSA | bovine serum albumin |
| $Ca^{2+}$ | calcium ions |
| CaM | calmodulin |
| CaMKII | $Ca^{2+}$/CaM-dependent kinase II |
| CARA | computer aided resonance assignment |
| CC1/CC2 | coiled coil-1/coiled coil-2 |
| CCDC109A | coiled coil domain containing 109A |
| CD | circular dichroism |
| CRAC | $Ca^{2+}$-release activated channels |
| Cryo-EM | cryo-electron microscopy |
| CypD | cyclophilin D |
| DAG | diacylglycerol |
| DSS | 4,4-dimethyl-4-silapentane-1-sulfonic acid |
| DTT | dithiothreitol |
| EB | ethidium bromide |
| EDTA | ethylene diamine tetra acetic acid |
| EMRE | essential MCU regulator |
| SILAC | stable isotope labelling by amino acids in cell culture |
| ER | endoplasmic reticulum |
| FPLC | Fast Purification Liquid Chromatography |
| GFP | green fluorescent protein |
| HCC | hepatocellular carcinomas |
| HCX | $H^+$/$Ca^{2+}$ exchangers |

| | |
|---|---|
| HSQC | $^1$H-$^{15}$N-heteronuclear single quantum coherence |
| IMM | inner mitochondrial membrane |
| IMS | inner membrane space |
| $IP_3$ | inositol-1,4,5-trisphosphate |
| $IP_3R$ | inositol-1,4,5-trisphosphate receptors |
| IPTG | isopropyl β-D-1-thiogalactopyranoside |
| LB | Luria-Bertani broth |
| LETM1 | leucine zipper EF-hand-containing transmembrane protein 1 |
| MALS | multi-angle light scattering |
| MAM | mitochondria-associated membrane |
| MCU | mitochondrial calcium uniporter |
| MCUR1 | MCU regulator 1 |
| MICU1 | mitochondrial calcium uptake 1 |
| MOPS | n-morpholino propanesulfonic acid |
| mPTP | mitochondrial permeability transition por |
| MRE | mean residue ellipticity |
| MTSL | 1-oxyl-2,2,5,5-tetramethyl-Δ3-pyrroline-3-methyl methanethiosulfonate |
| NCX | $Na^+/Ca^{2+}$ exchanger |
| NFkB | nuclear factor kappa B |
| Ni-NTA | nickel-nitrilotriacetic acid |
| NMDA | N-methyl-D-aspartate |
| NMR | nuclear magnetic resonance |
| NOE | nuclear Overhauser effect |
| $OD_{600}$ | optical density at 600 nm |
| OMM | outer mitochondrial membrane |
| PCR | polymerase chain reaction |
| PKA | protein kinase A |
| PKC | protein kinase C |
| PKG | cGMP-dependent protein kinase |
| PLC | phospholipase C |
| PMCA | plasma membrane $Ca^{2+}$-ATPases |
| PMT | photomultiplier tube |

| | |
|---|---|
| PRE | paramagnetic relaxation enhancement |
| RMSD | root mean square deviation |
| RNAi | RNA interference |
| ROC | receptor operated channels |
| ROS | reactive oxygen species |
| RuR | ruthenium red |
| RyR | ryanodine receptor |
| $S^2$ | smaller order parameters |
| SEC | size-exclusion gel chromatography |
| SERCA | sarcoendoplasmic reticulum $Ca^{2+}$ ATPase |
| siRNA | small interfering RNA |
| SMAC | second mitochondria derived activator of caspase |
| SMOC | second messenger operated channels |
| SOC | store operated calcium channels |
| SOCE | store operated $Ca^{2+}$ entry |
| SR | sarcoplasmic reticulum |
| STIM | stromal interaction molecule |
| $T_m$ | midpoint of temperature denaturation |
| TRP | transient receptor potential |
| VDAC | voltage dependent anion channel |
| VOC | voltage operated channels |

# Chapter 1

# 1 Introduction

## 1.1 Calcium signaling

Cellular signaling pathways are essential for cells to adapt and respond to the constantly changing environmental cues around them. Apart from being an important mineral for healthy bone development in our body, calcium ions ($Ca^{2+}$) also play an integral role as one of the chief signaling messengers in our cells. The spatiotemporal regulation of intracellular $Ca^{2+}$ levels govern numerous cellular processes ranging from cell growth and proliferation to cell death and apoptosis. This versatility of $Ca^{2+}$ signaling is primarily achieved by the presence of numerous proteins that form the $Ca^{2+}$-signaling toolkit consisting of receptors, transducers, effectors, channels, pumps, and exchangers (Berridge et al., 2003). To add to this versatility, both the duration and frequency of $Ca^{2+}$ oscillations in the cytosol can dictate the precise effect on cellular processes. This specificity can be seen during the gene expression driven by proinflammatory transcription factors. In one study, the rapid oscillation frequency of $Ca^{2+}$ led to the activation of three proinflammatory transcription factors whereas infrequent oscillations only led to the activation of Nuclear factor kappa B (NFκB) (Dolmetsch et al., 1998). While processes such as transcription and fertilization depend on longer durations of cytosolic $Ca^{2+}$ increases ranging from minutes to hours, many other processes respond to $Ca^{2+}$ oscillations within ms to μs. Neurotransmitter release at the small dendrites and spine is one such example of fast $Ca^{2+}$ signaling where a single action potential can raise the $Ca^{2+}$ concentration ($[Ca^{2+}]$) to ~1.5 μM within a few ms (Sabatini et al., 2002), leading to exocytosis of the presynaptic vesicles.

Additionally, $Ca^{2+}$ may bind to numerous sensory adaptor proteins that can activate further signaling pathways. Calmodulin (CaM) is one of the main ubiquitously expressed adaptor proteins that senses changes in $Ca^{2+}$ levels and facilitates signal transduction by interactions with a wide range of target proteins. Binding of $Ca^{2+}$ causes conformational changes in the CaM domains which promotes interactions with targets and activation through numerous mechanisms, including the relieving of protein autoinhibition, restructuring of protein/enzyme active sites, and regulation of protein-protein interactions, to name a few (Hoeflich & Ikura, 2002). More specifically, CaM contains two homologous domains connected via a flexible linker. Upon $Ca^{2+}$ binding to the EF-hand domains, the interhelical angles of the EF-hand motifs adopt an 'open' conformation, exposing the hydrophobic regions which can then interact with target proteins (Barbato et al., 1992). Interestingly, the binding affinity of $Ca^{2+}$ to CaM is not only dependent on the direct interaction with the EF-hand domains, but is also enhanced indirectly upon CaM interactions with target proteins (Clapham, 2007).

## 1.2 $Ca^{2+}$ entry, regulation and storage

Numerous cellular processes rely on $Ca^{2+}$ signaling, making the tight regulation of cytosolic $Ca^{2+}$ concentration ($[Ca^{2+}]$) essential for preventing any unregulated downstream signaling. At rest, cytosolic $[Ca^{2+}]$ is approximately 100 nM, roughly four orders of magnitude lower than that of the extracellular space which is maintained at ~1 mM (Rizzuto & Pozzan, 2006). This steep gradient is established primarily by the action of plasma membrane $Ca^{2+}$-ATPases (PMCA) and $Na^{2+}/Ca^{2+}$ exchangers (NCX). PMCAs require adenosine triphosphate (ATP) hydrolysis to export $Ca^{2+}$ ions across the plasma membrane in a 1:1 ratio, whereas NCXs utilize the electrochemical gradient of $Na^{+}$ to extrude 1× $Ca^{2+}$ for every 3× $Na^{+}$ ions (Carafoli, 1987; Hao et al., 1994; Palty et al., 2004). Intracellular storage organelles also complement this process during elevated cytoplasmic $[Ca^{2+}]$ via the action of sarcoendoplasmic reticulum $Ca^{2+}$-ATPase (SERCA), which actively moves 2× $Ca^{2+}$ ions per ATP hydrolysis into the endoplasmic/sarcoplasmic reticulum (ER/SR) $Ca^{2+}$ stores, and via the mitochondrial calcium uniporter (MCU) complex which moves $Ca^{2+}$ into the mitochondrial matrix (Bagur & Hajnoczky, 2017; Tanford, 1982). The ER (or SR) function as the main storage organelle for $Ca^{2+}$ inside the cell and can accumulate upwards of 0.1 – 0.5 mM $[Ca^{2+}]$ (Bagur & Hajnoczky, 2017). Additionally, mitochondrial matrix $[Ca^{2+}]$ mimics that of the cytosol during rest; however, upon stimulation, matrix $[Ca^{2+}]$ can rise significantly, exceeding 100 μM in certain cell types (Montero et al., 2000). The mitochondrial matrix

[$Ca^{2+}$] in histamine-stimulated HeLa cells was shown to range from ~20-50 μM (Montero et al., 2002; Pinton et al., 2004).

The initiation of $Ca^{2+}$ signaling can occur in response to external or internal cues which lead to a rise in cytosolic [$Ca^{2+}$]. For example, the presence of a large electrochemical gradient across the plasma membrane allows external $Ca^{2+}$ to be brought in rapidly via a wide variety of channels, each with distinct properties. The most well studied of these channels are the voltage operated channels (VOCs) present primarily in excitable cells that facilitate very rapid $Ca^{2+}$ influx necessary for processes such as muscle contraction and exocytosis of the synaptic vesicles (Berridge et al., 2003). Other channels include the receptor operated channels (ROCs) such as N-methyl-D-aspartate (NMDA) receptors that respond to external stimuli such as glutamate, and second messenger operated channels (SMOCs) such as arachidonic acid activated channels (ARC) that are activated upon binding of intracellular messengers (Berridge et al., 2003). Other less well-defined entry pathways that are not specific to $Ca^{2+}$ include the large family of transient receptor potential (TRP) ion channels, which are mostly activated by environmental cues such as temperature, pressure, and pH changes. (Berridge et al., 2000). Another channel type that has been the focus of intensive research are the store operated calcium channels (SOCs). As suggested by the name, SOCs sense and respond to the lowering of stored ER luminal [$Ca^{2+}$]. SOC activity is coupled indirectly to the function of inositol-1,4,5-trisphosphate receptors ($IP_3R$) found on the ER.

Release of intracellular stored $Ca^{2+}$ located in the ER or SR is primarily regulated by two ROCs, the $IP_3R$ and ryanodine receptor (RyR) families. The activity of these channels are also regulated by multiple factors present on either the luminal or cytosolic surface of the channel (Berridge et al., 2003). In the case of $IP_3R$ regulation, the main determinants of channel open probability are inositol-1,4,5-trisphosphate ($IP_3$) and $Ca^{2+}$. The production of $IP_3$ occurs at the cell membrane where a ligand binding to a cell surface receptor, G-protein-coupled or receptor tyrosine kinase, for example, leads to the activation of a specific membrane-bound phospholipase C (PLC), which in turn leads to hydrolysis of phosphatidylinositol 4,5-bisphosphate which generates the diacylglycerol (DAG) and $IP_3$ second messengers (Patergnani et al., 2011). The binding of $IP_3$ to $IP_3Rs$ on the ER opens this tetrameric channel causing movement of $Ca^{2+}$ down the gradient from the ER lumen to the cytosol. Interestingly, $Ca^{2+}$ binding to the $IP_3R$ can sensitize the channel in a 'bell-shaped' manner which enhances $Ca^{2+}$ conduction at low levels, but inhibits the channel at high $[Ca^{2+}]$ (Berridge et al., 2003). Furthermore, $IP_3Rs$ can be modulated by various other signaling pathways, including phosphorylation via $Ca^{2+}$/CaM-dependent kinase II (CaMKII), cGMP-dependent protein kinase (PKG), protein kinase C (PKC), and cAMP-dependent protein kinase (protein kinase A, PKA) (Patergnani et al., 2011).

On the other hand, the RyR is the largest known ion channel (>2 MDa) that can be modulated directly or indirectly via $Ca^{2+}$ or $Mg^{2+}$ ions, small molecules, L-type $Ca^{2+}$ channels found on the transverse tubule (t-tubule) walls, and various proteins including CaMKII and PKA (Ikemoto et al., 1991; Mayrleitner et al., 1995; Nakai et al., 1998; Smith et al., 1986; J. Wang & Best, 1992). Three mammalian isoforms of RyR have been identified, with RyR1 found primarily in skeletal muscle and cerebellar Purkinje neurons, RyR2 found primarily in cardiac muscle and brain tissue, and RyR3 found primarily in the cortical/hippocampal region and diaphragm (Lanner et al., 2010). During cardiac muscle contraction, the action potential travels to the t-tubules enriched in L-type $Ca^{2+}$ channels; membrane depolarization opens the L-type $Ca^{2+}$ channels and $Ca^{2+}$ enters the cytosol from the extracellular space; this $Ca^{2+}$ binds to RyR2 on the SR, inducing further release of SR-stored $Ca^{2+}$ via the opening of tetrameric RyR2 channels, in a process termed excitation-contraction coupling (Bootman et al., 2006; Rios & Brum, 1987). In skeletal muscle, this release of $Ca^{2+}$ is mediated via direct physical interaction between RyR1 and the L-type $Ca^{2+}$ channels, whereas in cardiac cells, this release depends on a $Ca^{2+}$-induced $Ca^{2+}$ release, as the RyR2 responds to the influx of extracellular $Ca^{2+}$ from the L-type $Ca^{2+}$ channels (Endo, 1977). The release of $Ca^{2+}$ from the SR causes muscle contraction, while the SERCA pumps acts to replenish these $Ca^{2+}$ stores to induce relaxation (Nakai et al., 1998).

### 1.2.1 Store operated $Ca^{2+}$ entry (SOCE)

As briefly mentioned above, the SOC family of proteins found on the plasma membrane respond to decreasing stored ER $Ca^{2+}$ levels. SOC activation causes a large influx of $Ca^{2+}$ into the cytosol for downstream signaling and replenishing of the stored $Ca^{2+}$. In nonexcitable cells, SOCs are the primary source of cytosolic $Ca^{2+}$ mobilization in cells. The increase in cytosolic [$Ca^{2+}$] in response to SOCs plays a significant role in a variety of cell signaling pathways and processes, including secretion, gene transcription, and modulation of enzymatic activity (Prakriya & Lewis, 2015).

Stromal interaction molecule (STIM) proteins are the $Ca^{2+}$ sensors inserted into the ER and Orai proteins are the plasma membrane subunits that make up the SOC. The identification of these proteins played a prominent role in elucidating the molecular mechanisms underlying the SOCE pathway in various cell types (Feske et al., 2006; Liou et al., 2005). During resting conditions with ER luminal $Ca^{2+}$ stores in a replete state, STIM1 is usually found in an inactive conformation with its ER lumen-localized EF-hands bound to $Ca^{2+}$ ions. Upon cell surface receptor stimulation, ER luminal $Ca^{2+}$ stores are depleted via $IP_3Rs$, causing $Ca^{2+}$ to dissociate from the STIM1 EF hands. This loss of $Ca^{2+}$ binding leads to the destabilization-coupled oligomerization and movement of STIM1 proteins to the region of the ER which are in close proximity to the plasma membrane; further, active and oligomerized STIM1 proteins which move to ER-plasma junctions interact with and assemble Orai1 subunits into open channels, causing the influx of $Ca^{2+}$ down the steep concentration gradient from the extracellular space into the cytosol (Stathopulos et al., 2013; Stathopulos et al., 2008). The reuptake of $Ca^{2+}$ mediated by SERCA into the ER lumen results in a decoupling of STIM1 from Orai1 through a $Ca^{2+}$ binding-induced stabilization of STIM1 (Jousset et al., 2007). Ultimately, STIM1 and Orai1 return to their resting, diffuse distribution once the ER $Ca^{2+}$ stores are fully replenished (Malli et al., 2008).

Another intracellular organelle that plays a vital role in the uptake of cytoplasmic $Ca^{2+}$ is the mitochondria. Mitochondria can rapidly sequester $Ca^{2+}$ and slowly release it during the recovery phase of the signaling event (Berridge et al., 2000). Mitochondria are usually found in close proximity to $Ca^{2+}$ releasing channels, such as the $IP_3Rs$ and RyRs, improving the effectiveness of $Ca^{2+}$ uptake (Csordas et al., 1999; Rizzuto et al., 1993). Indeed, electron tomography has shown mitochondria to be tethered to the smooth ER membrane, with the regions of interaction termed as the mitochondria-associated membranes (MAMs) (Csordas et al., 2006; van Vliet et al., 2014). They are also found clustered around highly active channels in neurons and in close proximity to RyR channels in skeletal and cardiac muscle cells (Franzini-Armstrong, 2007). In fact, these organelles are even believed to modulate the SOCE signaling pathway in numerous ways, such as by the buffering of $Ca^{2+}$ around the ER-plasma membrane junction that can help prolong SOCE (Rizzuto et al., 2009). In T-cells, the mitochondria have been shown to accumulate near the plasma membrane in response to the activation of Orai1 channels and function in a positive feedback loop to sustain the activity of these channels by preventing their inactivation due to increasing $[Ca^{2+}]$ (Quintana et al., 2006). Additionally, mitochondria may indirectly affect SOCE via the production of ATP, pyruvate, and reactive oxygen species (ROS) (Bakowski & Parekh, 2007; Montalvo et al., 2006; Mungai et al., 2011).

### 1.2.2 $Ca^{2+}$ signaling and mitochondria

Mitochondria are primarily known as the power houses of cells for their role in the production of ATP; however, these small organelles also play vital roles in regulating apoptosis and shaping cytosolic calcium ($Ca^{2+}$) transients that signal a myriad of downstream processes (Gunter et al., 2000). Similar to the ER/SR, mitochondria can also store $Ca^{2+}$, however, mitochondrial $[Ca^{2+}]$ also plays a role in regulating the mitochondrial viability, movement, and ATP production (Clapham, 2007). Intracellular $Ca^{2+}$ signalling pathways and their regulation which involve mitochondrial $Ca^{2+}$ uptake have been implicated in numerous pathophysiological disorders such as cancer (Pinton et al., 2008), diabetes (Tarasov et al., 2012), neuronal excitotoxicity (C. V. Logan et al., 2014), and muscular atrophy or hypertrophy (Mammucari et al., 2016), to name a few. Work by Marchi et al. (2013) directly linked the downregulation of mitochondrial $Ca^{2+}$ uptake in cancer cell lines with a higher resistance to apoptotic signalling. Additionally, the uptake of $Ca^{2+}$ by mitochondria has been shown to regulate the secretion of insulin in pancreatic β-cells (Alam et al., 2012).

Mitochondria possess two membranes: (i) the outer mitochondrial membrane (OMM) facing the cytoplasm, and (ii) the inner mitochondrial membrane (IMM) facing the mitochondrial matrix. The IMM houses the electron transport chain protein machinery, which is responsible for transporting $H^+$ ions into the inner membrane space (IMS), generating a large electrochemical gradient resulting in a membrane potential of -150 to -180 mV. Movement of these $H^+$ ions down this gradient via ATP synthase leads to the production of ATP. The IMM forms a highly selective barrier between the cytosol and mitochondrial matrix that only allows the passage of substrates via specific ions channels and transporters (McStay, 2017). However, small molecules and ions in the cytoplasm can freely diffuse across the OMM due to the presence of numerous porins. The presence of the porous voltage-dependent anion channels (VDACs) on the OMM allows for the free diffusion of $Ca^{2+}$ into the IMS (Madesh & Hajnoczky, 2001). In contrast, the tightly regulated movement of $Ca^{2+}$ across the IMM depends largely on the MCU, a selective channel which utilises the highly negative membrane potential across the IMM to drive $Ca^{2+}$ into the mitochondrial matrix (Pozzan et al., 1994). The function and regulation of MCU is discussed in more detail below. Another IMM protein that plays a role in $Ca^{2+}$ entry is the leucine zipper EF-hand-containing transmembrane protein 1 (LETM1). However, little is currently known about its mechanism of action (Jiang et al., 2009). The uptake of $Ca^{2+}$ into the mitochondria is counteracted by the presence of mitochondrial NCX and $H^+/Ca^{2+}$ exchangers (mHCX) (Pozzan et al., 1977). Together, MCU, LETM1, mNCX and mHCX control the movement and concentration of $Ca^{2+}$ in the mitochondrial matrix.

The ability of mitochondria to uptake $Ca^{2+}$ combined with their close proximity to the ER and plasma membrane allows them to rapidly accumulate $Ca^{2+}$ upon increased cytosolic $[Ca^{2+}]$, thereby adding to the buffering capacity at the specific domains where mitochondria are clustered and to the cytoplasm in general (Rizzuto et al., 2012). The release of $Ca^{2+}$ from ROCs on the ER/SR or VOCs/SOCs on the plasma membrane can lead to an inhibitory, activating, or a biphasic response on a specific channel dependent on the level of cytosolic $[Ca^{2+}]$ (Bezprozvanny et al., 1991). Thus, mitochondria present near the openings of $Ca^{2+}$ channels can modify the local cytosolic $[Ca^{2+}]$, which can thereby regulate the opening and closing of these channels. Apart from the previously mentioned impact on the SOCE pathway, mitochondrial $Ca^{2+}$ uptake also helps control the excitation-contraction coupling system found in cardiac cells by modulating the $Ca^{2+}$ signaling function of RyRs (Pacher et al., 2002). The spatial organization and distribution of mitochondria in specific cell types such as neurons and pancreatic acinar cells may help spatially constrain the shaping of cytosolic $Ca^{2+}$ transients to a certain region of these cells (Billups & Forsythe, 2002; Voronina et al., 2002).

As mentioned above, the uptake of $Ca^{2+}$ into the mitochondrial matrix regulates the metabolic functions of mitochondria such as the production of ATP. The presence and activation of $Ca^{2+}$ dependent dehydrogenases in mitochondria increases the availability of NADH. This is essential for the flow of electrons down the electron transport chain, and thereby leads to increased synthesis of ATP (Jouaville et al., 1999). In addition, aspartate/glutamate exchangers present in the IMM can sense $Ca^{2+}$ levels in the IMS, leading to a more complex and coordinated response to changes in cytosolic and mitochondrial [$Ca^{2+}$] (Lasorsa et al., 2003). The enriched association of mitochondria with regions of $Ca^{2+}$ release and entry ensures rapid uptake of $Ca^{2+}$ by the organelle in order to match the energy demands of cellular processes signaled through cytosolic $Ca^{2+}$ entry (Rizzuto et al., 2012).

Additionally, mitochondria play an integral role in regulating cell survival. Prolonged high levels of $Ca^{2+}$ in the cytosol leads to the $Ca^{2+}$ overload of mitochondria which, in turn, results in opening of the mitochondrial permeability transition pore (mPTP) (Rizzuto et al., 2012). The mPTP opening causes the dissipation of IMM potential as ions and small molecules are released from the matrix; swelling of mitochondria can ensue causing subsequent release of cytochrome c and pyridine nucleotides. The resulting decrease in ATP production leads to the necrotic cell death pathways witnessed in cardiomyocytes (O'Rourke, 2000); however, apoptosis pathways are also activated by mPTP opening. The opening of mPTP and the resulting apoptotic and necrotic cell death pathways are regulated by numerous accessory proteins and factors such as the Bcl-2 family proteins Bax and Bak, cytochrome c, second mitochondria derived activator of caspase (smac)/DIABLO and apoptosis inducing factor (AIF) (Du et al., 2000; Liu et al., 1996; Susin et al., 1996; Verhagen et al., 2000; Wei et al., 2001). The inhibition or dysregulation of these pathways is implicated in the pathogenesis of various human disorders involving tumor or viral proteins (Chami et al., 2003; Pinton et al., 2001).

The interplay between autophagy and mitochondria has also been well established. Autophagy is a vital cellular process that helps clean up long-lived proteins, damaged or excess organelles, and even parts of cytosol as they are taken up via a double membrane vesicle and fused with lysosomes to form the autophagosome (He & Klionsky, 2009). ER, Golgi apparatus, plasma membrane and mitochondria have all been shown to play a role in the regulation and formation of autophagosome (Cuervo, 2010). Autophagy is primarily induced or activated in response to cellular stress, such as nutrient deprivation and largely serves a cytoprotective function (Singh & Cuervo, 2011). Recent work has associated autophagy with the cellular energy balance, placing mitochondria as a key regulator of this starvation-induced process and a supplier of the membranes that help form autophagosomes (Hailey et al., 2010). Furthermore, autophagy has been shown to selectively target damaged mitochondria and other organelles (Lemasters, 2005). Indeed, the division, fusion or migration of mitochondria in response to environmental and physiological stress helps the cell maintain energy demands (Chen & Chan, 2009). The elongation and fusion of mitochondria into network like structures during nutrient starvation has been shown to provide them protection from autophagy and allow them to function as efficient factories for bioenergetic functions (Gomes et al., 2011). Furthermore, the close association of $IP_3Rs$ on the ER with mitochondria has been implicated in the rapid uptake and sensing of $Ca^{2+}$ by mitochondria upon cellular stress, which has been shown to regulate autophagy pathways (Decuypere et al., 2011). The inhibition of mitochondrial $Ca^{2+}$ uptake has recently been implicated with enhanced autophagy (Tomar et al., 2016). The regulation of apoptotic and autophagy pathways by mitochondria has also been linked with numerous neurodegenerative diseases such as Alzheimer's, Parkinson's and Huntington's (Celsi et al., 2009). Due to their critical role in cellular bioenergetics and apoptotic pathways, mitochondrial dysfunction has been associated with numerous cancers (Wallace, 2012).

The implication of mitochondrial $Ca^{2+}$ uptake on both aerobic metabolism and cell survival pathways highlight the importance of studying the regulation of mitochondrial $Ca^{2+}$ uptake; further, it is important to reinforce that MCU represents the major ubiquitous $Ca^{2+}$ entry pathway into the mitochondrial matrix.

## 1.3 Mitochondrial calcium uniporter (MCU) complex

### 1.3.1 Identification of the MCU protein components

The emergent understanding that mitochondrial $Ca^{2+}$ uptake is central in the regulation of ATP production, autophagy and apoptotic pathways drove interest in identifying the underlying signalling molecules. The presence of a highly selective $Ca^{2+}$ channel present on the IMM with a high affinity for $Ca^{2+}$ was first realized about five decades ago. However, the detailed biophysical characterization of this channel remained elusive until a seminal electrophysiology study using patch-clamped mitochondria (Kirichok et al., 2004). Further, it was also established prior to the identification of the molecules mediating this uptake mechanism, that the channel depended on the steep electrochemical potential present across the IMM for moving $Ca^{2+}$ into the matrix (Rizzuto & Pozzan, 2006). Finally, the molecular identity of this channel was identified using the MitoCarta database generated by Pagliarini et al. (2008) which lists all mitochondria localized proteins. This database was established by performing mass spectrometry analysis of highly purified mitochondrial preparations to exclusively identify the mitochondrial proteins. These mitochondrial proteins were further confirmed via green fluorescent protein (GFP) tagging and localization experiments. Searching the MitoCarta database for proteins with a potential for $Ca^{2+}$ binding and channel formation, and subsequently, performing RNA interference (RNAi) screening on the shortlisted proteins led to the identification of mitochondrial calcium uptake 1 (MICU1) (Perocchi et al., 2010). However, it was quickly realized that MICU1 functions as regulator of a larger complex that forms the $Ca^{2+}$ channel (Raffaello et al., 2012), and is not the channel-forming protein itself.

Using a similar approach which led to the identification of MICU1, two groups were able to independently identify the major MCU protein component using the MitoCarta database (Baughman et al., 2011; De Stefani et al., 2011). The presence of putative transmembrane domains along with a putative loop enriched in acidic residues made coiled coil domain containing 109A (CCDC109A) (i.e. renamed to MCU) a strong candidate as the subunit which forms the $Ca^{2+}$ selective MCU channel (Raffaello et al., 2012). Baughman et al. (2011) also conducted small interfering RNA (siRNA) silencing of *MCU* in cultured and *in vivo* hepatocytes to demonstrate a severe loss of mitochondrial $Ca^{2+}$ uptake, while the mitochondrial membrane potential and oxidative phosphorylation pathways remained intact. Although these knockdown studies confirmed MCU as an essential component of the MCU complex, an overexpression analysis was also carried out to demonstrate an increase in mitochondrial $Ca^{2+}$ uptake and to confirm the role as the main pore forming subunit. Indeed, the overexpression of MCU led to a dramatic increase in mitochondrial $[Ca^{2+}]$ in response to $IP_3$ coupled agonist stimulation (De Stefani et al., 2011). The third and final piece of evidence confirming MCU as the main IMM $Ca^{2+}$ channel protein arose by studying the ability of purified MCU to transport $Ca^{2+}$ when inserted into a lipid bilayer. Not only was the channel activity observed, but ruthenium red (RuR), a known mitochondrial $Ca^{2+}$ uptake inhibitor, was shown to inhibit MCU channel activity (De Stefani et al., 2011). Several peripheral binding proteins have now been identified that regulate this MCU channel formation and gating, including essential MCU regulator (EMRE), MICU1 and -2 (MICU2) and MCU regulator 1 (MCUR1) (De Stefani et al., 2016). These regulatory proteins form a higher order heteromeric complex with the core MCU component on the IMM (Figure 1) and are discussed in more detail below.

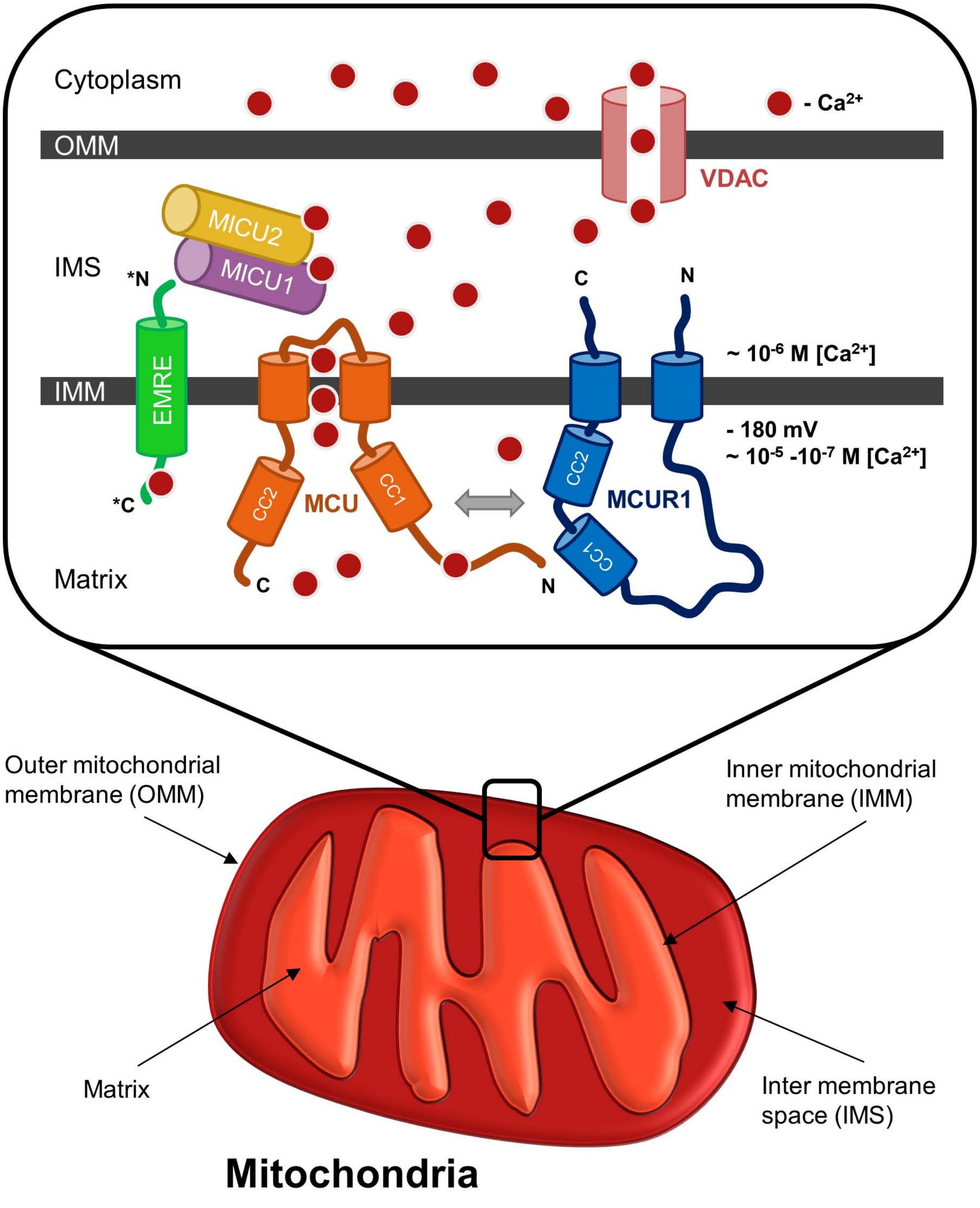

**Figure 1. Schematic representation of the topology of MCU, MCUR1 and other regulatory proteins.** $Ca^{2+}$ binding to MICU1 and MICU2 heterodimer, the N-terminal domain of MCU, and putatively to EMRE helps regulate the complex assembly. The coiled coil domains of MCUR1 interact with the N-terminal domain of MCU and functions as a scaffold protein for the complex. The '*' represents the contested topology of EMRE. $Ca^{2+}$ can flow across the OMM via the VDAC channels.

### 1.3.2 Structure and topology of MCU

An *MCU* gene is present in almost all plants and metazoa, with the exception of yeast, some protozoan and fungal lineages (Bick et al., 2012). In humans, the MCU channel subunit is a 35 kDa protein and is ubiquitously expressed across all tissue types. MCU is a dual transmembrane protein, with two coiled coil domains and a specialized region known as the DIME motif due to the high conservation of the Asp (D), Ile (I), Met (M), Glu (E) and the importance of the motif in coordinating $Ca^{2+}$. Although the topology of MCU was initially debated, it has now been established that the N- and C- terminal regions of the protein face the mitochondrial matrix, whereas the DIME motif is exposed to the IMS (Martell et al., 2012). Initially, GFP-tagging of the N-terminus of MCU and trypan blue analysis suggested MCU was localized on the IMM with the N- and C-termini facing the IMS since trypan blue, which is permeable to the OMM but not the IMM, was able to quench MCU-GFP florescence (De Stefani et al., 2011). In contrast, proteinase K analysis carried out on mitochondria with a permeabilized OMM was unable to digest MCU, thereby indicating that the N- and C- termini face the mitochondrial matrix (Baughman et al., 2011). The topology on this IMM protein was unequivocally established using an electron microscopy approach. Specifically, ascorbic peroxidase was used as a high definition marker in EM experiments. The separate N- and C-terminal fusions to an engineered ascorbic peroxidase showed high EM contrast after diaminobenzidine/$H_2O_2$ treatment exclusively inside the mitochondrial matrix and thereby demonstrated that both the N- and C-terminus of MCU face the matrix (Martell et al., 2012). Thus, the DIME motif and other important acidic residues (i.e. E256, D260, and E263) face the IMS. Collectively, these residues are critical for $Ca^{2+}$ permeability and conduction, as charge neutralizing mutations of these amino acids lead to a loss of $Ca^{2+}$ uptake (Raffaello et al., 2013). The S259A mutation near the DIME motif was also found to reduce RuR sensitivity of the channel (Baughman et al., 2011).

Intriguingly, *MCUb*, a related gene translated with ~50 % sequence similarity to MCU has been identified that functions as a dominant negative regulator of the MCU channel formation (Raffaello et al., 2013). Much like MCU, MCUb also contains two coiled coil domains and two transmembrane domains separated by a short loop region allowing it to closely associate and form heterooligomers with MCU (Raffaello et al., 2013). However, crucial acidic DIME residues are substituted in MCUb (i.e. E256V), likely causing MCU channel inhibition when incorporated into the complex (Raffaello et al., 2013).

### 1.3.3 Oligomerization of MCU

Oligomerization of MCU leads to formation of the channel that mediates $Ca^{2+}$ uptake into the matrix (Raffaello et al., 2013). However, the homotypic interactions between these MCU subunits remain poorly defined for the human protein. Based on data from other known channel forming proteins and molecular dynamic simulations, a quaternary structure with a four-fold symmetry was predicted (Raffaello et al., 2013). Additionally, native gel electrophoresis confirmed the presence of a higher order oligomeric complex with an apparent molecular weight of ~480 kDa, indicating the presence of other regulatory proteins (Baughman et al., 2011). Recent work by Oxenoid et al. (2016) utilizing both EM and nuclear magnetic resonance (NMR) spectroscopy on *C. elegans* MCU with a deleted N-terminal domain provided the first high resolution structural insights, proposing a pentameric organization for MCU. The pentameric NMR/EM model places the DIME motif in a loop at the opening of the pore with carboxylic acid side chains protruding into the entrance of the channel. Nevertheless, numerous recent fungal and metazoan cryo-electron microscopy (cryo-EM) structures (excluding human) using full-length MCU have been solved, unequivocally demonstrating that MCU assembles as a tetramer with the DIME motif forming part of the transmembrane helix (i.e. not an unstructured loop) which lines the pore and the $Ca^{2+}$ selectivity filter (Fan et al., 2018; Nguyen et al., 2018; Yoo et al., 2018). The structure of MCU is discussed in more detail in the Discussion section of the thesis.

### 1.3.4 Divalent cation sensing at the N-terminal domain

The Stathopulos laboratory has previously solved the high resolution (1.8 Å) crystal structure for the highly conserved N-terminal domain of human MCU (S. K. Lee et al., 2016). The structure of the MCU N-terminal domain resembles that of a β-grasp fold and contains two electropositive and two electronegative patches that may play a role in oligomerization via complementary electrostatic interactions. Additionally, this N-terminal domain was shown to be sensitive to divalent cations, with a loss in oligomerization and stability observed at ~mM $Mg^{2+}$ and $Ca^{2+}$ concentrations, suggesting a role in self regulation of MCU channel activity, similar to other $Ca^{2+}$ channel proteins such as $IP_3Rs$ and RyRs (see above). Apart from its potential impact on channel oligomerization and activity, the N-terminal domain was shown to be a phosphorylation target by CaM kinase II, a site for *S*-glutathionylation under oxidative stress conditions and an important protein-protein interaction domain with MCUR1, a putative scaffolding factor involved in the formation of MCU complex (Dong et al., 2017; Y. Lee et al., 2015; Tomar et al., 2016).

## 1.4 MICU1 and MICU2

The discovery of MICU1 preceded that of MCU by a few months, and this earlier work was pivotal for the appreciation that MCU functions as a higher order complex of multiple proteins (Perocchi et al., 2010). MICU1 is a 54 kDa protein containing a highly debated, single transmembrane domain, and two conserved EF-hand $Ca^{2+}$ binding domains. The localization of MICU1 still requires clarification; however, proteomics data and the proposed function of MICU1 as a gatekeeper of MCU suggests that it is present in the IMS (Hung et al., 2014). As previously mentioned, a key feature of mitochondrial $Ca^{2+}$ uptake is the biphasic response to cytosolic $[Ca^{2+}]$, such that at low cytosolic $[Ca^{2+}]$ the rate of mitochondrial uptake is kept low, while the carrying capacity dramatically increases with increasing cytosolic $[Ca^{2+}]$. The topology of MCU, with both N- and C-termini facing the mitochondrial matrix suggests that the presence of a regulatory protein is responsible for modulating the opening and closing of the MCU channel. Indeed, it was shown by Mallilankaraman et al. (2012) that silencing of MICU1 led to the constitutive overloading of mitochondria even at lower cytosolic $[Ca^{2+}]$. The role of MICU1 as a gatekeeping molecule was further reinforced when it was shown that MICU1 not only regulates the threshold of MCU channel opening, but also acts as a cooperative promoter of channel activity at higher cytosolic $[Ca^{2+}]$ (Csordas et al., 2013).

Adding further to the complexity of MICU regulation, mammalian cells express three MICU homologues: MICU1, MICU2 and MICU3 (Plovanich et al., 2013). Unlike MICU1 and MICU2, MICU3 does not display strong mitochondrial localization and is therefore not included in the MitoCarta list (Pagliarini et al., 2008). MICU2, however, does localize to mitochondria and contains EF-hand $Ca^{2+}$ binding domains like MICU1 (Plovanich et al., 2013). In fact, MICU2 has been shown to directly associate with MICU1 and play a gatekeeping role at low $Ca^{2+}$ levels (Patron et al., 2014). Overexpression of MICU2 leads to a lower MCU channel open probability at low [$Ca^{2+}$], with no effect seen at higher [$Ca^{2+}$] (Patron et al., 2014). Extensive work conducted by Matesanz-Isabel et al. (2016) also showed that silencing of MICU2 results in large mitochondrial $Ca^{2+}$ uptake at cytosolic [$Ca^{2+}$] between ~100 nM to 4.5 μM, whereas at concentrations above ~7 to 10 μM cytosolic [$Ca^{2+}$] the absence of MICU2 does not impact mitochondrial $Ca^{2+}$ uptake. This trend suggests that MICU2 functions as a genuine inhibitor of MCU channel activity, while MICU1 plays a dual inhibitory role at low cytosolic [$Ca^{2+}$] and acts as a channel activity promoter at cytosolic [$Ca^{2+}$] above ~2.5 μM (Matesanz-Isabel et al., 2016). The measurements were conducted using genetic and fluorescent dye $Ca^{2+}$ indicators (Matesanz-Isabel et al., 2016). Additionally, the stable expression of MICU2 is dependent on MICU1. The silencing of MICU1 leads to a reduction in MICU2 protein levels, suggesting that the loss in gatekeeping function observed in the absence of MICU1 is due, in part, to the collective loss of MICU2 (Patron et al., 2014). Consequently, it has been established that MICU1 and MICU2 function as a stable heterodimer, where MICU1 is shown to tightly associate with the MCU complex (Kamer & Mootha, 2014; Patron et al., 2014). Although little is known about the third isoform MICU3, it appears to be predominantly expressed in the central nervous system and may have tissue specific functions (Plovanich et al., 2013).

## 1.5 Essential MCU regulator (EMRE)

Another important regulatory protein of the MCU complex is EMRE, identified using stable isotope labelling by amino acids in cell culture (SILAC) and mass spectroscopy proteomics analysis (Sancak et al., 2013). Previously known as C22ORF32, EMRE is a small, 10 kDa protein containing a single transmembrane domain, with a highly conserved C-terminal domain rich in Asp residues (Sancak et al., 2013). This IMM protein is proposed to interact not only with MCU, but also with the MICU1/MICU2 heterodimer present in the IMS. Sancak et al. (2013) showed that the knockdown of

EMRE leads to complete abrogation of $Ca^{2+}$ uptake into the mitochondria via MCU, which was not recovered with the overexpression of MCU. Indeed, blue native polyacrylamide gel electrophoresis shows a reduction in the size of the MCU complex with the knockout of EMRE (Sancak et al., 2013). Interestingly, this implication of EMRE as an essential component of the MCU complex formation in humans does not apply to plants or fungi, which have no known homologs of EMRE (Sancak et al., 2013). Additionally, similar to the MICU2 stability dependence on MICU1, the levels of EMRE are drastically reduced in MCU-depleted cells, consistent with the close association between the two proteins (Sancak et al., 2013).

The Asp-rich C-terminal region of EMRE is believed to play an important role in MCU complex regulation; however, the topology of EMRE is still being debated. Recent work by Vais et al. (2016) suggests a mitochondrial matrix $Ca^{2+}$ sensing role for the negatively charged C-terminal domain of EMRE. Proteinase K protection assays on mitochondria in the presence of 0-2 % (v/v) digitonin suggested that the N-terminal domain faces the IMS as it was degraded first by the protease. Furthermore, Vais et al. (2016) showed that the deletion of the EMRE putative mitochondrial matrix $Ca^{2+}$ sensing C-terminal domain led to an unregulated uptake of $Ca^{2+}$ into the mitochondrial matrix. Conversely, it has also been suggested that the negatively charged C-terminal domain may have a potential role in interacting with the MICU1/MICU2 gatekeeping molecules of the MCU complex (Tsai et al., 2016). The presence of a polybasic sequence on MICU1 suggests a putative mechanism for the interaction via electrostatic complementarity. Interestingly, Tsai et al (2016) also showed that the transmembrane domain of EMRE interacts directly with the first transmembrane helix of MCU.

## 1.6 MCUR1

The identification of MCUR1 was a result of a slightly different approach. RNAi screening in HEK293T cells was conducted for 45 mitochondrial membrane proteins that were predicted to be present on the IMM or were previously reported to play a role in $Ca^{2+}$ signalling (Mallilankaraman et al., 2012). Only one of the 45 screened proteins showed a marked reduction in mitochondrial $Ca^{2+}$ uptake, namely CCDC90A, which was renamed MCUR1. MCUR1 was shown to be a ubiquitously expressed protein in vertebrates similar to MCU, EMRE, MICU1, and MICU2. The same study also demonstrated that, apart from abrogating the agonist induced uptake of $Ca^{2+}$ in mitochondria, the silencing of MCUR1 led to a large decrease of basal [$Ca^{2+}$] in the mitochondrial matrix. Interestingly, the localization and expression level of MCU was not affected by the loss of MCUR1. Collectively, these findings suggest a critical regulatory role for MCUR1 in the MCU mediated $Ca^{2+}$ uptake in mitochondria (Mallilankaraman et al., 2012). Furthermore, the topology of this putative dual transmembrane protein was studied using proteinase K assay on digitonin permeabilized cells and incubated with truncated Bid, a pro apoptotic protein that selectively permeabilized the OMM (Kuwana et al., 2002). The presence of a slightly truncated MCUR1 (i.e. ~6 kDa digestion) in the solubilized membrane fractions, as visualized by western blot analysis, showed that the majority of MCUR1 was protected and thus exposed to the mitochondrial matrix, with the N- and C-terminal facing the IMS (Mallilankaraman et al., 2012).

### 1.6.1 MCUR1 association with MCU

MCUR1 has been shown to associate with MCU by coimmunoprecipitation assays, where MCUR1 was able to pull down MCU and *vice versa* (Mallilankaraman et al., 2012). However, MICU1 was not pulled down in the same MCUR1 coimmunoprecipitation assay, suggesting the presence of two qualitatively distinct MCU complexes. This data implies that a pool of MCU can work independently of the gatekeeping regulator, allowing it to uptake $Ca^{2+}$ even at resting conditions (De Stefani et al., 2016). Recent work has further shown that the MCUR1 interaction with MCU is highly specific, as immunoprecipitation assays did not show any interaction between MCUR1 and the structural homolog of MCU, MCUb (Tomar et al., 2016). Additionally, it was shown that MCUR1 interacts with EMRE. Further, using blue native gel electrophoresis, and MCU size exclusion fractionation profiling, it was shown that MCUR1 is required for stabilizing the higher order oligomeric formation of the MCU complex. Indeed, the knockout of MCUR1 in mice endothelial cells resulted in a lower order molecular MCU complex formation (Tomar et al., 2016). Although the interaction of MCU and MCUR1 has been established, details of the interface remain unclear.

Several truncation and deletion mutations of MCU and MCUR1 were engineered to identify the regions of interaction via immunoprecipitation followed by western blotting (Tomar et al., 2016). The predicted matrix-oriented domains of each protein appear to play a role in the interaction, with residues 150-231 for MCU and 166-305 for MCUR1 playing a significant role in the interaction. These regions are comprised of both coiled coil and other folded domains.

Apart from a role in regulating MCU channel activity by promoting higher order complex formation, MCUR1 has been shown to function as a threshold regulator for the opening of mPTP (Chaudhuri et al., 2016). When expressed in the $Ca^{2+}$ overload resistant *Drosophila* S2R+ cells, MCUR1 greatly reduces the threshold required for mPTP opening. Conversely, the genetic inhibition of MCUR1 in mammalian cells significantly increased the threshold for $Ca^{2+}$ overload. Although MCUR1 appears to play a key role in the mPTP threshold regulation, it does not act as a direct $Ca^{2+}$ sensor for mPTP; however, it is thought to assist in bridging the MCU and mPTP complexes (Chaudhuri et al., 2016). Additionally, MCUR1 was suggested to help assemble the complex IV of the electron transport chain and, thereby, have an indirect effect on MCU channel activity via the establishment of the highly negative membrane potential. Indeed, knockdown of MCUR1 was shown to impair oxidative phosphorylation activity, reduce membrane potential across the IMM and, thereby, also impair $Ca^{2+}$ uptake (Paupe et al., 2015). However, recent electrophysiological studies on the MCU-dependent $Ca^{2+}$ currents in isolated mitoplasts (i.e. mitochondria stripped of the OMM) showed that MCUR1 knockdown inhibited the MCU channel activity even under voltage clamp-mediated fixed membrane potentials (Vais et al., 2015). This observation further confirmed the direct role of MCUR1 in MCU complex assembly and function.

### 1.6.2 Structural knowledge gaps

MCUR1 is a 40 kDa dual transmembrane protein that contains two putative coiled coil domains and is well conserved across higher order species (Figure 2). The ability of MCUR1 to stabilize the subcomplexes and the presence of coiled coil domains which are considered important for protein-protein interactions make MCUR1 a strong candidate for functioning as a scaffolding factor in MCU complex formation (Tomar et al., 2016).

The concept is supported by both the formation of a smaller MCU complex and the significantly lower $Ca^{2+}$ uptake by mitochondria in the absence of MCUR1. The topology of MCUR1 and MCU also suggests that the interaction occurs in the mitochondrial matrix, as the majority of both proteins, including the coiled coil domains, reside in the matrix. Despite the demonstrated fundamental role of MCUR1 in the regulation of MCU activity, mPTP opening and functioning of the electron transport chain, there currently exists no high-resolution structural information on MCUR1.

**A**

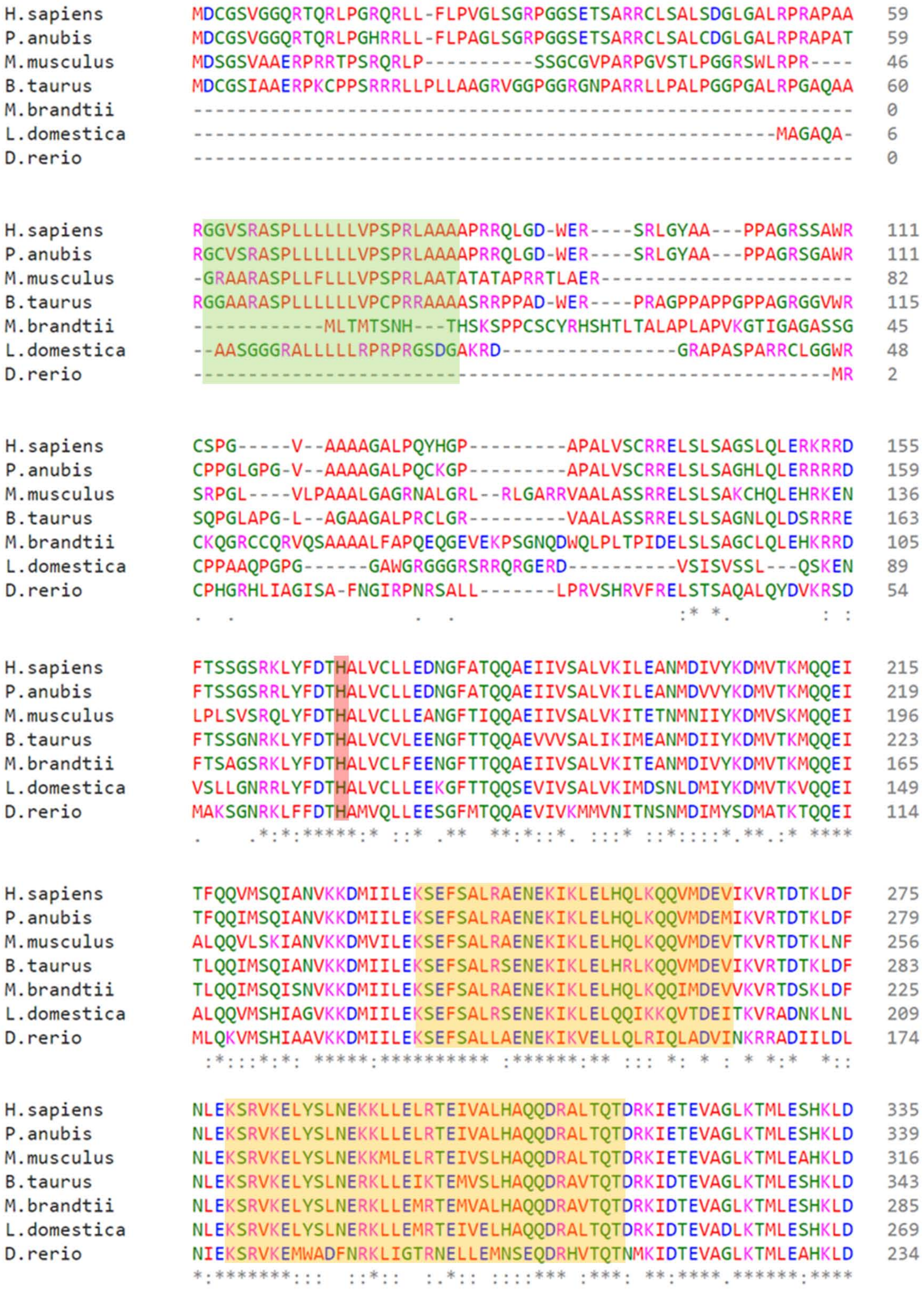

```
H.sapiens      MDCGSVGGQRTQRLPGRQRLL-FLPVGLSGRPGGSETSARRCLSALSDGLGALRPRAPAA   59
P.anubis       MDCGSVGGQRTQRLPGHRRLL-FLPAGLSGRPGGSETSARRCLSALCDGLGALRPRAPAT   59
M.musculus     MDSGSVAAERPRRTPSRQRLP----------SSGCGVPARPGVSTLPGGRSWLRPR----   46
B.taurus       MDCGSIAAERPKCPPSRRRLLPLLAAGRVGGPGGRGNPARRLLPALPGGPGALRPGAQAA   60
M.brandtii     ------------------------------------------------------------   0
L.domestica    -----------------------------------------------------MAGAQA-   6
D.rerio        ------------------------------------------------------------   0


H.sapiens      RGGVSRASPLLLLLLVPSPRLAAAAPRRQLGD-WER----SRLGYAA---PPAGRSSAWR   111
P.anubis       RGCVSRASPLLLLLLVPSPRLAAAAPRRQLGD-WER----SRLGYAA---PPAGRSGAWR   111
M.musculus     -GRAARASPLLFLLLVPSPRLAATATATAPRRTLAER-----------------------   82
B.taurus       RGGAARASPLLLLLLVPCPRRAAAASRRPPAD-WER----PRAGPPAPPGPPAGRGGVWR   115
M.brandtii     -----------MLTMTSNH---THSKSPPCSCYRHSHTLTALAPLAPVKGTIGAGASSG   45
L.domestica    --AASGGGRALLLLLRPRPRGSDGAKRD----------------GRAPASPARRCLGGWR   48
D.rerio        ----------------------------------------------------------MR   2


H.sapiens      CSPG-----V--AAAAGALPQYHGP---------APALVSCRRELSLSAGSLQLERKRRD   155
P.anubis       CPPGLGPG-V--AAAAGALPQCKGP---------APALVSCRRELSLSAGHLQLERRRRD   159
M.musculus     SRPGL----VLPAAALGAGRNALGRL--RLGARRVAALASSRRELSLSAKCHQLEHRKEN   136
B.taurus       SQPGLAPG-L--AGAAGALPRCLGR---------VAALASSRRELSLSAGNLQLDSRRRE   163
M.brandtii     CKQGRCCQRVQSAAAALFAPQEQGEVEKPSGNQDWQLPLTPIDELSLSAGCLQLEHKRRD   105
L.domestica    CPPAAQPGPG------GAWGRGGGRSRRQRGERD----------VSISVSSL---QSKEN   89
D.rerio        CPHGRHLIAGISA-FNGIRPNRSALL-------LPRVSHRVFRELSTSAQALQYDVKRSD   54
               .  .                .  .                    :* *.        : :

H.sapiens      FTSSGSRKLYFDTHALVCLLEDNGFATQQAEIIVSALVKILEANMDIVYKDMVTKMQQEI   215
P.anubis       FTSSGSRRLYFDTHALVCLLEDNGFATQQAEIIVSALVKILEANMDVVYKDMVTKMQQEI   219
M.musculus     LPLSVSRQLYFDTHALVCLLEANGFTIQQAEIIVSALVKITETNMNIIYKDMVSKMQQEI   196
B.taurus       FTSSGNRKLYFDTHALVCVLEENGFTTQQAEVVVSALIKIMEANMDIIYKDMVTKMQQEI   223
M.brandtii     FTSAGSRKLYFDTHALVCLFEENGFTTQQAEIIVSALVKITEANMDIVYKDMVTKMQQEI   165
L.domestica    VSLLGNRRLYFDTHALVCLLEEKGFTTQQSEVIVSALVKIMDSNLDMIYKDMVTKVQQEI   149
D.rerio        MAKSGNRKLFFDTHAMVQLLEESGFMTQQAEVIVKMMVNITNSNMDIMYSDMATKTQQEI   114
               .    .*:*:*****:* ::* .**  **:*::*. :::* ::*::::*.**.:* ****

H.sapiens      TFQQVMSQIANVKKDMIILEKSEFSALRAENEKIKLELHQLKQQVMDEVIKVRTDTKLDF   275
P.anubis       TFQQIMSQIANVKKDMIILEKSEFSALRAENEKIKLELHQLKQQVMDEMIKVRTDTKLDF   279
M.musculus     ALQQVLSKIANVKKDMVILEKSEFSALRAENEKIKLELHQLKQQVMDEVTKVRTDTKLNF   256
B.taurus       TLQQIMSQIANVKKDMIILEKSEFSALRSENEKIKLELHRLKQQVMDEVIKVRTDTKLDF   283
M.brandtii     TLQQIMSQISNVKKDMIILEKSEFSALRAENEKIKLELHQLKQQIMDEVVKVRTDSKLDF   225
L.domestica    ALQQVMSHIAGVKKDMIILEKSEFSALRSENEKIKLELQQIKKQVTDEITKVRADNKLNL   209
D.rerio        MLQKVMSHIAAVKKDMIILEKSEFSALLAENEKIKVELLQLRIQLADVINKRRADIILDL   174
                :*:::*:*: *****:********** :******:** ::: *: * : * *:*  *::

H.sapiens      NLEKSRVKELYSLNEKKLLELRTEIVALHAQQDRALTQTDRKIETEVAGLKTMLESHKLD   335
P.anubis       NLEKSRVKELYSLNEKKLLELRTEIVALHAQQDRALTQTDRKIETEVAGLKTMLESHKLD   339
M.musculus     NLEKSRVKELYSLNEKKMLELRTEIVSLHAQQDRALTQTDRKIETEVAGLKTMLEAHKLD   316
B.taurus       NLEKSRVKELYSLNERKLLEIKTEMVSLHAQQDRAVTQTDRKIDTEVAGLKTMLESHKLD   343
M.brandtii     NLEKSRVKELYSLNERKLLEMRTEMVALHAQQDRAVTQTDRKIDTEVAGLKTMLESHKLD   285
L.domestica    NLEKSRVKELYSLNERKLLEMRTEIVELHAQQDRALTQTDRKIDTEVADLKTMLESHKLD   269
D.rerio        NIEKSRVKEMWADFNRKLIGTRNELLEMNSEQDRHVTQTNMKIDTEVAGLKTMLEAHKLD   234
               *:*******:::  ::*::  :.*:: ::::*** :***: **:****.******:****
```

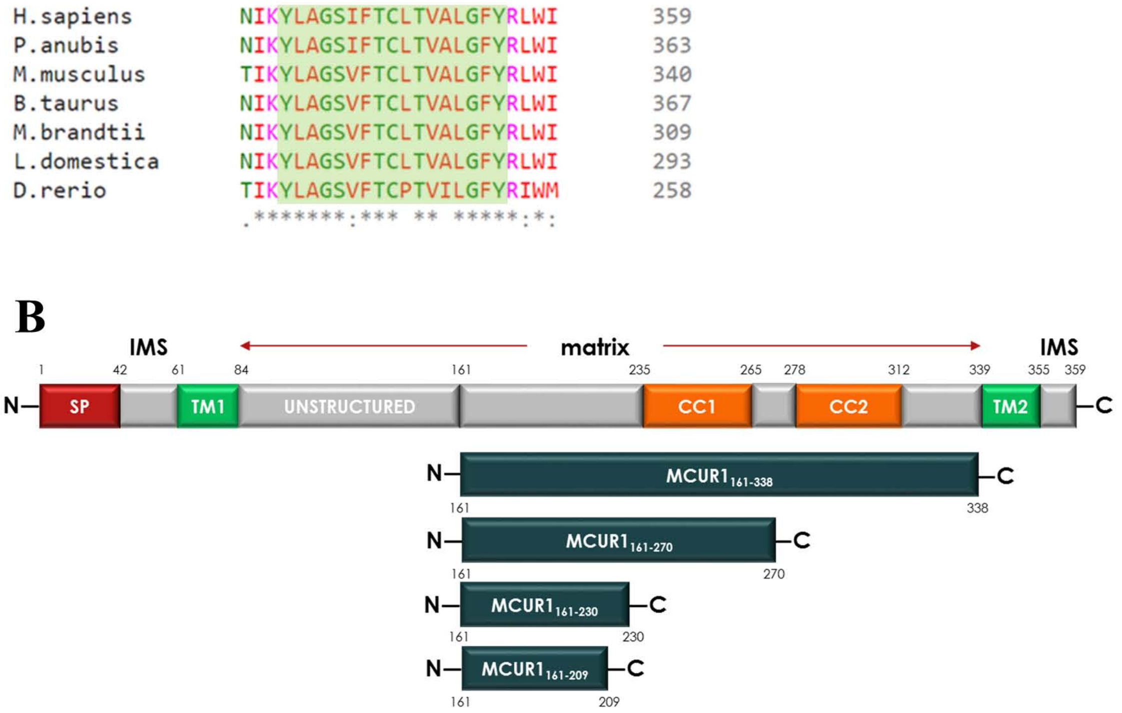

```
H.sapiens       NIKYLAGSIFTCLTVALGFYRLWI      359
P.anubis        NIKYLAGSIFTCLTVALGFYRLWI      363
M.musculus      TIKYLAGSVFTCLTVALGFYRLWI      340
B.taurus        NIKYLAGSVFTCLTVALGFYRLWI      367
M.brandtii      NIKYLAGSVFTCLTVALGFYRLWI      309
L.domestica     NIKYLAGSVFTCLTVALGFYRLWI      293
D.rerio         TIKYLAGSVFTCPTVILGFYRIWM      258
                .*******:*** ** *****:*:
```

**Figure 2. Primary structure alignment of full length human MCUR1 and its predicted domain architecture. A)** Alignment was conducted using Clustal Omega software on MCUR1 protein across seven species namely, *Homo sapiens* (human) MCUR1 (NP_001026883.1), *Papio anubis* (olive baboon) (XP_003897124.1), *Mus musculus* (mouse) (NP_001074528.1), *Bos taurus* (cattle) (NP_001095779.1), *Myotis brandtii* (Brandt's bat) (EPQ15249.1), *Lonchura striata domestica* (society finch) (XP_021408961.1) and *Danio rerio* (zebrafish) (AAI50229.1) to identify the conserved regions of MCUR1. The putative pH sensitive H169 residue is shaded red. Completely conserved regions are identified by '*****', highly conserved by '**:**' and partially conserved by '**.**' symbols. The predicted locations of the transmembrane domains are shaded green, while the coiled coil domains are shaded orange. Residue numbers are shown at right. **B)** Location of the conserved MCUR1 constructs under investigation are shown relative to the domain architecture of the full-length human MCUR1 protein. The architecture is composed of a signal peptide (SP), two transmembrane domains (TM1 and TM2), and two coiled coil domains (CC1 and CC2). Residue numbers indicate the boundary of each putative domain. N, amino terminus; C, carboxyl terminus; IMS, inner membrane space.

## 1.7 Rationale

MCU complex formation and regulation is mediated by both homotypic and heterotypic interactions. Further, the uptake of $Ca^{2+}$ by mitochondria plays a vital role in normal physiology (i.e. ATP production, apoptosis, autophagy, and shaping spatio-temporal $Ca^{2+}$ signals of the cytosol) as well as many metabolic, neurodegenerative, and chronic disorders (De Stefani et al., 2016; O'Rourke, 2000). Several high resolution structures for MCU and MICU1 have been elucidated, leading to a greater understanding of $Ca^{2+}$ uptake via the MCU channel (Fan et al., 2018; S. K. Lee et al., 2016; Y. Lee et al., 2015; Nguyen et al., 2018; Oxenoid et al., 2016; L. Wang et al., 2014; Yoo et al., 2018). Nevertheless, although MCUR1 has been shown to impact MCU complex formation and $Ca^{2+}$ uptake, no structural data exists which could help ascertain the mechanism underlying its function. Additionally, given that MCUR1 is a dual transmembrane protein that functions as a scaffolding factor in regulating the higher order assembly of the MCU complex, I predict that MCUR1 also has a propensity for assembly, and this homo-oligomerization plays a role in the higher order MCU complex assembly and function. Homo-oligomerization may also allow MCUR1 to interact with multiple MCU complexes at one time, facilitating a clustering of these $Ca^{2+}$ channels for more localized bursts of $Ca^{2+}$ uptake. This phenomenon has been recently observed in HeLa cells, where the post-translational modification of MCU (i.e. *S*-glutationylation) in the mitochondrial matrix leads to the ordered clustering of the MCU complexes (Dong et al., 2017).

Considering the importance of regulating mitochondrial $[Ca^{2+}]$ relative to the cytosolic levels, many of the proteins involved in the formation of the MCU complex have an intrinsic $Ca^{2+}$ sensing capacity. Both MICU1 and MICU2 contain $Ca^{2+}$-binding EF hands which allows them to sense cytosolic $[Ca^{2+}]$ (Csordas et al., 2013; Mallilankaraman et al., 2012). Additionally, the negatively charged Asp-rich tail of EMRE has been proposed to act as a mitochondrial matrix $[Ca^{2+}]$ sensor (Vais et al., 2016). The Stathopulos laboratory has previously shown the matrix facing N-terminal domain of MCU itself has a $Ca^{2+}$ and $Mg^{2+}$ sensing capacity (S. K. Lee et al., 2016). Based on these findings and given the established role of MCUR1 as a fundamental regulator of the MCU complex, I predict MCUR1 also contains a $Ca^{2+}$ sensing region.

With the numerous recent cryo-EM and crystal structures solved for MCU, our understanding of the underlying molecular mechanisms of MCU channel function and formation is largely limited by the available structural information of the key regulators of this complex such as MCUR1. Thus, I believe the structural and biophysical characterization of the domains of MCUR1 will fill an important knowledge gap providing key insights into the molecular mechanisms regulating $Ca^{2+}$ uptake via the MCU complex. In particular, analyzing the constructs targeted towards this conserved matrix-oriented region that contains two putative coiled coil domains and a structured region should provide novel insights into the roles of these domains in the functioning of MCUR1 as an MCU complex regulator.

## 1.8 Hypothesis and aims

**Hypothesis:**

I hypothesize that the conserved matrix-oriented region of MCUR1 plays vital roles in mediating self-association and sensing divalent cations which regulate MCU complex formation and function.

**Aim1:**

The IMM-localized regulatory protein MCUR1 plays a vital role in $Ca^{2+}$ signaling as recent knockdown studies in mouse cardiomyocytes have shown impairment of both, mitochondrial $Ca^{2+}$ uptake and MCU complex formation (Tomar et al. 2016). My work aims to biochemically and biophysically characterize the conserved MCUR1 domains to reveal new insights into the physicochemical nature of its regulatory function.

**Aim2:**

Currently, there exists no high resolution structural data for the recently identified MCU regulatory protein, MCUR1. Further, given that highly conserved protein domains among phylogeny play fundamental roles in the underlying functional mechanisms of proteins, I aim to elucidate the first high resolution structural insights into the matrix-oriented region of MCUR1 which exhibits high amino acid sequence conservation. These data will provide new insights into the molecular mechanisms of MCUR1 scaffolding function.

# Chapter 2

# 2 Methods

## 2.1 Bioinformatics

Homology analysis was conducted using Clustal Omega software on *Homo sapiens* (human) (NP_001026883.1), *Papio anubis* (olive baboon) (XP_003897124.1), *Mus musculus* (mouse) (NP_001074528.1), *Bos taurus* (cattle) (NP_001095779.1), *Myotis brandtii* (Brandt's bat) (EPQ15249.1), *Lonchura striata domestica* (society finch) (XP_021408961.1) and *Danio rerio* (zebrafish) (AAI50229.1) MCUR1 amino acid sequences to identify conserved regions (Sievers et al., 2011). The secondary structure predictions were obtained using PSIPRED protein sequence analysis workbench by the bioinformatics group at University College (London, UK) (Buchan et al., 2013). Additionally, the transmembrane and mitochondrial signal peptide sequence predictions were obtained from the online servers, TMpred (Swiss Institute of Bioinformatics) and TargetP 1.1 (University of Denmark), respectively (Emanuelsson et al., 2007; Hofmann & Stoffel, 1992). Two independent programs were used to predict the location of coiled coil domains, namely COILS (Swiss Institute of Bioinformatics) and Coiled-coil Prediction (Pole Rhône-Alpes Bioinformatics Center) (Combet et al., 2000; Lupas et al., 1991).

## 2.2 Designing and engineering of MCUR1 constructs

Four MCUR1 constructs were identified as structural targets based on high amino acid sequence conservation, high level of predicted secondary structure and high solubility (i.e. excluding the putative transmembrane regions): *i*) MCUR1$_{161\text{-}338}$, *ii*) MCUR1$_{161\text{-}270}$, *iii*) MCUR1$_{161\text{-}230}$, and *iv*) MCUR1$_{161\text{-}209}$, where subscripted integer range corresponds to the residue number range of the human protein. The DNA sequences which encode the 161-338 and 161-270 residue ranges were amplified using the polymerase chain reaction (PCR) with specifically designed primers, as indicated in Table 1. A full-length *H. sapiens* FLAG-tagged MCUR1 template held in a pCMV6-Entry (C-terminal Myc- and DDK-tagged) vector was used for amplification, and the inserts generated were subcloned into a pET-28a vector (Novagen) in frame with a hexahistidine tag (6×-His tag) using NheI and XhoI restriction enzyme sites designed into the 5’ and 3’ ends, respectively, of the amplification primers.

Specifically, a 150 μL PCR mixture was prepared using 114 μL deionized, filtered and autoclaved water ($dH_2O$), 30 μL of 5× high fidelity (HF) buffer, ~45 ng of pCMV6-Entry-FLAG-MCUR1 template, ~750 ng of forward and reverse primers each, 1.5 μL of 10 mM dNTPs, and lastly 0.75 μL of Phusion DNA polymerase (Thermo Fisher Scientific). These PCR mixtures were placed in a LifeECO thermocycler (BioER) for amplification. Amplification was performed with the initial denaturation cycle set to 98 °C for 1 min, followed by 35 cycles of denaturation at 96 °C for 30 s, annealing at 56-58 °C for 1 min, and extension at 72 °C for 30 s. A final extension was performed at 72 °C for 5 min. Subsequently, the PCR amplified product was electrophoresed on a 1 % (w/v) agarose gel prepared in 0.5× TRIS, acetic acid, ethylene diamine tetra acetic acid (EDTA) (TAE) running buffer. Following electrophoresis, the gel was submerged in 0.5 μg $mL^{-1}$ ethidium bromide (EB) solution and placed on a platform shaker for 30 min. After this EB staining procedure, the gel was visualized under a UV light (302 nm), the bands corresponding to the expected number of base pairs (bp) for each of the target constructs (i.e. 534 and 330 bp for $MCUR1_{161-338}$ and $MCUR1_{161-270}$, respectively) were excised and transferred into microcentrifuge tubes for extraction. The amplified PCR products were extracted from the agarose gel fragments using the GenepHlow Gel/PCR kit as described by the manufacturer (GeneAid) protocol.

The purified MCUR1 inserts and pET-28a vector were then double digested with NheI and XhoI, to generate sticky ends. Restriction digest mixtures for the MCUR1 constructs consisted of 35 μL MCUR1 insert (i.e. the total PCR amplified product), 4.2 μL of the 10× Cut Smart Buffer, and 1.5 μL each of NheI and XhoI enzymes (New England Biolabs), whereas the pET-28a vector digestion was carried out using 10 μL pET-28a vector (i.e. ~1.5 μg), 2 μL of the 10× Smart Cut Buffer, 5 μL $dH_2O$, and 1.5 μL each of NheI and XhoI restriction enzymes. The mixtures were incubated overnight at 37 °C. The next day, the digested samples were separated using agarose gel electrophoresis and visualized under UV light as described above. Ligation reactions were set up using the digested and gel purified DNA inserts and vectors by aliquoting 3.5 μL of the pET-28a vector, 13.5 μL of the MCUR1 insert, and 2 μL of 10× T4 DNA ligation buffer into a microcentrifuge tube. This mixture was then heated for 45 s at 42 °C and immediately placed on ice for 5 min. Next, 1 μL of T4 DNA ligase (New England Biolabs) was added, and the mixture was placed in a 15 °C water bath overnight (~16 h).

The next day, the ligated products were transformed into DH5α *Escherichia coli* cells by mixing 7.5 μL of the ligation mixture with 100 μL of cells thawed on ice. Following incubation on ice for 60 min, the DNA-*E. coli* mixture was heat shocked at 42 °C for 45 s and immediately placed on ice for 3 min. Subsequently, 900 μL of Luria-Bertani (LB) broth was added to the heat-shocked microcentrifuge tube, and the ~1 mL mixture was transferred into a 15 mL sterile Falcon tube. The Falcon tube was incubated at 37 ºC with constant shaking at 200 rpm for 90 min. After this recovery period, the LB was transferred back into a microcentrifuge tube and centrifuged at 10,000 ×g for 10 min at ambient temperature. After removing ~900 μL of the supernatant, the resulting cell pellet was resuspended in ~100 μL of the remaining LB. Finally, the bacteria were plated on agar plates containing 60 μg ml$^{-1}$ kanamycin. The plates were incubated overnight at 37 °C in an air incubator.

The resultant colonies were screened for the presence of the pET-28a vector containing the inserts of interest by PCR. Approximately 4-5 colonies were individually suspended in 20 μL of $dH_2O$ contained in sterile microcentrifuge tube. Subsequently 9.5 μL of the colony suspension was added to 10 μL of 2× Taq Frogga Mix (FroggaBio) and supplemented with 0.25 μL (~250 ng) each of T7 forward and reverse T7 terminator primers. These PCR mixtures (i.e. one mixture for each colony screened) prepared in thin-walled PCR tubes were amplified using an initial denaturation cycle set of 95 °C for 3 min, followed by 32 cycles of denaturation at 95 °C for 1 min, annealing at 55 °C for 1 min, and extension at 72 °C for 1 min. A final extension was performed at 72 °C for 2 min (Table 2). Subsequently, the amplified mixtures were separated on a 1 % (w/v) agarose gel and visualized using EB as described above. Colonies which showed amplification of a product corresponding to the expected size of the target insert plus the additional flanking bp of the T7 forward and T7 reverse primers were considered positive, and the associated remaining colony suspension was transferred into 5 mL LB media supplemented with 60 µg ml$^{-1}$ kanamycin. This inoculated LB was cultured overnight at 37 °C with constant shaking at 200 rpm. The following day, the Presto Mini Plasmid Kit (GeneAid) was used to purify the pET-28a-MCUR1 vectors from the liquid culture as described by the manufacturer protocol. Finally, the isolated DNA was sent for sequencing at the Robarts DNA Sequencing Facility (London, ON) to confirm the pET-28a-MCUR1 vectors contained the insertion of interest in the correct pET-28a reading frame.

The MCUR1$_{161-230}$ and MCUR1$_{161-209}$ constructs were generated using a PCR-mediated mutagenesis protocol that used the sequenced pET-28a-MCUR1$_{161-338}$ construct as the template. Primers were designed to incorporate a STOP codon at the 210 (K210) and 231 (M231) residue for MCUR1$_{161-209}$ and MCUR1$_{161-230,}$ respectively (Table 1). For each construct, two separate mixtures for the forward and reverse reactions were prepared in thin-walled PCR tubes. Each mixture contained ~75 ng pET-28a-MCUR1$_{161-338}$ template in 0.5 µL, 4 µL 5× HF buffer, 0.4 µL of 10 mM dNTP mix, 14.45 µL dH$_2$O, ~125 ng forward or reverse primer in ~0.4 µL, and 0.25 µL Phusion DNA polymerase (Thermo Fisher Scientific). Mixtures were separately amplified using an initial denaturation cycle set of 98 °C for 30 s, followed by 5 cycles of denaturation at 98 °C for 15 s, annealing at 55.5 °C for 45 min, and extension at 72 °C for 3.5 min and a final temperature drop to 4 °C. After the 5 cycles of PCR, the forward and reverse reactions were quickly mixed together and subjected to a further 15 cycles of PCR using the same thermocycling parameters as was used for the individual primer amplifications, with the exception that a final 72 °C extension for 5 min was performed following the 15 cycles (Table 2).

To confirm that the amplification of the vector was successful, a 15 µL aliquot of the amplified product was electrophoresed alongside an equivalent amount of template DNA on a 1 % (w/v) agarose gel and visualized by EB staining as described above. A higher relative intensity for the PCR-amplified product compared to the vector template control lane which contained an equivalent amount of unamplified template was used as an indicator of a successful PCR reaction. Once the amplification was confirmed, 0.6 μL of DpnI restriction enzyme (New England Biolabs) was added to the remaining 25 μL of PCR mixture to digest the methylated template DNA and incubated at 37 °C for 3 h in an air incubator. The digested mixture is then transformed into DH5α *E. coli* cells as described above for the ligations. Approximately 3-4 colonies were selected from the plate after overnight incubation and inoculated into separate 15 mL Falcon tubes containing 5 mL LB media supplemented with 60 μg mL$^{-1}$ kanamycin. After overnight incubation at 37 °C with constant shaking at 200 rpm, plasmids were isolated using the Presto Mini Plasmid Kit (GeneAid) and sent for sequencing at Robarts DNA Sequencing Facility (London, ON) to confirm the vectors contained the mutations of interest in the correct pET-28a reading frame.

A similar mutagenesis protocol was followed for engineering each of the mutant pET-28a-MCUR1$_{161-338}$ and -MCUR1$_{161-209}$ constructs. The MCUR1$_{161-338}$ and MCUR$_{161-209}$ mutant constructs were generated targeting the residues identified in self-association interface of MCUR1$_{161-209}$ which includes A170R/L174R, V203R/Y204R, and C173P/L174P/L175P. Additional charge neutral A170S/174S and V203S/Y204S mutants were also generated for the MCUR1$_{161-209}$ construct. A MCUR1$_{161-338}$ mutant construct targeting the acidic residues (i.e. D315N/E318Q/E321Q) as a putative Ca$^{2+}$ binding site on the second coiled coil domain was also generated. Primers were designed to incorporate double and triple point substitution mutations as summarized in Table 1. The sequenced pET-28a MCUR1$_{161-338}$ and pET-28a MCUR1$_{161-209}$ constructs were used as template DNA for the respective MCUR1$_{161-338}$ and MCUR1$_{161-209}$ mutants (Table 2). Colony screening and sequencing was also performed for each of the mutant constructs as described above.

**Table 1. Oligonucleotide primers designed for generating constructs used in the research described in this thesis.**

| Primer | Sequence |
|---|---|
| **pET-28a MCUR1$_{161-338}$[a]** | 5’-CTAATCGCTAGCAGCAGGAAACTCTACTTCGACACTCATGCC-3’ |
| | 5’-GAGTAGCTCGAGCTATTTAATATTATCAAGCTTGTGTGACTCAAG-3’ |
| **pET-28a MCUR1$_{161-270}$[a]** | 5’-CTAATCGCTAGCAGCAGGAAACTCTACTTCGACACTCATGCC-3’ |
| | 5’-GAGTAGCTCGAGCTAATCTGTTCGGACTTTGATCACTTCATCCAT-3’ |
| **pET-28a MCUR1$_{161-230}$[b]** | 5’-GCGAATGTGAAAAAGGATtaGATTATTTTGGAGAAG-3’ |
| | 5’-CTTCTCCAAAATAATCtaATCCTTTTTCACATTCGC-3’ |
| **pET-28a MCUR1$_{161-209}$[b]** | 5’-CAAAGATATGGTCACCtAGATGCAGCAGGAAATC-3’ |
| | 5’-GATTTCCTGCTGCATCTaGGTGACCATATCTTTG-3’ |
| **pET-28a MCUR1$_{161-338}$ & MCUR1$_{161-209}$ A170R/L174R[b]** | 5’-CTACTTCGACACTCATcgCTTAGTGTGCagACTGGAAGACAATGGG -3’ |
| | 5’-CCCATTGTCTTCCAGTctGCACACTAAGcgATGAGTGTCGAAGTAG-3’ |
| **pET-28a MCUR1$_{161-338}$ & MCUR1$_{161-209}$ V203R/Y204R[b]** | 5’-GAGGCCAACATGGACATCcgCcgCAAAGATATGGTCACC-3’ |
| | 5’-GGTGACCATATCTTTGcgGcgGATGTCCATGTTGGCCTC-3’ |
| **pET-28a MCUR1$_{161-338}$ & MCUR1$_{161-209}$ C173P/L174P/L175P[b]** | 5’-GACACTCATGCCTTAGTGccCccAccGGAAGACAATGGGTTTGC-3’ |
| | 5’-GCAAACCCATTGTCTTCCggTggGggCACTAAGGCATGAGTGTC-3’ |
| **pET-28a MCUR1$_{161-209}$ A170S/L174S[b]** | 5’-CTACTTCGACACTCATagCTTAGTGTGCagcCTGGAAGACAATGGG-3’ |
| | 5’-CCCATTGTCTTCCAGgctGCACACTAAGctATGAGTGTCGAAGTAG-3’ |
| **pET-28a MCUR1$_{161-209}$ V203S/Y204S[b]** | 5’-GAGGCCAACATGGACATCagCagCAAAGATATGGTCACC-3’ |
| | 5’-GGTGACCATATCTTTGctGctGATGTCCATGTTGGCCTC-3’ |
| **pET-28a MCUR1$_{161-338}$ D315N/E319Q/E321Q[b]** | 5'-GCCCTTACCCAGACAaACAGGAAGATCcAAACTcAGGTTGCTGGCCTCAAA-3' |
| | 5'-TTTGAGGCCAGCAACCTgAGTTTgGATCTTCCTGTtTGTCTGGGTAAGGGC-3' |
| **T7 promoter[c]** | 5′-TAATACGACTCACTATAG-3′ |
| **T7 terminator[c]** | 5’-GCTAGTTATTGCTCAGCGG-3’ |

All primers were synthesized by Sigma-Aldrich (St. Louis, MO).
Nhe1 (forward) and Xho1 (reverse) restriction sites are underlined.
[a] subcloning primer
[b] mutagenesis primer
[c] sequencing primer

**Table 2. Summary of the PCR amplification parameters used for mutagenesis and construct cloning.**

| | **pET-28a MCUR$_{161-338}$ & MCUR1$_{161-270}$ subcloning** | | **pET-28a MCUR1$_{161-338}$ 209-STOP & 230-STOP mutagenesis** | | **pET-28a MCUR1$_{161-209}$ A170/L174 V203/Y204 C173/L174/L175 mutagenesis** | | **pET-28a MCUR1$_{161-338}$ A170/L174 V203/Y204 C173/L174/L175 mutagenesis** | | **pET-28a MCUR1$_{161-338}$ D315/E318/E321 mutagenesis** | |
|---|---|---|---|---|---|---|---|---|---|---|
| | 35 cycles | | 5 + 15 cycles | | 10 + 25 cycles | | 10 + 25 cycles | | 5 + 15 cycles | |
| | Temp (°C) | Time (s) | Temp (°C) | Time (s) | Temp (°C) | Time (s) | Temp (°C) | Time (s) | Temp (°C) | Time (s) |
| **Int. denaturation** | 98 | 60 | 98 | 30 | 98 | 60 | 98 | 60 | 98 | 30 |
| **Denaturation** | 96 | 30 | 98 | 15 | 98 | 45 | 98 | 45 | 98 | 15 |
| **Annealing** | 56[a] | 60 | 55.5[b] | 45 | 54-56 | 60 | 54-56 | 60 | 55.5 | 45 |
| **Extension** | 72 | 30 | 72 | 210 | 72 | 210 | 72 | 210 | 72 | 210 |
| **Final extension** | 72 | 120 | 72 | 300 | 72 | 300 | 72 | 300 | 72 | 300 |
| **Storage** | 4 | ∞ | 4 | ∞ | 4 | ∞ | 4 | ∞ | 4 | ∞ |

[a] Annealing temperature was 58 °C for MCUR1$_{161-338}$

[b] Annealing temperature was 56 °C for MCUR1$_{161-230}$

## 2.3 Protein expression and purification

The expression of all wild type and mutant MCUR1 constructs was carried out by transforming BL21(DE3) *E. coli* as described above for the DH5α transformations with the following modifications: first, the recovery period was 60 min in 900 μL of LB; second, no cell pelleting step was used; third, 150 μL of the diluted cells from the 1000 μL total cell suspension were plated. Cells were plated on an agar plate containing 60 μg ml$^{-1}$ kanamycin for selecting the viable colonies that had incorporated the desired construct. After overnight incubation of the plate at 37 °C in an air incubator, an individual colony was used to inoculate a starter liquid culture containing 25 mL LB supplemented with 60 μg ml$^{-1}$ kanamycin in a 250 mL Erlenmeyer flask. This starter culture was grown overnight at 37 °C with 190 rpm constant shaking. The 25 mL starter culture was then equally distributed into 4× 500 mL LB contained in 2 L Erlenmeyer flasks. The 500 mL of LB contained in each 2 L flask was supplemented with 60 μg mL$^{-1}$ kanamycin. These 2 L flasks were incubated at 37 °C with ~190 rpm constant shaking to promote the bacterial cell culture growth. Once the optical density at 600 nm ($OD_{600}$) reached ~0.6-0.8, cells were induced to express the protein of interest with the addition of isopropyl β-D-1-thiogalactopyranoside (IPTG) to a final concentration of 200 μM. The incubation temperature was reduced to ambient after the addition of the IPTG, and the cells were allowed to express for ~16 h. After this overnight incubation, the cells were harvested using a JA10 rotor in J2-21M induction drive centrifuge (Beckman, Inc.) at 7,250 ×g, 8 °C for 30 min. The resultant cell pellets were stored at -80 °C until protein purification.

Purification of the frozen cell pellets was carried out under denaturing conditions using solubilization buffer consisting of 6 M guanidine hydrochloride, 20 mM TRIS-HCl (pH 8.8), and 5 mM β-mercaptoethanol (BME). The cell pellet, corresponding to a ~5-7 mL wet volume held in a 50 mL conical tube, was manually homogenized using a transfer pipette in the presence of ~40 mL solubilization buffer. Once homogenized, the mixture in the conical tube was slowly rotated in a hybridization oven maintained at ambient temperature for 90 min to promote solubilization by mechanical mixing of the solution. Next, the mixture was centrifuged using a JA20 rotor in J2-21M induction drive centrifuge at 10,000 ×g, 8 °C for 50 min to separate the insoluble cell debris from the supernatant containing the soluble protein. The clarified supernatant (~40 mL) was subsequently incubated with 400 μL of a 50 % (v/v) nickel-nitrilotriacetic acid (Ni-NTA) agarose bead slurry (HisPur, ThermoFisher Scientific) and placed in the hybridization oven for end-over-end mixing at ambient temperature for 90 min. The Ni-NTA beads containing the 6×His-bound protein was captured by flowing the entire mixture through a gravity filtration column. To increase protein yield of precious $^{15}$N and/or $^{13}$C-labelled proteins (see below), the flow through (~40 mL) was remixed with 300 μL unused Ni-NTA beads and incubated in the hybridization oven as described above to extract any remaining unbound protein. The beads retained by the gravity filtration column were subsequently washed with 3× 15 mL wash buffer composed of 6M urea, 20 mM TRIS-HCl (pH 8.8), and 5 mM BME. After completion of the three washes, elution of the protein was carried out using 7× 3 mL of elution buffer composed of 6M urea 20 mM TRIS-HCl (pH 8.8), 5 mM BME, and 300 mM imidazole. Each 3 mL aliquot of elution buffer onto the beads in the gravity flow column was incubated for 90 s prior to flowing into a glass collection tube.

The presence of the protein in the eluted fractions was confirmed by separating aliquots of each fraction on a 15 % (w/v) SDS-PAGE gel, followed by Coomassie blue staining of the gel. Elution fractions containing the protein of interest based on migration in the gel relative to a set of protein standards were then pooled into a 3,500 Da dialysis membrane (BioDesign), and the bag was placed in 1 L refolding buffer composed of 20 mM TRIS (pH 8.8), 150 mM NaCl, and 1 mM dithiothreitol (DTT). After ~24 h of refolding at 4 °C and slow mixing with a magnetic stir bar, the 6×His tag was cleaved off the protein by adding ~1 U mg$^{-1}$ thrombin (Biopharm) into the dialysis bag and proceeding with dialysis at 4 °C for an additional 24 h. To confirm that the efficiency of the thrombin digestion was close to 100 %, a pre and post thrombin aliquot was separated on a 15 % (w/v) SDS-PAGE gel and visualized using Coomassie blue staining.

To achieve ~95 % purity, all MCUR1 proteins were further purified using size-exclusion gel chromatography (SEC) (Figure 3, 4, 5, and 6). The SEC was performed using a Superdex 200 10/300 GL column (GE Healthcare) connected to an AKTA Pure Fast

Purification Liquid Chromatography (FPLC) system (GE Healthcare). The running buffer used for SEC was composed of 20 mM HEPES, 150 mM KCl, 1 mM DTT, pH 7.5 for the $\mathrm{MCUR1}_{161\text{-}209}$, $\mathrm{MCUR1}_{161\text{-}230}$ and $\mathrm{MCUR1}_{161\text{-}270}$ proteins and pH 8.3 for $\mathrm{MCUR1}_{161\text{-}338}$. For this SEC purification step, the dialyzed/thrombin-digested samples were concentrated to ~1.5 – 2.0 mL using a 10,000 Da molecular weight cutoff Amicon Ultrafiltration concentrator (Millipore), and the SEC column was equilibrated with a minimum of 1 column volume of running buffer. The ~1.5 – 2.0 mL protein sample was injected onto the column in a single step, and the molecules were separated based on size using a flow rate of 0.5 mL $\mathrm{min}^{-1}$. Elution was monitored by UV absorbance at 280 nm and collected in 1 mL fractions. Aliquots of fractions which showed UV 280 nm absorbance were then separated on a 15 % (w/v) SDS-PAGE gel, and the gel was Coomassie stained to confirm the presence and purity of the protein of interest. Fractions which showed a single band migrating in the SDS-PAGE gel near the theoretical molecular weight of the monomer were pooled and stored at 4 °C for biophysical, biochemical and structural analyses performed within ~3 days or flash frozen in liquid nitrogen and housed at -80 °C for long term storage.

Protein concentrations for all proteins were routinely determined using the primary structure-derived UV extinction coefficients at 280 nm (Table 3).

The expression of uniformly single $^{15}$N- or $^{13}$C-labelled and double $^{15}$N, $^{13}$C-labelled samples was carried out using M9 minimal media in the place of LB. The M9 media was prepared by first making up M9 salts composed of 42 mM $\mathrm{Na_2HPO_4}$, 22 mM $\mathrm{KH_2PO_4}$, and 8.6 mM NaCl, pH 7.4 in 1 L of $\mathrm{dH_2O}$. This 1 L of M9 salts were sterilized by autoclaving for 20 min. On the day of protein expression, the M9 growth medium was prepared by supplementing the autoclaved M9 salts with additives (i.e. D-glucose, $\mathrm{NH_4Cl}$, $\mathrm{MgSO_4}$, $\mathrm{CaCl_2}$, thiamine and biotin) required for growth and expression using $\mathrm{NH_4Cl}$ and D-glucose as the primary nitrogen and carbon sources, respectively. The additives were pooled into a 50 mL conical tube and filtered directly into the M9 salts through a 0.2 μm syringe filter (Millipore). The final concentration of the additives in the 1 L of M9 media was 0.2 % (w/v) D-glucose (or $^{13}$C-D-glucose), 0.2 mg $\mathrm{ml}^{-1}$ $\mathrm{NH_4Cl}$ (or $^{15}$N-$\mathrm{NH_4Cl}$), 1 mM $\mathrm{MgSO_4}$, 1 μM $\mathrm{CaCl_2}$, 50 μM thiamine, and 1 μg $\mathrm{ml}^{-1}$ biotin.

Similar to the unlabeled expression, a 20 mL LB starter culture was grown at 37 °C overnight with 190 rpm constant shaking. The next day, the bacterial starter culture was centrifuged at 1,800 ×g for 15 min to pellet the cells and the LB media was decanted. The pelleted BL21 cells were subsequently resuspended gently in 10 mL of the M9 media and transferred into the bulk of the 1 L of M9 media contained within a 4 L flask. Cell growth, expression and purification was carried out as described for the unlabeled proteins above. Based on the observed ~95 % purity of the labelled samples after the thrombin digestion, as observed by the SDS-PAGE gel analysis, further purification steps following the dialysis into experimental buffer were not performed in order to minimize protein loss.

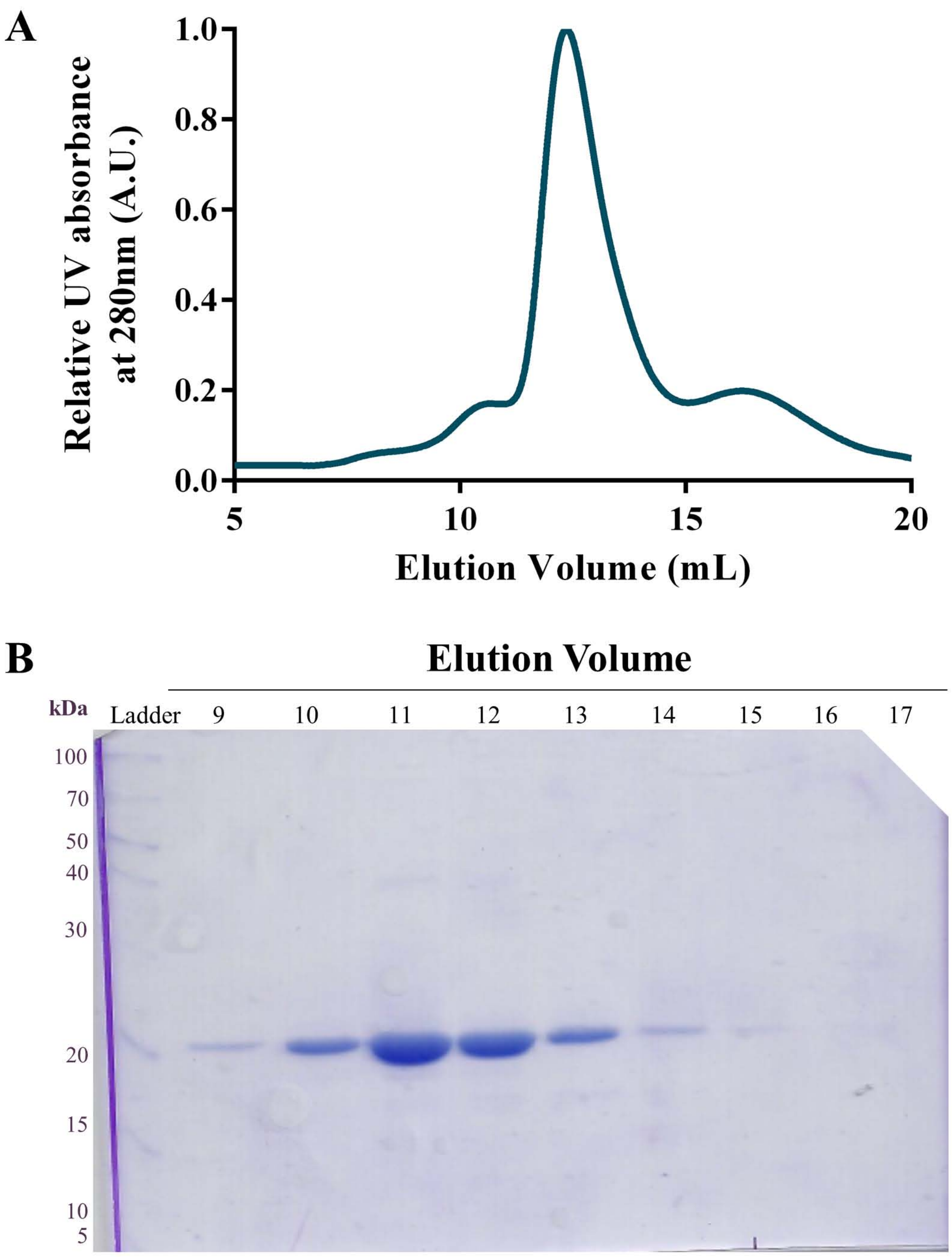

**Figure 3. Size exclusion chromatography elution profile of MCUR1$_{161\text{-}338}$.** Purification was carried out using a Superdex 200 10/300 GL (GE Healthcare) column. **A)** The elution profile was obtained by plotting the relative absorbance measured at 280 nm as a function of the column elution volume. **B)** A 15% (w/v) SDS-PAGE gel showing the protein in the elution fractions corresponding to the major elution peak. Coomassie blue R250 staining confirmed the presence of a band corresponding to the theoretical monomeric mass of MCUR1$_{161\text{-}338}$ (i.e. 21.2 kDa). The migration of the protein of interest is shown relative to the migration of the PageRuler™ Broad Range Unstained Protein Ladder standards in the first lane (ladder).

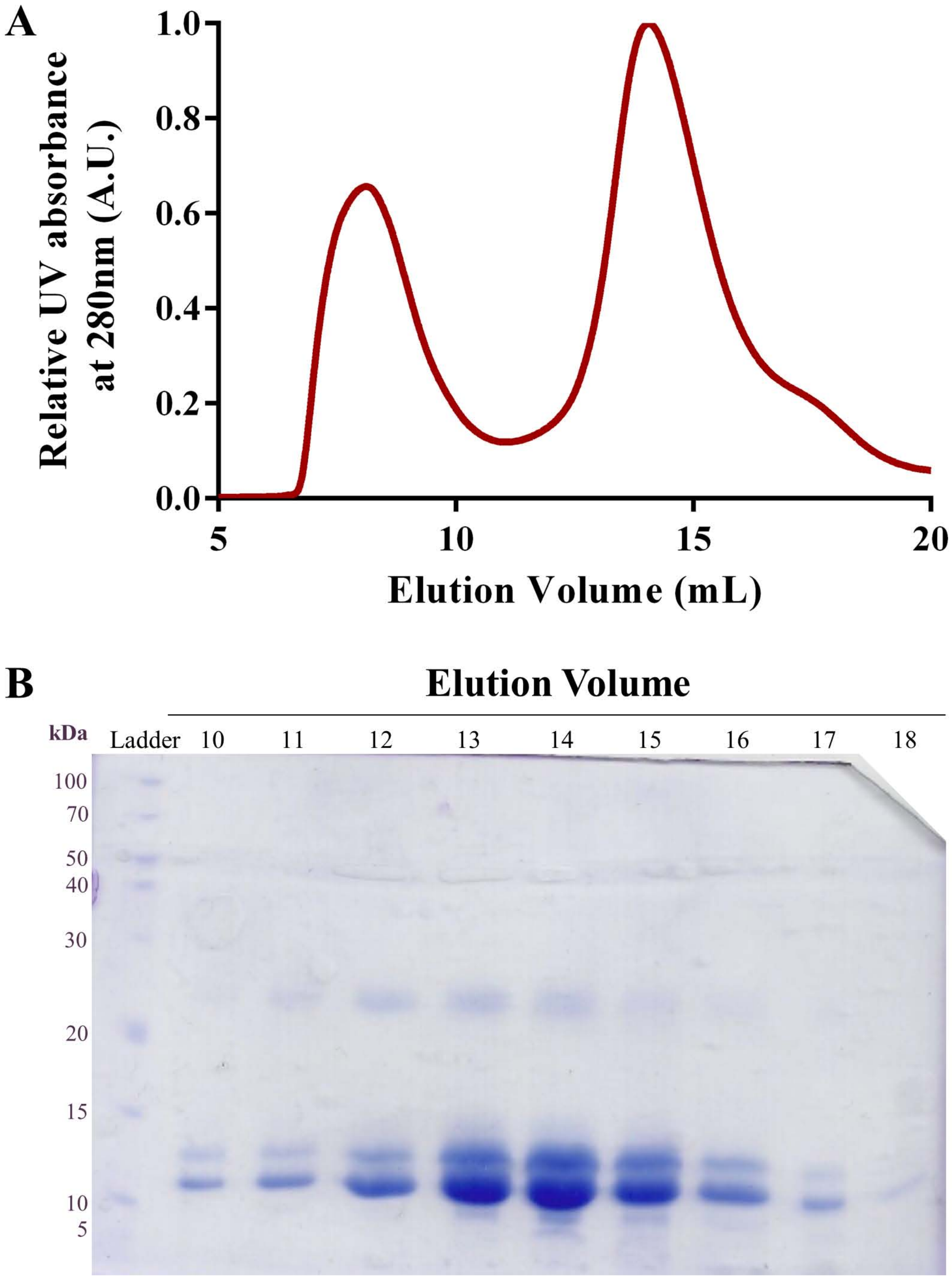

**Figure 4. Size exclusion chromatography elution profile of MCUR1$_{161\text{-}270}$.** Purification was carried out using a Superdex 200 10/300 GL (GE Healthcare) column. **A)** The elution profile was obtained by plotting the relative absorbance measured at 280 nm as a function of the column elution volume. **B)** A 15% (w/v) SDS-PAGE gel showing the protein in the elution fractions corresponding to the major elution peak. Coomassie blue R250 staining confirmed the presence of a band corresponding to the theoretical monomeric mass of MCUR1$_{161\text{-}270}$ (i.e. 13.3 kDa). The migration of the protein of interest is shown relative to the migration of the PageRuler$^{TM}$ Broad Range Unstained Protein Ladder standards in the first lane (ladder).

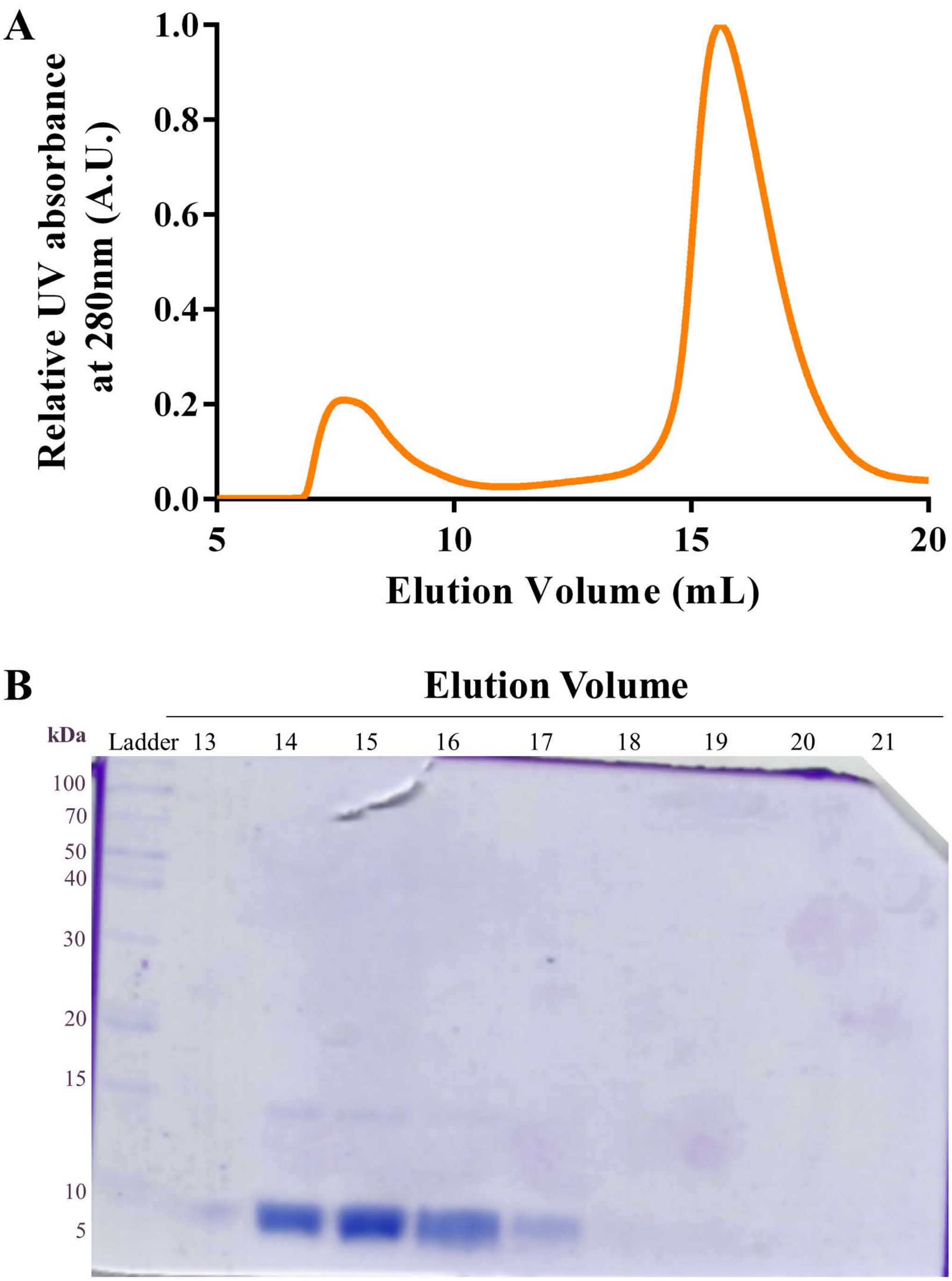

**Figure 5. Size exclusion chromatography elution profile of $\mathbf{MCUR1_{161\text{-}230}}$.** Purification was carried out using a Superdex 200 10/300 GL (GE Healthcare) column. **A)** The elution profile was obtained by plotting the relative absorbance measured at 280 nm as a function of the column elution volume. **B)** A 15% (w/v) SDS-PAGE gel showing the protein in the elution fractions corresponding to the major elution peak. Coomassie blue R250 staining confirmed the presence of a band corresponding to the theoretical monomeric mass of $\text{MCUR1}_{161\text{-}230}$ (i.e. 8.6 kDa). The migration of the protein of interest is shown relative to the migration of the PageRuler$^{\text{TM}}$ Broad Range Unstained Protein Ladder standards in the first lane (ladder).

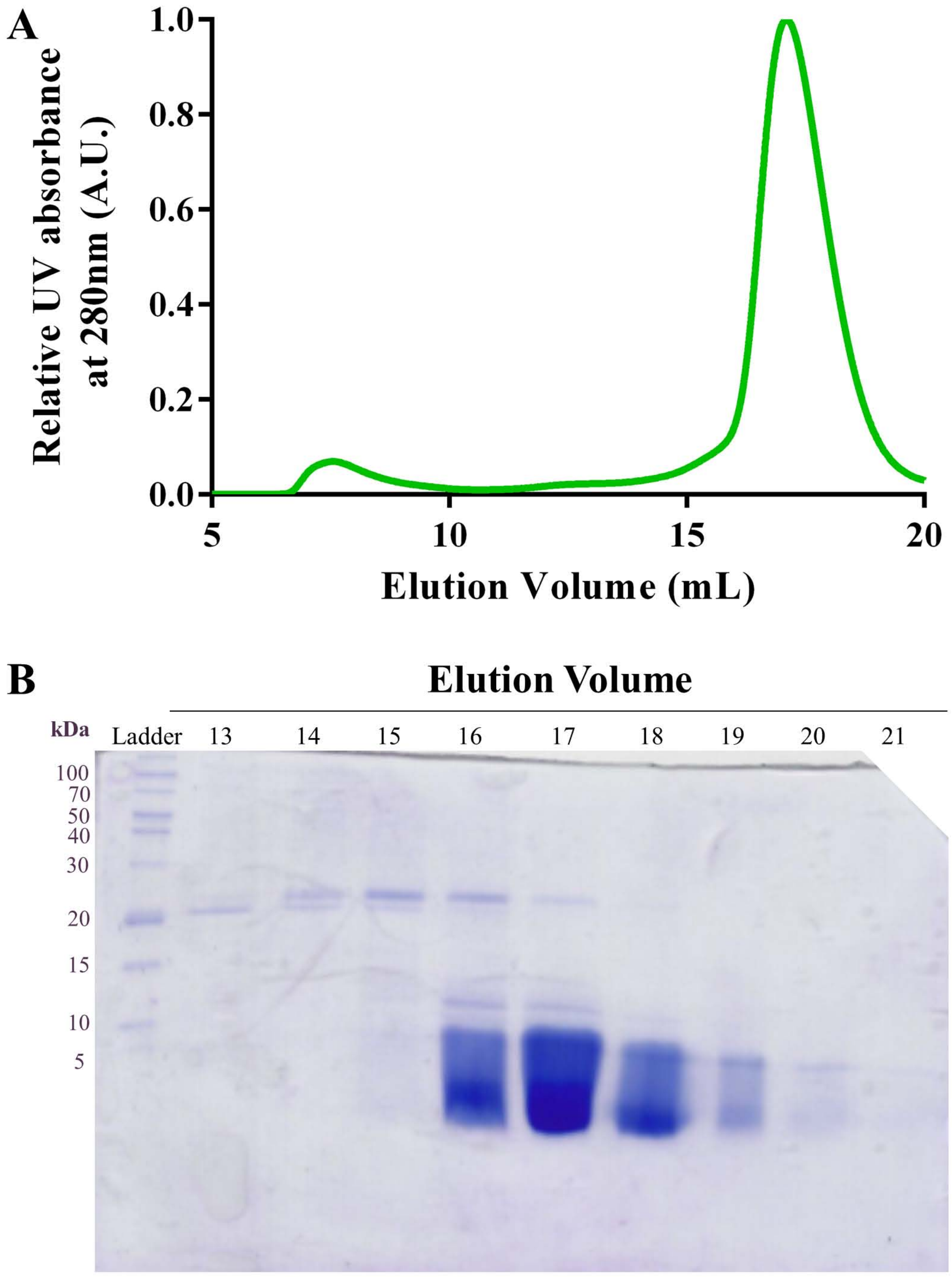

**Figure 6. Size exclusion chromatography elution profile of $\mathrm{MCUR1}_{161\text{-}209}$.** Purification was carried out using a Superdex 200 10/300 GL (GE Healthcare) column. **A)** The elution profile was obtained by plotting the relative absorbance measured at 280 nm as a function of the column elution volume. **B)** A 15% (w/v) SDS-PAGE gel showing the protein in the elution fractions corresponding to the major elution peak. Coomassie blue R250 staining confirmed the presence of a band corresponding to the theoretical monomeric mass of $\mathrm{MCUR1}_{161\text{-}209}$ (i.e. 6.1 kDa). The migration of the protein of interest is shown relative to the migration of the PageRuler$^{\mathrm{TM}}$ Broad Range Unstained Protein Ladder standards in the first lane (ladder).

**Table 3. Primary structure-based estimation of the biochemical properties of protein constructs.**

| Protein construct | Molecular weight (Da) | Extinction coefficient $((mg/mL)^{-1}cm^{-1})$ at 280 nm | Estimated pI |
|---|---|---|---|
| **MCUR1$_{161-338}$** | 21,233.6 | 0.1808 | 6.70 |
| **MCUR1$_{161-270}$** | 13,315.5 | 0.1923 | 5.88 |
| **MCUR1$_{161-230}$** | 8,578.9 | 0.2984 | 5.78 |
| **MCUR1$_{161-209}$** | 6,102.0 | 0.4195 | 5.12 |
| **MCUR1$_{161-338}$ A170R/L174R** | 21,361.7 | 0.1798 | 7.56 |
| **MCUR1$_{161-338}$ V203R/Y204R** | 21,283.7 | 0.1203 | 7.56 |
| **MCUR1$_{161-338}$ AC173P/L174P/L175P** | 21,195.5 | 0.1812 | 6.72 |
| **MCUR1$_{161-209}$ A170R/L174R** | 6,230.2 | 0.4109 | 6.53 |
| **MCUR1$_{161-209}$ V203R/Y204R** | 6,152.1 | 0.2081 | 6.53 |
| **MCUR1$_{161-209}$ AC173P/L174P/L175P** | 6,063.9 | 0.4222 | 5.12 |
| **MCUR1$_{161-209}$ A170S/L174S** | 6,092.0 | 0.4202 | 5.12 |
| **MCUR1$_{161-209}$ V203S/Y204S** | 6,013.9 | 0.1995 | 5.12 |
| **MCUR1$_{161-338}$ D315N/E319Q/E321Q** | 21,230.6 | 0.1809 | 8.08 |

Protein calculator v3.4 was used to obtain the predicted values.

## 2.4 Far-UV circular dichroism (CD)

Far-UV CD experiments were carried out in 20 mM HEPES, 150 mM KCl, 1 mM DTT at pH 7.5 for MCUR1$_{161-209}$, MCUR1$_{161-230}$ and MCUR1$_{161-270}$ constructs, and pH 8.3 for MCUR1$_{161-338}$ construct. The far-UV CD spectra and thermal melt measurements were conducted to determine the secondary structure and thermal stability of each construct, respectively. For each experiment 280 µL of 0.5 mg mL$^{-1}$ protein was placed in a 0.1 cm path length quartz cuvette. Data was acquired using the Jasco J-815 CD Spectrometer (Jasco, Inc.) equipped with a Jasco PTC-423S temperature control unit. Each spectral measurement was carried out as an average of 3 accumulations at 4 °C from 240 to 200 nm with 1 nm increments at 20 nm min$^{-1}$, an averaging time of 8 s, and a 1 nm bandwidth. Thermal melts were acquired by monitoring the changes at 222 nm while the temperature was increased from 4 to 95 °C at 1 °C min$^{-1}$ increments, using an averaging time of 8 s. To assess the effect of divalent cations on the secondary structure of the proteins, the Ca$^{2+}$ free spectra were acquired first, and then the spectral acquisition was repeated following the addition of 10 mM Ca$^{2+}$ into the same sample, which was also used for the Ca$^{2+}$ loaded thermal melt analysis. The cuvette was then extensively washed with 2 % (w/v) SDS and dH$_2$O, and a new aliquot of protein was used to obtain the Ca$^{2+}$ free thermal melt. Furthermore, spectra of the experimental buffers in the absence of protein were also acquired and subtracted from the protein CD signals to remove the buffer contributions. The analysis of thermal melts was conducted using GraphPad, where a Boltzmann sigmoidal fit was applied to each curve which exhibited a single unfolding transition to extract the apparent midpoints of temperature denaturation ($T_m$). For curves which showed two unfolding transitions, the curve was first normalized from 0 to 1 based on the apparent folded (i.e. set to 0) and unfolded (i.e. set to 1) baselines of the first transition, and the temperature where the fractional change was ~0.5 was taken as the first $T_m$ ($T_{m1}$). Subsequently the curve was normalized from 0 to 1 based on the apparent folded and unfolded transitions of the second transition, and the temperature where the fractional change was ~0.5 was taken as the second $T_m$ ($T_{m2}$).

## 2.5 Extrinsic 8-anilinonapthalene-1-sulfonic acid (ANS) fluorescence

The relative levels of solvent-exposed protein hydrophobicity were monitored by ANS binding and the associated changes in extrinsic ANS fluorescence. These extrinsic ANS fluorescence measurements were performed using a Cary Eclipse spectrofluorometer (Varian/Agilent, Inc) which was temperature equilibrated at 35 °C with a circulating water bath. Experimental buffers were as described above for the CD experiments. Each protein sample contained 600 μL of 0.15 mg mL$^{-1}$ protein, 50 μM ANS, and 0.1 mM EDTA placed in a quartz cuvette containing four clear sides. The excitation wavelength was set to 372 nm. The extrinsic ANS fluorescence emission spectra were acquired from 400 to 600 nm, with the photomultiplier tube (PMT) detector set at 660 V for MCUR1$_{161-338}$ and 690 V for MCUR1$_{161-270}$. Excitation and emission slit widths were set to 10 and 20 nm, respectively, for all ANS experiments. To monitor Ca$^{2+}$-induced changes in exposed hydrophobicity of the proteins, Ca$^{2+}$ was titrated into the samples between 1 to 80 mM with a 10 min incubation time between each incremental measurement. Buffer contributions to the ANS fluorescence were monitored by acquiring similar spectra in the absence of protein.

## 2.6 Size exclusion chromatography with in-line multi-angle light scattering (SEC-MALS)

SEC-MALS was performed to evaluate the quaternary structure of MCUR1 protein. A Superdex 200 Increase 10/300 GL column (GE Healthcare) connected to an AKTA Pure FPLC (GE Healthcare) was used for SEC and was placed in line with a DAWN HELEOS II (Wyatt Corp.) multi-angle light scattering (MALS) detector equipped with a 658 nm laser and an Optilab Trex differential refractometer (Wyatt Corp.) equipped with a 658 nm LED source. All systems were housed in a cold cabinet, maintaining the temperature at ~10 °C.

Experimental buffers were as described above for the CD experiments. The proteins were concentrated to ~6 mg mL$^{-1}$ using 10,000 Da molecular weight cutoff centrifugal concentrators and subsequently diluted using the experimental buffer for the 4 and 2 mg mL$^{-1}$ trials. The Superdex 200 Increase 10/300 GL column was equilibrated in the appropriate experimental buffer for at least 2 column volumes. Samples were centrifuged at 6,500 ×g for 10 min at 4 °C immediately before loading onto the column to remove insoluble particles. For each protein concentration, 100 μL of sample was injected onto the column via the manual 200 μL connected to the AKTA Pure system and moved through the system using a flow rate of 0.5 mL min$^{-1}$. The protein concentration through the eluted peaks was determined by the differential refractometer using a refractive index increment (dn/dc) of 0.185 mL g$^{-1}$. Molecular weights were calculated by Zimm plot analysis of the MALS signals and measured protein concentration using the ASTRA software (v6.1.5.22; Wyatt Corp.).

To probe the effect of divalent cations on the quaternary structures, the protein samples and the running buffers were supplemented with 10 mM $Ca^{2+}$ or 40 mM $Mg^{2+}$; further, the column was re-equilibrated as described above prior to sample injection. Additionally, a control experiment with ~2 mg ml$^{-1}$ bovine serum albumin (BSA) solubilized in experimental buffer (i.e. 20mM HEPES, 150 mM KCL, 1mM DTT, and pH 7.5) was injected to extract the normalizing constants at each MALS detector angle and for peak alignment of the refractive index and light scattering signals (Figure 7).

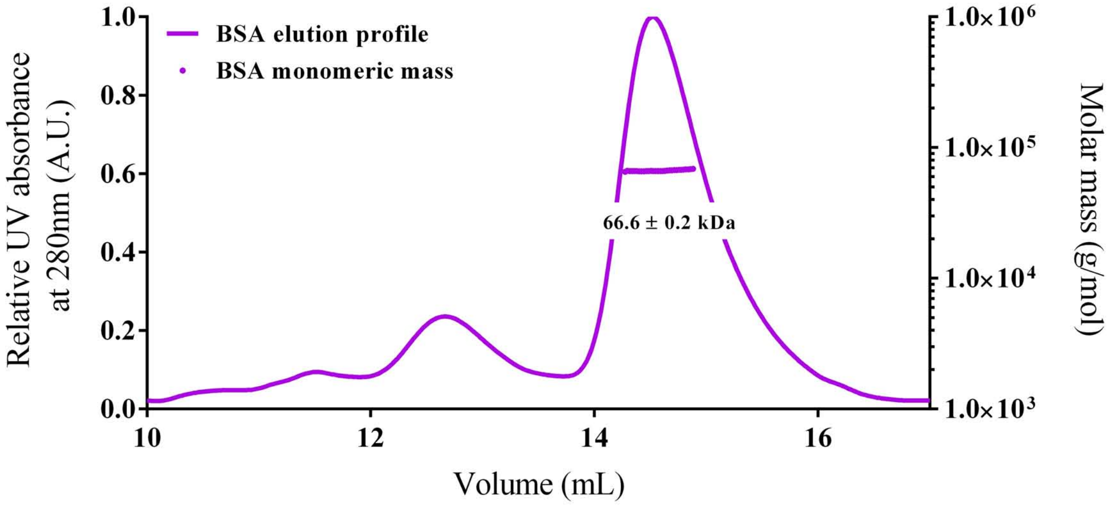

**Figure 7. SEC-MALS analysis of bovine serum albumin (BSA).** The MALS-determined monomeric mass of BSA was 66.6 kDa, showed closed circles (purple) under the major elution peak. The theoretical monomeric mass is 66.5 kDa. The multiple peaks observed at smaller elution volumes correspond to the higher order assembly of BSA. 100 µL of 2 mg/mL BSA in 20 mM HEPES, 150 mM KCl, 1 mM DTT, and pH 7.5 was injected onto the column. A.U., arbitrary units.

## 2.7 Structural elucidation using solution nuclear magnetic resonance (NMR) spectroscopy

All NMR experiments were carried out using the Varian INOVA 600 MHz magnet housed in the Biomolecular NMR facility at the University of Western Ontario. The characterization of MCUR1$_{161\text{-}209}$ by NMR required optimization of buffer conditions to obtain a $^{1}$H-$^{15}$N-heteronuclear single quantum coherence (HSQC) spectrum that provided intense amide H(N) peaks for all 55 amino acids which includes the non-native, N-terminal GSHMAS residues remaining after thrombin digestion. The initial buffer conditions were 20 mM HEPES, 150 KCl, and 1 mM DTT at pH 7.5, similar to the conditions used in the biophysical characterization experiments. However, reduced salt concentration and pH was found to improve the intensity and increase the number of H(N) peaks visible in the $^{1}$H-$^{15}$N-HSQC spectrum. Thus, the final NMR buffer was composed of 50 mM $NaH_2PO_4$ and 1 mM DTT at pH 6.5. All NMR experiments were carried out at 35 °C.

All NMR samples were prepared in a total of 600 μL and were composed of ~325 μM protein, 60 μM 4,4-dimethyl-4-silapentane-1-sulfonic acid (DSS), and 10 % (v/v) or 100 % $D_2O$. For the protein samples required in 100 % $D_2O$. The NMR samples were prepared as per usual to a volume of ~600 μL, and the $H_2O$ was subsequently evaporated overnight under centrifugation and vacuum using an Eppendorf Vacufuge housed at 4 °C (Eppendorf). This dried sample was then carefully resuspended in 600 μL of 100 % $D_2O$ for downstream NMR applications. The Wilmad thin walled (0.38 mm), 7-inch, 5 mm OD NMR tubes were used for the NMR experiments.

Backbone atom chemical shift assignments were obtained from $^{1}$H-$^{15}$N-HSQC, HNCO, CBCA(CO)NH and HNCACB experiments (S. Grzesiek & Bax, 1993; L. E. Kay et al., 2011; A. C. Wang et al., 1994). Furthermore, $^{1}$H-$^{13}$C-HSQC, (H)C(CO)NH-TOCSY and HCCH-TOCSY experiments were performed for side chain assignments (T. M. Logan et al., 1992; A. C. Wang et al., 1994). Finally, $^{15}$N-edited and $^{13}$C-edited NOESY-HSQC experiments were conducted to obtain the Nuclear Overhauser effect (NOE) restraints used to calculate the three dimensional (3D) solution structure of MCUR$_{161\text{-}209}$ (L. E. Kay et al., 1989). Table 4 provides a summary of the NMR experiments, dimensionality, protein labeling scheme, solvent conditions, and user-modified parameters for each NMR experiment performed.

All spectra were processed using NMRPipe, whereas the resonance assignments were made using computer aided resonance assignment (CARA) and NEASY (Bartels et al., 1995; Delaglio et al., 1995; Keller et al.). The online TALOS+ server was used to obtain the dihedral angle restraints based on the assigned chemical shifts (Shen et al., 2009). Hydrogen bond restraints were derived from the TALOS+ secondary structure output and using the online CSI 3.0 server based on the inputted chemical shift assignments (Shen et al., 2009; Wishart & Sykes, 1994). CYANA (v2.1) was used for automated NOE assignment and structure calculation based on ~91 % complete $^{1}$H chemical-shift assignments and 3D NOESY-HSQC-derived peaks (Guntert, 2004; Mal et al., 2002).

All structure images were rendered using PyMOL (Schrodinger, 2015).

**Table 4. Summary of the experimental parameters used for the solution NMR data acquisition.**

| Experiment | $^{1}$H frequency | $^{15}$N frequency | $^{13}$C frequency | $^{1}$H sw | $^{1}$H sw2 | $^{15}$N sw | $^{13}$C sw |
|---|---|---|---|---|---|---|---|
| **$^{1}$H-$^{15}$N-HSQC** | 599.3 | 150.7 | 60.7 | 8000 | - | 1994.3 | - |
| **$^{1}$H-$^{13}$C-HSQC** | 599.3 | 150.7 | 60.7 | 6499.8 | - | - | 14000 |
| **HNCO** | 599.3 | 150.7 | 60.7 | 8000 | - | 1944.3 | 3770.1 |
| **CBCACONH** | 599.3 | 150.7 | 60.7 | 8000 | - | 1944.3 | 10000 |
| **HNCACB** | 599.3 | 150.7 | 60.7 | 8000 | - | 1944.3 | 10000 |
| **CCCNNH-TOCSY** | 599.3 | 150.7 | 60.7 | 8000 | - | 1944.3 | 11000 |
| **HCCH-TOCSY** | 599.3 | 150.7 | 60.7 | 6499.8 | 6500 | - | 14000.7 |
| **$^{15}$N-edited NOESY** | 599.3 | 150.7 | 60.7 | 8000 | 8000 | 1944.3 | - |
| **$^{13}$C-edited NOESY** | 599.3 | 150.7 | 60.7 | 8000 | 6499.8 | - | 14000.7 |

| Experiment | nt | $^{1}$H points | $^{1}$H incr. | $^{15}$N incr. | $^{13}$C incr. | Labeling scheme | Solvent[#] | Refs |
|---|---|---|---|---|---|---|---|---|
| **$^{1}$H-$^{15}$N-HSQC** | 8 | 1024 | - | 64 | - | U-$^{15}$N | 90H/10D | a |
| **$^{1}$H-$^{13}$C-HSQC** | 48 | 1024 | - | - | 128 | U-$^{13}$C | 100D | a, b |
| **HNCO** | 32 | 1024 | - | 20 | 20 | U-$^{15}$N-$^{13}$C | 90H/10D | c, d, e, f |
| **CBCACONH** | 40 | 1024 | - | 20 | 44 | U-$^{15}$N-$^{13}$C | 90H/10D | g |
| **HNCACB** | 40 | 1024 | - | 20 | 44 | U-$^{15}$N-$^{13}$C | 90H/10D | e, f, h |
| **CCCNNH-TOCSY** | 48 | 1024 | - | 20 | 48 | U-$^{15}$N-$^{13}$C | 90H/10D | i |
| **HCCH-TOCSY** | 32 | 1024 | 44 | - | 32 | U-$^{13}$C | 100D | j, k |
| **$^{15}$N-edited NOESY** | 32 | 1024 | 48 | 32 | - | U-$^{15}$N | 90H/10D | a, l |
| **$^{13}$C-edited NOESY** | 24 | 1024 | 64 | - | 32 | U-$^{13}$C | 100D | m |

Where 'sw' and 'sw2' represents sweep widths, 'Nt' represents number of transients, and 'U' corresponds to uniform.

[#] Solvent percent composition of H and D corresponds to $H_2O$ and $D_2O$, respectively.

[a] (L. Kay et al., 1992)

[b] (John et al., 1993)

[c] (Ikura et al., 1990)

[d] (Stephan Grzesiek & Bax, 1992)

[e] (Muhandiram & Kay, 1994)

[f] (L. E. Kay et al., 1994)

[g] (Stephan Grzesiek & Bax, 1992)

[h] (Wittekind & Mueller, 1993)

[i] (Sattler et al., 1995)

[j] (L. E. Kay et al., 1993)

[k] (L. E. Kay et al., 1990)

[l] (Zhang et al., 1994)

[m] (Kupce, 1997)

### 2.7.1 Interface determination using paramagnetic resonance enhancement (PRE) NMR spectroscopy

To identify residues involved in mediating self-association of MCUR1$_{161\text{-}209}$, the single Cys at position 173 of MCUR1$_{161\text{-}209}$ was nitroxide spin tagged. The nitroxide spin-tagged MCUR1$_{161\text{-}209}$ was then mixed with uniformly $^{15}$N-labelled MCUR1$_{161\text{-}209}$ at a 1:1 ratio and simple $^{1}$N-$^{15}$N-HSQC spectra were acquired. The NMR-visible H(N) crosspeaks from the $^{15}$N-labelled MCUR1 subunits which were within ~10 Å of the nitroxide tag on unlabeled MCUR1 subunits exhibited a reduction in peak intensity due to the PRE effects of the nitroxide tag. Since the nitroxide-tagging was mediated by a 1-oxyl-2,2,5,5-tetramethyl-Δ3-pyrroline-3-methyl methanethiosulfonate (MTSL) functional group, 15 mM DTT was used to remove the resultant covalent disulfide linkage and provide a baseline spectrum with no PRE effects for comparison (Figure 8).

To nitroxide-tag the protein, 250 µL of 2.8 mg mL$^{-1}$ unlabeled MCUR$_{161\text{-}209}$ was dialyzed 2× in 1 L of 20 mM n-morpholino propanesulfonic acid (MOPS) buffer, 50 mM NaCl, and 0.1 mM TCEP-HCl, pH 8.3 at 4 °C. The dialyzed sample was then incubated in the dark for ~16 h at room temperature with a final concentration of 1.5 mM MTSL. Following this tagging procedure, the protein was dialyzed 2× in 1 L of 50 mM $NaH_2PO_4$, pH 6.5 at 4 °C, to remove any unreacted label and leave the sample in experimental buffer conditions. Concurrently, an equivalent amount of uniformly $^{15}$N-labelled MCUR1$_{161\text{-}209}$ was also dialyzed 2× in the same buffer conditions. Both samples were then mixed and left at room temperature in the dark for ~72 h to promote exchange of tagged and labelled monomers within dimer proteins. The 500 µL solution was then supplemented with 40 µL NMR buffer containing no DTT, 60 µM DSS, and 10 % (v/v) $D_2O$, to a final volume of 600 µL before acquiring a $^{1}$H-$^{15}$N-HSQC at 35 °C on the Varian INOVA 600 MHz NMR spectrometer. A second $^{1}$H-$^{15}$N-HSQC at 35 °C was acquired after the removal of MTSL nitroxide tag with the addition of 15 mM final DTT to the mixture. The peak intensities from the $^{1}$H-$^{15}$N-HSQC spectra acquired in the presence and absence of DTT were determined using NEASY in CARA (Bartels et al., 1995; Keller et al.). To map the interface, the H(N) crosspeak intensity ratios with and without DTT were ranked from lowest to highest, and the top 20 most broadened peaks were mapped on the surface of the $\mathrm{MCUR1}_{161\text{-}209}$ monomer structure.

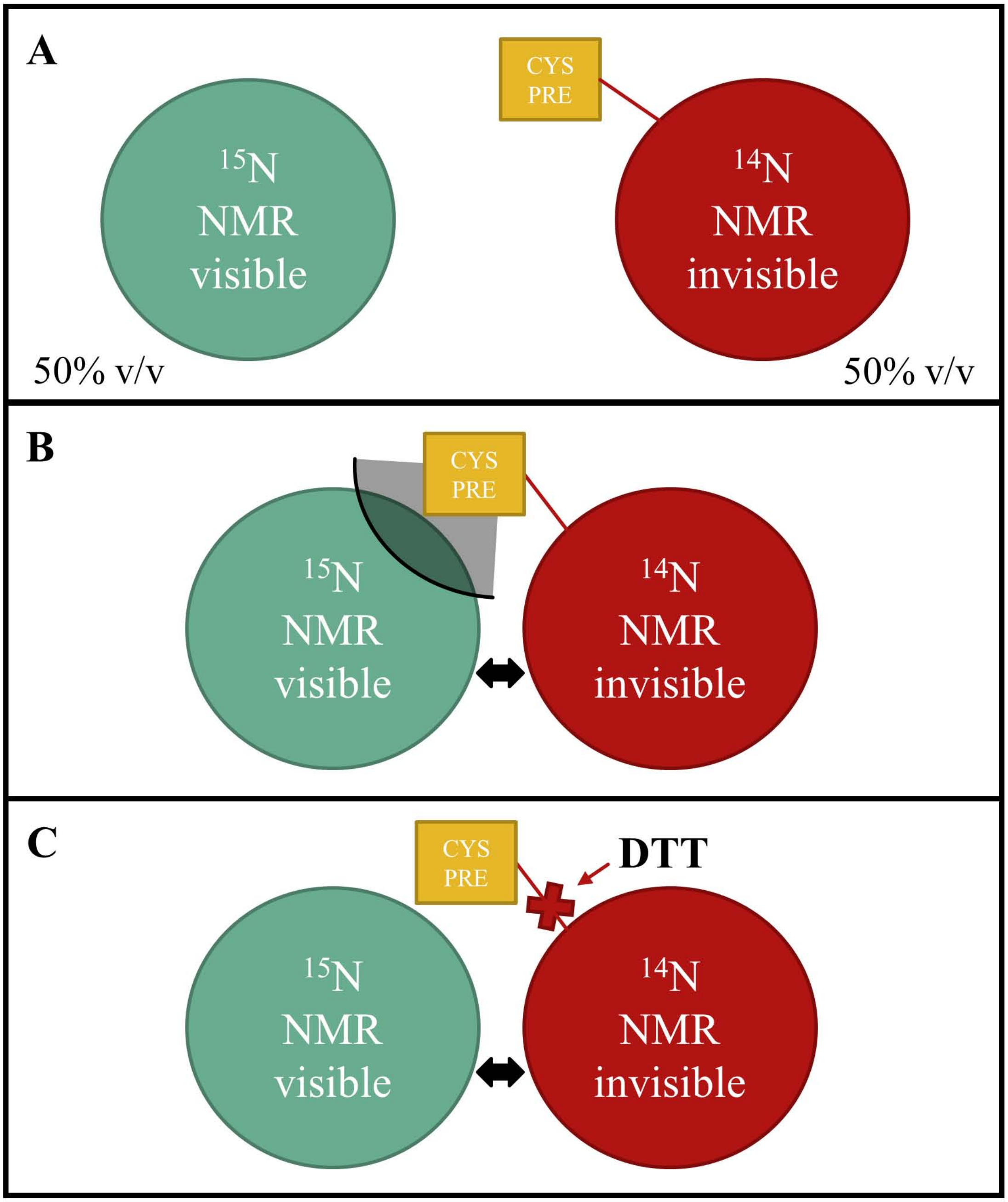

**Figure 8. Schematic representation of the PRE-NMR spectroscopy protocol.** The self association interface of MCUR1$_{161\text{-}209}$ was identified using PRE-NMR spectroscopy. **A)** Two distinct MCUR1$_{161\text{-}209}$ samples were prepared: a $^{15}$N-labelled MCUR1$_{161\text{-}209}$ and a nitroxide spin tagged $^{14}$N-MCUR1$_{161\text{-}209}$. The Cysteine residue at position 173 allowed for the nitroxide spin tagging mediated by the MTSL functional group. **B)** The two samples were mixed in a 1:1 ratio and a $^{1}$H-$^{15}$N-HSQC is acquired on the resultant mixture. Residues of the NMR visible $^{15}$N-MCUR1$_{161\text{-}209}$ sample found within ~10 Å of the MTSL tagged Cys173 experience peak broadening. **C)** Addition of 15 mM DTT serves to remove this MTSL tag as it reduces the disulfide covalent linkages. A final $^{1}$H-$^{15}$N-HSQC is performed in these reducing conditions to provide the baseline spectrum with no PRE-induced peak broadening.

# Chapter 3

# 3 Results

## 3.1 The conserved matrix region of MCUR1 is highly α-helical.

Currently, there is no high resolution structural information available on MCUR1. My research focused on the matrix-oriented structured region of MCUR1 since it represents the largest topological segment of the protein (Figure 1). Additionally, research from our group previously showed that matrix domain interactions with MCU can affect mitochondrial $Ca^{2+}$ uptake (S. K. Lee et al., 2016). According to PSIPRED, a bioinformatics tool that predicts the secondary structure of proteins using their amino acid sequence, the MCUR1 matrix domain between residue 161 – 338 is predicted to be predominantly α-helical. In contrast, residues ~85 – 160 are predicted to remain unstructured. Thus, I expressed and purified a series of MCUR1 matrix domain constructs encompassing the full structured region (i.e. residues 161-338), only one of the two putative coiled coil domains (i.e. residues 161-270), no putative coiled-coil domain (i.e. residues 161-230) and a minimal construct encompassing the most highly predicted α-helices with no coiled coil domain (i.e. residues 161-209); these constructs are named $\mathrm{MCUR1}_{161\text{-}338}$, $\mathrm{MCUR1}_{161\text{-}270}$, $\mathrm{MCUR1}_{161\text{-}230}$ and $\mathrm{MCUR1}_{161\text{-}209}$, respectively, in this thesis. I expressed and purified each of the corresponding proteins to > 95 % purity using an *E. coli* expression and purification strategy (see Materials and Methods).

To experimentally assess the level of secondary structure and confirm the PSIPRED predictions for each of these protein constructs, first, I conducted far-UV CD measurements on each protein (Figure 9A, 9B, 9C, 9D). Our results show two distinct minima in the far-UV CD spectra at ~ 208 and 222 nm for each protein construct. These minima indicate predominantly α-helical structures for all four protein constructs (Holzwarth & Doty, 1965). The most intense mean residue ellipticity (MRE) was observed for the $\mathrm{MCUR1}_{161\text{-}270}$ construct, probably due to the presence of the largest coiled coil domain (i.e. coiled coil-1 (CC1)) (Figure 2 and Table 5). MRE normalizes the

CD signal on a per residue basis, where more negative MRE signal at 208 and 222 nm indicates greater overall α-helicity.

Given the past work from our group showing that divalent cations such as $Ca^{2+}$ and $Mg^{2+}$ can regulate mitochondrial $Ca^{2+}$ uptake through MCU, I next assessed the level of secondary structure of each of the protein constructs in the presence of 10 mM $CaCl_2$ (S. K. Lee et al., 2016). At 4 °C where the CD spectra were acquired, the presence of $Ca^{2+}$ did not significantly change the MRE signal or shapes of the spectra. Overall, my far-UV CD data show that the MCUR1 matrix region primarily folds into α-helical configurations, and the level of α-helicity does not appear to be sensitive to high levels of $Ca^{2+}$.

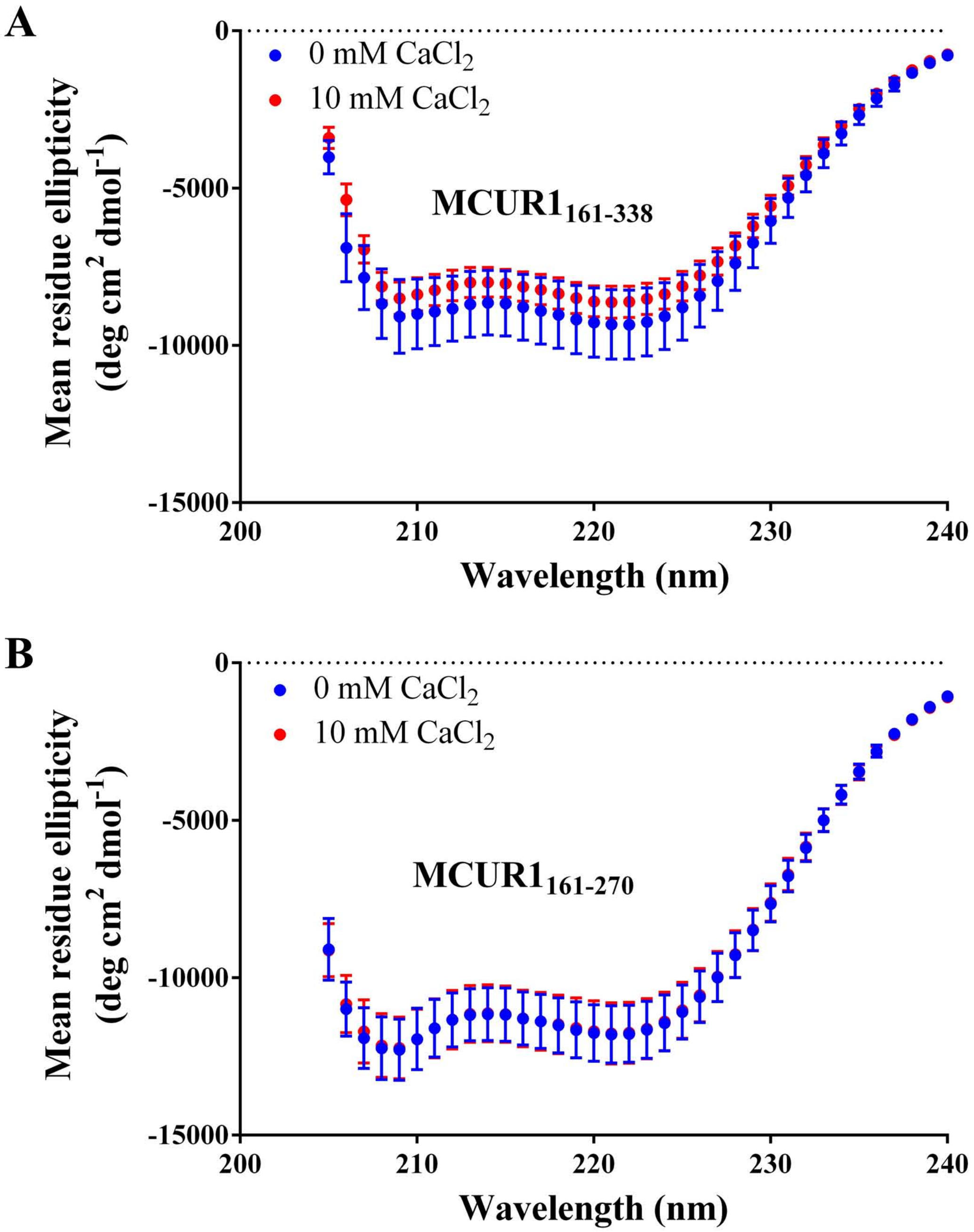
A
0
-5000
-10000
-15000
200
210
220
230
240
Mean residue ellipticity (deg cm$^2$ dmol$^{-1}$)
Wavelength (nm)
● 0 mM CaCl$_2$
● 10 mM CaCl$_2$
MCUR1$_{161\text{-}338}$
B
0
-5000
-10000
-15000
200
210
220
230
240
Mean residue ellipticity (deg cm$^2$ dmol$^{-1}$)
Wavelength (nm)
● 0 mM CaCl$_2$
● 10 mM CaCl$_2$
MCUR1$_{161\text{-}270}$

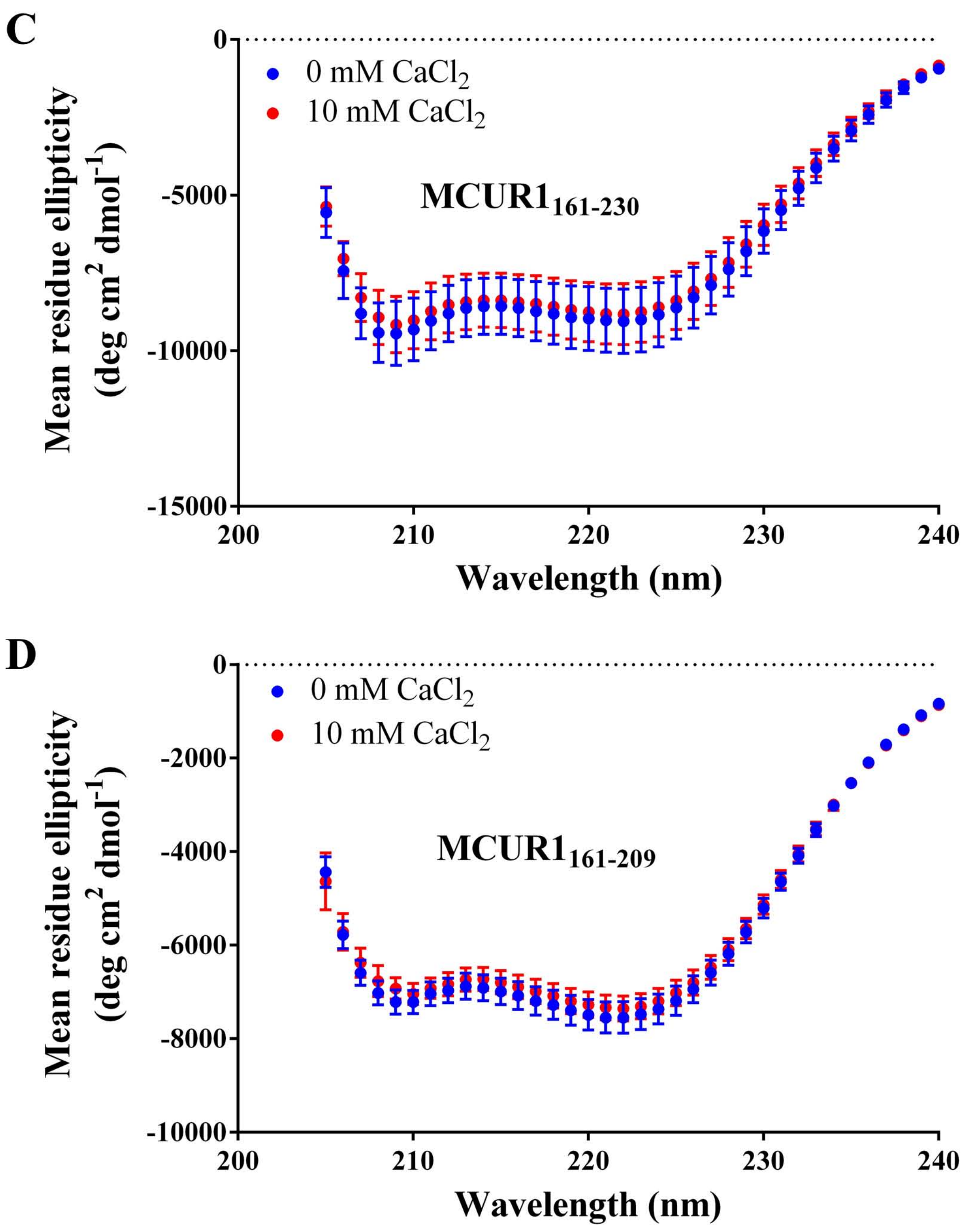

**Figure 9. Far-UV CD spectra of MCUR1 protein constructs in the presence and absence of $Ca^{2+}$.** Far-UV CD spectra were acquired for **A)** $MCUR1_{161\text{-}338}$, **B)** $MCUR1_{161\text{-}270}$, **C)** $MCUR1_{161\text{-}230}$ and **D)** $MCUR1_{161\text{-}209}$ protein constructs at 4 °C. All protein constructs showed distinct minima at 208 and 222 nm indicative of a high level of α-helical structure. Data were acquired in the absence (blue circles) or presence of 10 mM $CaCl_2$. All experiments were performed with 0.5 mg/mL protein in 20 mM HEPES, 150 mM KCl, 1 mM DTT, pH 7.5 ($MCUR1_{161\text{-}270}$, $MCUR1_{161\text{-}230}$ and $MCUR1_{161\text{-}209}$) or pH 8.3 ($MCUR1_{161\text{-}338}$). Data are means ± SEM of n=3 experiments.

## 3.2 The coiled coil domains destabilize the MCUR1 matrix region.

Having found that the MCUR1 matrix region is highly $\alpha$-helical, I next assessed the stability of each protein construct. I evaluated the change in far-UV CD signal at 222 nm as a function of temperature from 4 °C to 95 °C as an indicator of protein construct stability. Additionally, these thermal stabilities were semi-quantitated by determining the apparent midpoint of temperature denaturation ($T_m$), taken as the temperature causing a 50 % relative change in CD signal. Interestingly, the results show a dramatic ~+20 °C increase in apparent $T_m$ with the successive truncation of each coiled coil domain (Figure 10A, 10B, 10C). Thus, the minimal $MCUR1_{161-209}$ construct showed the highest stability with an apparent $T_m > 90$ °C (Figure 10D). Furthermore, the $MCUR1_{161-338}$ construct exhibited at least two distinct unfolding transitions, indicating that coiled coil-2 (CC2) may be unfolding independently from the other matrix domains. All other thermal melts, including $MCUR1_{161-270}$ containing CC1 showed only a single apparent unfolding transition.

Next, I assessed the thermal stability of each of the protein constructs in the presence of 10 mM $CaCl_2$. While high $CaCl_2$ levels did not affect the far-UV CD spectra of any of the protein constructs acquired at 4 °C, my thermal melts indeed revealed a sensitivity to the divalent cation. Both protein constructs containing coiled coils (i.e. $MCUR1_{161-338}$ with two coiled coils and $MCUR1_{161-270}$ with one coiled coil) exhibited altered thermal unfolding profiles (Figure 10A, 10B, and Table 5). The presence of 10 mM $CaCl_2$ caused $MCUR1_{161-270}$ to undergo a systematic shift in the single transition to lower temperatures, whereas $MCUR1_{161-338}$ displayed an apparent increase in the $T_m$ of the first transition and a decrease in the $T_m$ of the second transition in the presence of 10 mM $CaCl_2$. The $T_m$ values of my MCUR1 constructs lacking coiled coils were not affected by $CaCl_2$. Collectively, these thermal stability measurements suggest that the stability of the MCUR1 matrix region is sensitive to $CaCl_2$, and this sensitivity is primarily conveyed via the coiled coil domains.

**A**

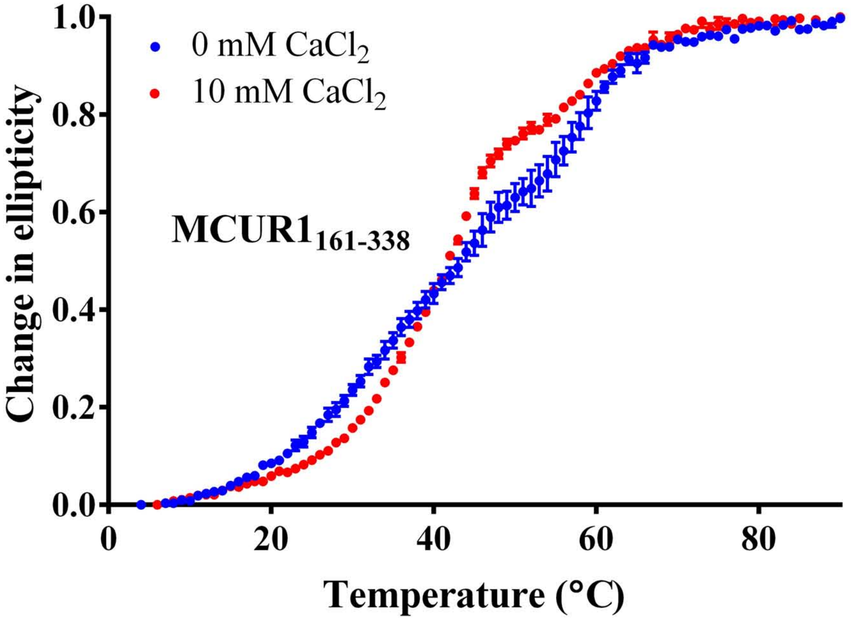
1.0
0.8
0.6
0.4
0.2
0.0
0
20
40
60
80
Change in ellipticity
Temperature (°C)
0 mM $CaCl_2$
10 mM $CaCl_2$
$MCUR1_{161-338}$

**B**

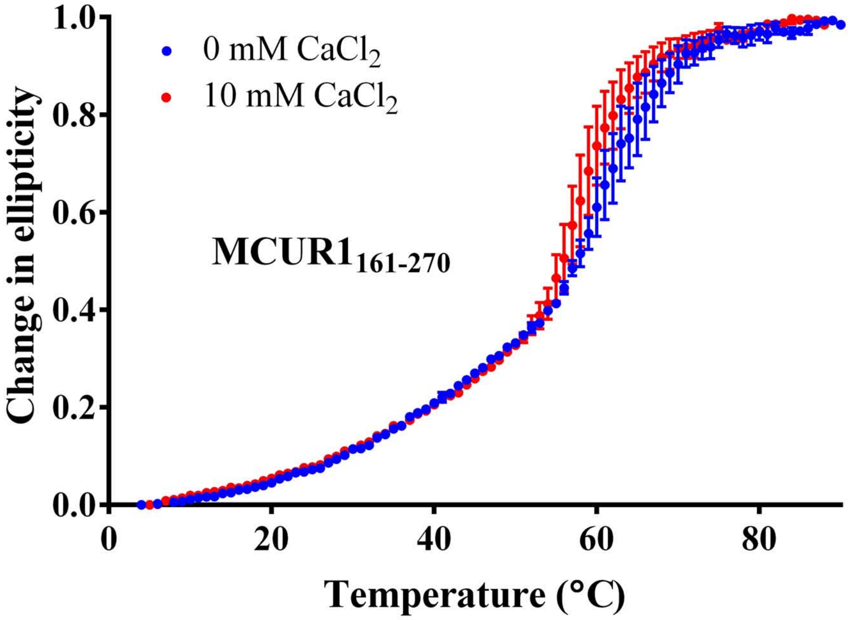
1.0
0.8
0.6
0.4
0.2
0.0
0
20
40
60
80
Change in ellipticity
Temperature (°C)
0 mM $CaCl_2$
10 mM $CaCl_2$
$MCUR1_{161-270}$

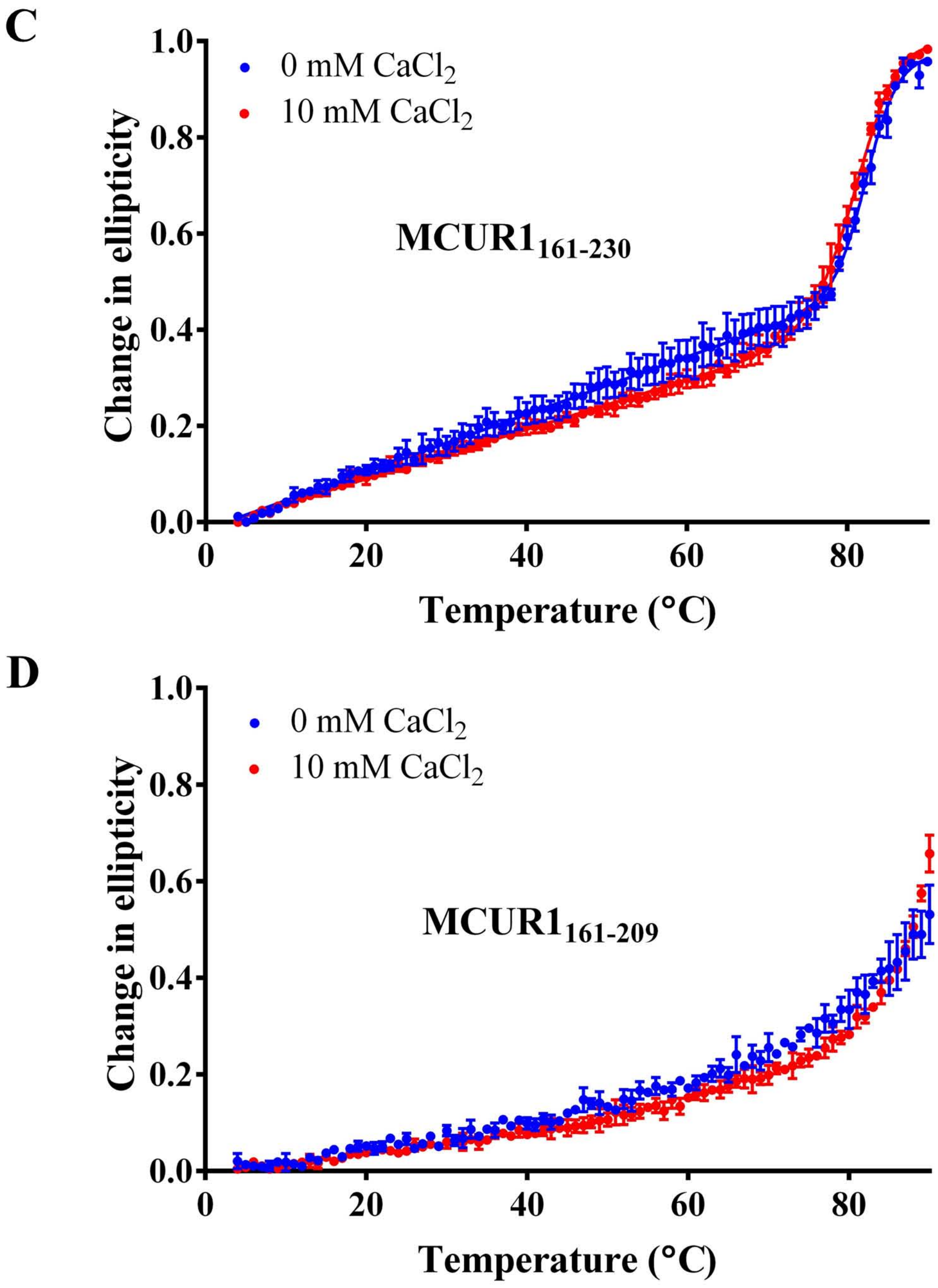

**Figure 10. Thermal stability of MCUR1 protein constructs in the presence and absence of Ca$^{2+}$.** Thermal melts were acquired for **A)** MCUR1$_{161-338}$, **B)** MCUR1$_{161-270}$, **C)** MCUR1$_{161-230}$ and **D)** MCUR1$_{161-209}$ protein constructs by monitoring the change in CD signal at 222 nm as a function of temperature. Data were acquired in the absence (blue circles) or presence of 10 mM CaCl$_2$. Increase in thermal stability are observed with the progressive loss of each coiled coil domain with very high thermal stabilities (i.e. > 80 °C) observed for MCUR1$_{161-230}$ and MCUR1$_{161-209}$. All experiments were performed with 0.5 mg/mL protein in 20 mM HEPES, 150 mM KCl, 1 mM DTT, pH 7.5 (MCUR1$_{161-270}$, MCUR1$_{161-230}$ and MCUR1$_{161-209}$) or pH 8.3 (MCUR1$_{161-338}$). Data are means ± SEM of n=3 experiments.

**Table 5. Thermal stabilities of the MCUR1 constructs in the presence and absence of $Ca^{2+}$ ions.**

| Construct | Putative coiled coils | $CaCl_2$ (10mM) | MRE at 222 nm (deg $cm^2$ $dmol^{-1}$) ($x10^3$) | Apparent $T_{m1}$ (°C) | Apparent $T_{m2}$ (°C) |
|---|---|---|---|---|---|
| **MCUR1 $_{161-338}$** | 2 | - | -9.3 ± 1.1 | 36.6 ± 5.3 * | ~ 58 ** |
| | | + | -8.6 ± 0.5 | 43.9 ± 0.5 * | ~ 58 ** |
| **MCUR1 $_{161-270}$** | 1 | - | -11.8 ± 0.9 | 61.6 ± 0.1 * | N/A |
| | | + | -11.7 ± 0.9 | 58.2 ± 0.1 * | N/A |
| **MCUR1 $_{161-230}$** | 0 | - | -9.0 ± 1.0 | 82.4 ± 0.4 * | N/A |
| | | + | -8.8 ± 1.0 | 81.8 ± 0.4 * | N/A |
| **MCUR1 $_{161-209}$** | 0 | - | -7.5 ± 0.3 | >90 ** | N/A |
| | | + | -7.5 ± 0.3 | >90 ** | N/A |

[*] Apparent midpoint of denaturation ($T_m$) values obtained using Boltzmann sigmoidal curve with sloping baselines

[**] Apparent $T_m$ estimated from the thermal melt curve

## 3.3 The MCUR1 matrix region self-association is influenced by the coiled coils.

Given that MCU functions as a higher order complex in the presence of MCUR1, I next assessed the quaternary structure of my MCUR1 matrix domain constructs. I utilized SEC-MALS to ascertain the quaternary structure for all four MCUR1 constructs because it provides a measure of molar mass, independent of elution volume which can be affected by particle shape and interactions with column resins. The largest $\text{MCUR1}_{161\text{-}338}$ construct containing both coiled coil domains eluted with a molecular weight of 66.2 ± 0.6 kDa which was ~3× the size of its theoretical monomeric molecular weight of 21.3 kDa (Figure 11A). Similarly, $\text{MCUR1}_{161\text{-}270}$ which contains CC1 also eluted with a molecular weight consistent with a homotrimer (Figure 11B and Table 6). In contrast, both $\text{MCUR1}_{161\text{-}230}$ and $\text{MCUR1}_{161\text{-}209}$ which contain no coiled coils showed a shift in the self-association equilibrium towards a dimer formation with the latter existing primarily as a homodimer (Figure 11C, 11D and Table 6). Experiments conducted with lower (i.e. ~2 mg $\text{mL}^{-1}$) and higher (i.e. ~6 mg $\text{mL}^{-1}$) protein concentrations yielded similar results indicating relatively high self-association affinities given the large dilution which occurs on the column (i.e. minimum ~20× dilution) (Table 6).

Despite observing a sensitivity in the thermal stability of the MCUR1 protein constructs containing coiled coils, the oligomerization state for all four constructs was not impacted by the presence of divalent cations. Specifically, the presence of 10 mM $CaCl_2$ or 40 mM $MgCl_2$ did not cause a significant shift in elution volume or the MALS-determined molecular weights for all four constructs (Figures 11A, 11B, 11C, 11D and Table 6). It should be noted that these SEC-MALS experiments were performed at 10 °C, and therefore, an effect of divalent cations on quaternary structure at physiological temperature cannot be ruled out. Collectively, my SEC-MALS data suggest that the MCUR1 matrix regions self-associate in solution with high affinity, and the coiled coils further potentiate this assembly into trimers.

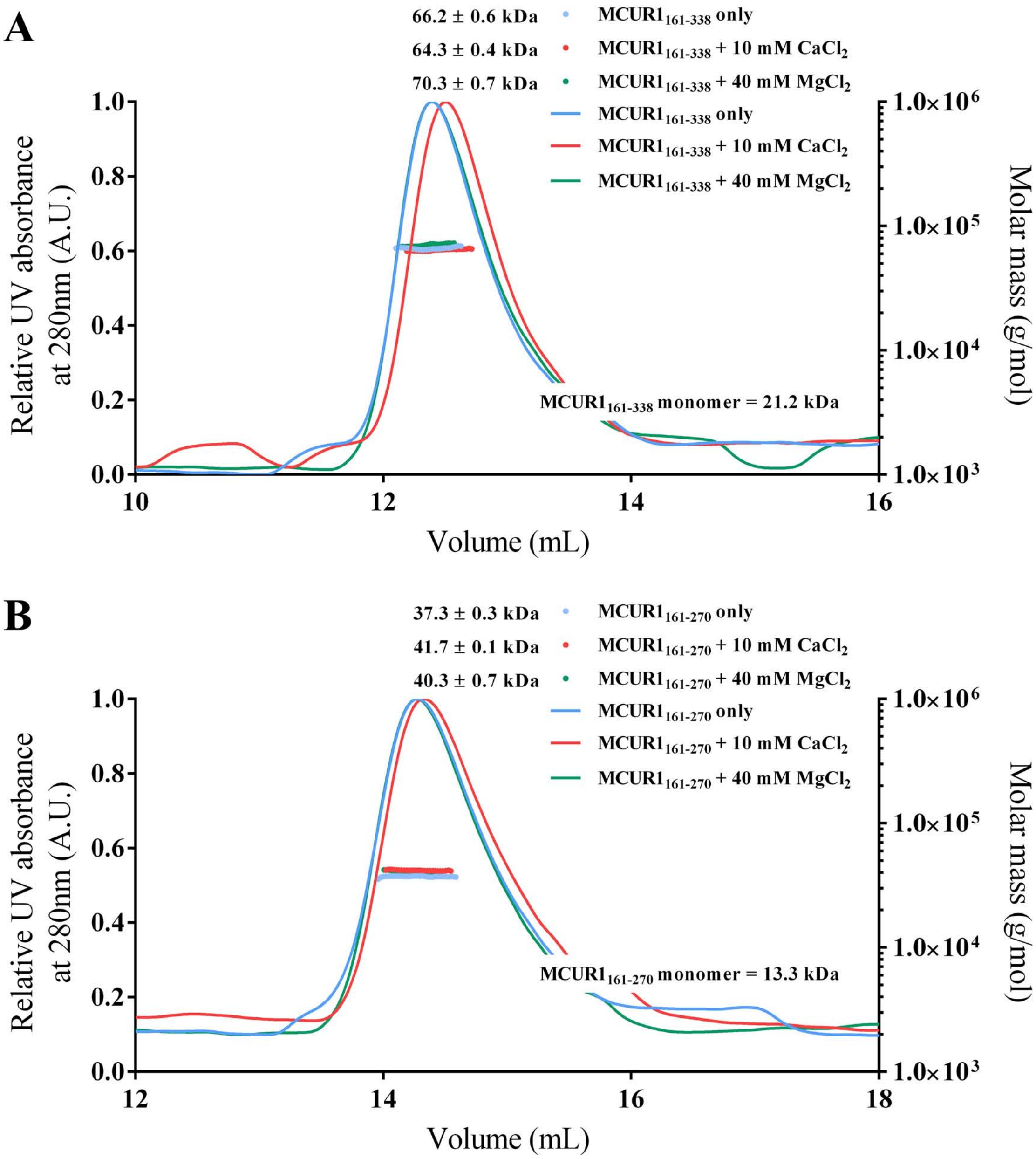
A
66.2 ± 0.6 kDa
64.3 ± 0.4 kDa
70.3 ± 0.7 kDa
MCUR1$_{161\text{-}338}$ only
MCUR1$_{161\text{-}338}$ + 10 mM CaCl$_2$
MCUR1$_{161\text{-}338}$ + 40 mM MgCl$_2$
MCUR1$_{161\text{-}338}$ only
MCUR1$_{161\text{-}338}$ + 10 mM CaCl$_2$
MCUR1$_{161\text{-}338}$ + 40 mM MgCl$_2$
MCUR1$_{161\text{-}338}$ monomer = 21.2 kDa
Relative UV absorbance at 280nm (A.U.)
Molar mass (g/mol)
Volume (mL)
0.0
0.2
0.4
0.6
0.8
1.0
$1.0\times10^3$
$1.0\times10^4$
$1.0\times10^5$
$1.0\times10^6$
10
12
14
16
B
37.3 ± 0.3 kDa
41.7 ± 0.1 kDa
40.3 ± 0.7 kDa
MCUR1$_{161\text{-}270}$ only
MCUR1$_{161\text{-}270}$ + 10 mM CaCl$_2$
MCUR1$_{161\text{-}270}$ + 40 mM MgCl$_2$
MCUR1$_{161\text{-}270}$ only
MCUR1$_{161\text{-}270}$ + 10 mM CaCl$_2$
MCUR1$_{161\text{-}270}$ + 40 mM MgCl$_2$
MCUR1$_{161\text{-}270}$ monomer = 13.3 kDa
Relative UV absorbance at 280nm (A.U.)
Molar mass (g/mol)
Volume (mL)
0.0
0.2
0.4
0.6
0.8
1.0
$1.0\times10^3$
$1.0\times10^4$
$1.0\times10^5$
$1.0\times10^6$
12
14
16
18

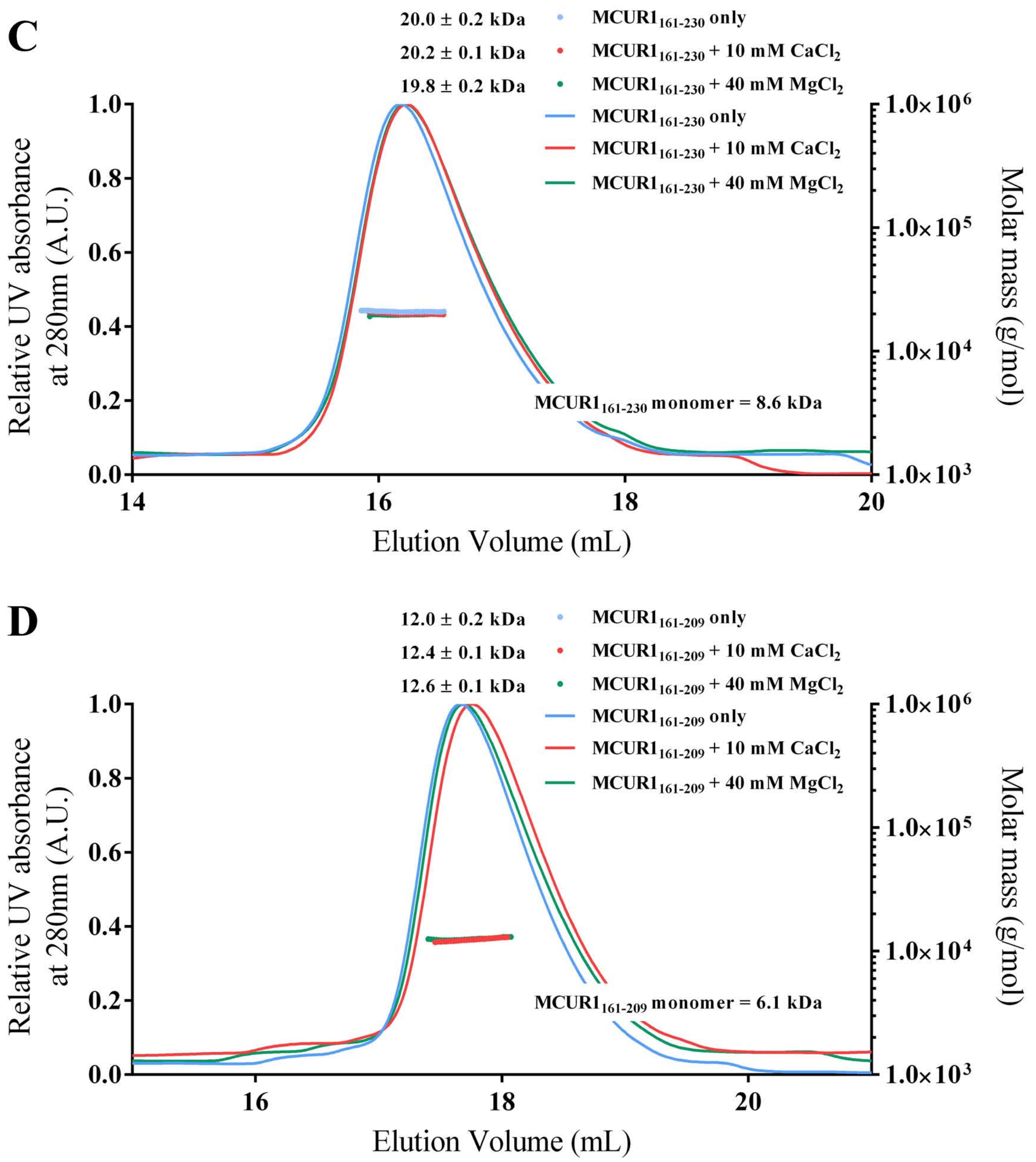

**Figure 11. Quaternary structure analysis of MCUR1 constructs using SEC-MALS.** SEC-MALS analysis of **A)** MCUR1$_{161-338}$, **B)** MCUR1$_{161-270}$, **C)** MCUR1$_{161-230}$ and **D)** MCUR1$_{161-209}$ protein constructs. The MALS-determined molecular weights calculated for each elution peak are shown under the peaks as closed circles. The presence of the coiled coils favours trimer assembly, while in the absence of the coiled coils the protein constructs primarily form dimers. Experiments performed in the presence of 10 mM CaCl$_2$ (red) and 40 mM MgCl$_2$ (blue) did not affect the quaternary structure in the protein concentration range tested. Data shown are of 100 μL injections of 4.0 mg/mL protein in 20 mM HEPES, 150 mM KCl, 1 mM DTT, pH 7.5 (MCUR1$_{161-270}$, MCUR1$_{161-230}$ and MCUR1$_{161-209}$) or pH 8.3 (MCUR1$_{161-338}$). Table 6 provides measurements for experiments conducted at 2 mg/mL and 6 mg/mL protein concentration. All experiments were conducted at 10 °C.

**Table 6. SEC-MALS analysis of MCUR1 constructs at various protein concentrations and in the absence and presence of $Ca^{2+}$ and $Mg^{2+}$ ions.**

| | Putative coiled coils | Theoretical monomeric weight (kDa) | Protein conc. (mg $mL^{-1}$) | $CaCl_2$ (10 mM) | $MgCl_2$ (40 mM) | MALS determined weight (kDa) | Stoichiometric ratio |
|---|---|---|---|---|---|---|---|
| MCUR1 $_{161-338}$ | 2 | 21.3 | 2.0 | - | - | 67.9 ± 2.9 | 3.2 |
| | | | 4.3 | | | 66.3 ± 0.6 | 3.1 |
| | | | 6.6 | | | 69.9 ± 0.5 | 3.3 |
| | | | 2.0 | + | - | 70.6 ± 2.3 | 3.3 |
| | | | 4.3 | | | 64.3 ± 0.4 | 3.0 |
| | | | 6.6 | | | Bad DRI | - |
| | | | 2.0 | - | + | 63.8 ± 0.9 | 3.0 |
| | | | 4.3 | | | 70.3 ± 0.7 | 3.3 |
| | | | 6.6 | | | Bad DRI | - |
| MCUR1 $_{161-270}$ | 1 | 13.3 | 2.0 | - | - | 40.6 ± 1.2 | 3.1 |
| | | | 4.0 | | | 37.3 ± 0.3 | 2.8 |
| | | | 6.9 | | | 41.5 ± 0.2 | 3.1 |
| | | | 2.0 | + | - | 41.8 ± 0.2 | 3.1 |
| | | | 4.0 | | | 41.7 ± 0.9 | 3.1 |
| | | | 6.9 | | | 39.8 ± 0.1 | 3.0 |
| | | | 2.0 | - | + | 36.5 ± 0.8 | 2.7 |
| | | | 4.0 | | | 40.3 ± 0.7 | 3.0 |
| | | | 6.9 | | | 41.3 ± 0.3 | 3.1 |
| MCUR1 $_{161-230}$ | 0 | 8.6 | 2.0 | - | - | 20.4 ± 0.2 | 2.4 |
| | | | 4.0 | | | 21.0 ± 0.2 | 2.4 |
| | | | 5.8 | | | 20.9 ± 0.2 | 2.4 |
| | | | 2.0 | + | - | 20.0 ± 0.3 | 2.3 |
| | | | 4.0 | | | 20.2 ± 0.2 | 2.3 |
| | | | 5.8 | | | 20.4 ± 0.2 | 2.4 |
| | | | 2.0 | - | + | 20.3 ± 0.5 | 2.4 |
| | | | 4.0 | | | 19.8 ± 0.2 | 2.3 |
| | | | 5.8 | | | 20.4 ± 0.2 | 2.4 |
| MCUR1 $_{161-209}$ | 0 | 6.1 | 2.0 | - | - | 11.8 ± 0.2 | 1.9 |
| | | | 4.0 | | | 12.0 ± 0.2 | 2.0 |
| | | | 5.9 | | | 12.0 ± 0.1 | 2.0 |
| | | | 2.0 | + | - | 13.0 ± 0.1 | 2.1 |
| | | | 4.0 | | | 12.4 ± 0.1 | 2.0 |
| | | | 5.9 | | | 12.5 ± 0.1 | 2.0 |
| | | | 2.0 | - | + | 13.1 ± 0.1 | 2.1 |
| | | | 4.0 | | | 12.6 ± 0.1 | 2.1 |
| | | | 5.9 | | | 12.8 ± 0.1 | 2.1 |

## 3.4 The MCUR1 matrix region coiled coils confer a divalent cation-dependent increase in exposed hydrophobicity.

Given my thermal stability measurements which showed a $Ca^{2+}$ sensitivity only for the constructs containing coiled coils, but no apparent change in secondary structure, I next examined the impact of divalent cations on the exposed hydrophobicity of these protein constructs. I used the extrinsic fluorescent probe ANS to evaluate the change in exposed hydrophobicity of $MCUR1_{161-338}$ and $MCUR1_{161-270}$ protein constructs in response to increasing levels of $CaCl_2$. Upon binding to solvent-exposed hydrophobic patches on proteins, ANS undergoes an increase in fluorescence intensity along with a concomitant decrease in the wavelength of the fluorescence emission maximum. $MCUR1_{161-338}$ showed a dramatic increase in ANS binding-induced fluorescence even after the addition of 1 mM $CaCl_2$. The ANS binding-induced fluorescence increase appeared to begin to saturate at ~40 mM $Ca^{2+}$ for $MCUR1_{161-338}$ (Figure 12A and 13). In contrast, the $MCUR1_{161-270}$ construct lacking the putative CC2, displayed a minimal change in exposed hydrophobicity in response to the titrated increase of $CaCl_2$ in the same concentration range as used for $MCUR1_{161-338}$ (Figure 12B and 13). Fluorescence emission spectra of buffer loaded with ANS in the absence of protein were much less intense and did not change in response to the addition of $CaCl_2$ (Figure 12A and 12B). Collectively, the ANS binding experiments suggest that $Ca^{2+}$ binding causes an increase in the exposed hydrophobicity of the MCUR1 matrix region, and that this $Ca^{2+}$-induced conformational change is dependent on the presence of CC2.

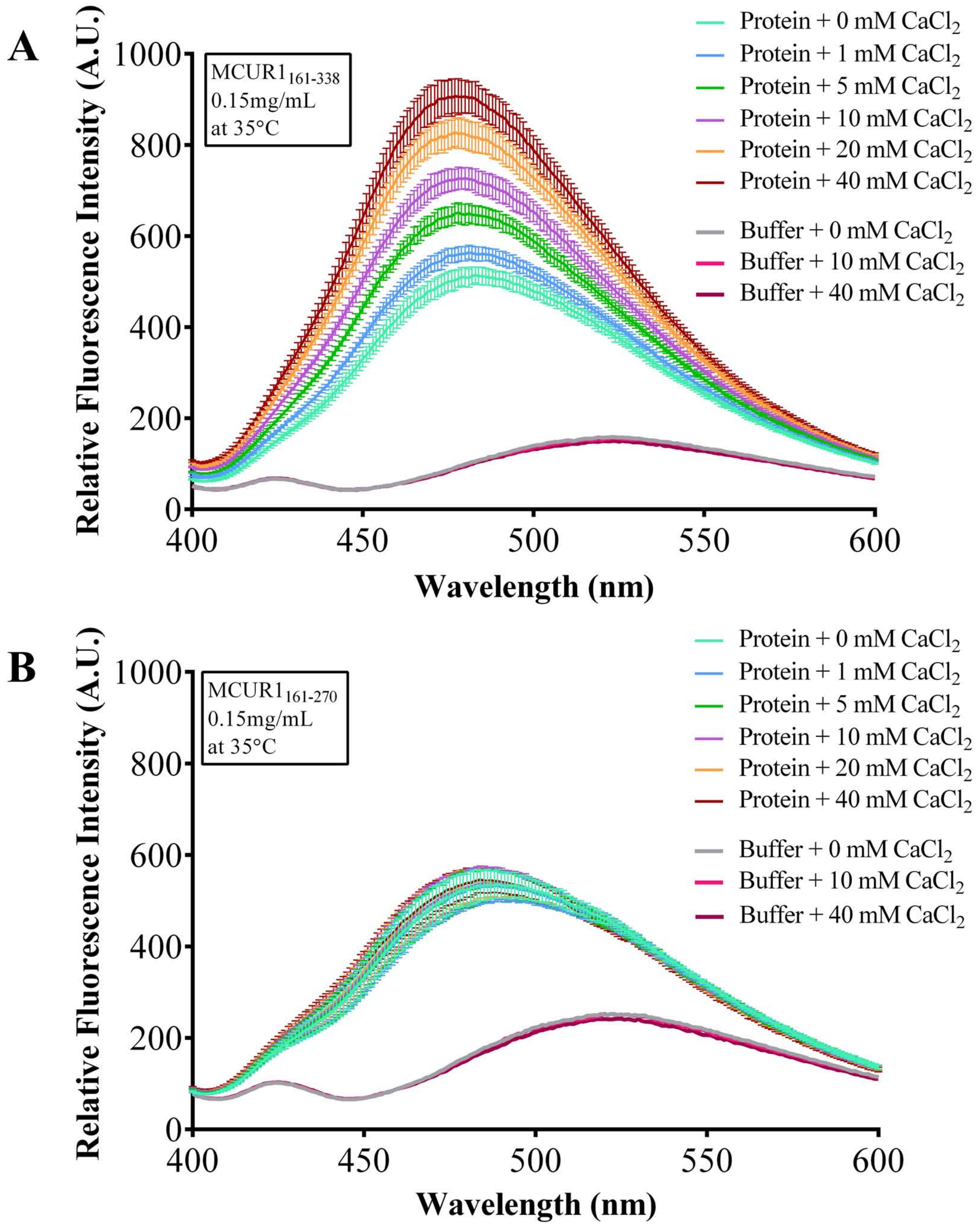

**Figure 12. Solvent exposed hydrophobicity analysis of the coiled-coil containing MCUR1 constructs using ANS fluorescence.** Extrinsic ANS binding-induced fluorescence emission spectra of **A)** MCUR1$_{161-338}$ and **B)** MCUR1$_{161-270}$ as a function of increasing CaCl$_2$ concentration. MCUR1$_{161-270}$ and MCUR1$_{161-338}$ protein constructs containing one or two coiled coils, respectively, caused enhanced ANS fluorescence intensity concomitant with a blue shift in the emission maximum. The addition of CaCl$_2$ caused enhanced ANS binding only for the MCUR1$_{161-338}$ construct. ANS fluorescence emission spectra acquired in the absence of protein are shown as controls. Data are means ± SEM of n=3 experiments.

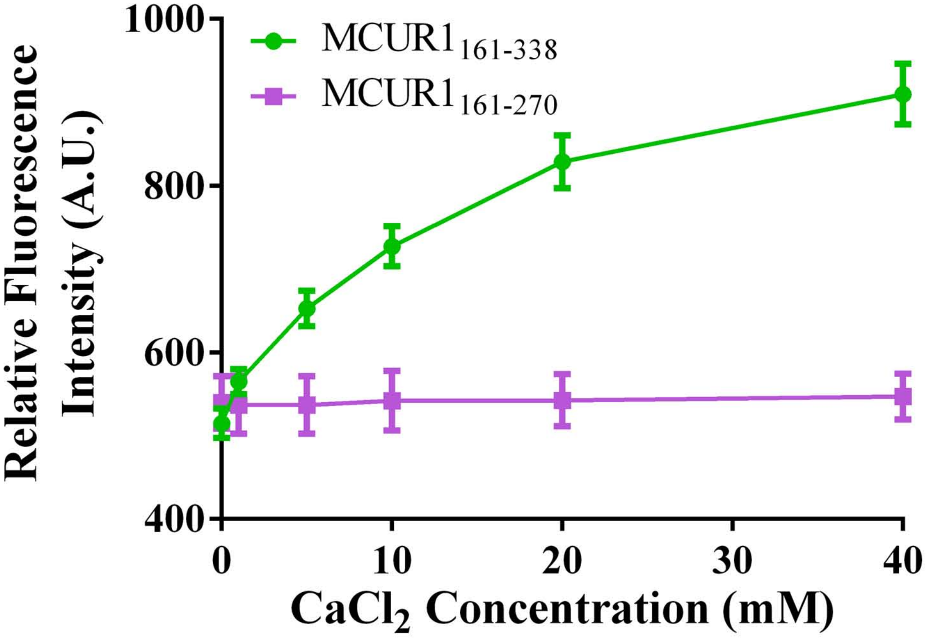

**Figure 13. Summary plot of the ANS fluorescence emission maxima induced by the coiled-coil containing MCUR1 constructs.** The maximum ANS fluorescence emission intensity induced by MCUR1$_{161\text{-}338}$ (green) and MCUR1$_{161\text{-}270}$ (purple) are plotted as a function of increasing CaCl$_2$ concentration. ANS binding to MCUR1$_{161\text{-}338}$ (green) showed a Ca$^{2+}$ sensitivity, while MCUR1$_{161\text{-}270}$ (purple) shows a minimal response to increases in Ca$^{2+}$. Data are means ± SEM of n=3 experiments.

## 3.5 $MCUR1_{161-209}$ is the most tractable construct for solution NMR structural analysis.

Given my observations that the MCUR1 matrix domains self-associates and the knowledge that MCU functions as a higher order heteromeric complex which includes MCUR1, I next aimed to reveal the first atomic resolution insights into the basis for the MCUR1 assembly due to its potential implications in these processes. Initially, I targeted and expressed uniformly $^{15}$N-labeleled $MCUR1_{161-270}$ due to its more NMR-tractable size. The $MCUR1_{161-338}$ construct was excluded from my solution NMR initiatives due to its relatively large size for standard NMR pulse sequences and the relatively low field strengths available. I screened numerous solvent conditions in an attempt to resolve all expected amide H(N) crosspeaks in $^{1}$H-$^{15}$N-HSQC spectra [i.e. one H(N) crosspeak expected per residue] of $MCUR1_{161-270}$. This optimization included the use of various detergents, salts, and buffers. Following this solution condition screening, the best $^{1}$H-$^{15}$N-HSQC was obtained using 12 mM deoxycholate at 35°C. This $MCUR1_{161-270}$ $^{1}$H-$^{15}$N-HSQC exhibited ~80% of the expected H(N) backbone cross peaks (Figure 14A); however, the spectrum showed poor resolution near the central ~7.5-8.5 $^{1}$H ppm region, as is typical of coiled coils (Schnell et al., 2005). Additionally, the $MCUR1_{161-270}$ spectrum and sample was not stable at 35°C for longer 3D experiments required for any high resolution structural elucidation.

Consequently, I next aimed to structurally elucidate the $MCUR1_{161-230}$ construct that is ~+20°C more thermally stable than $MCUR1_{161-270}$ (see above) and exists in an equilibrium between a homodimer and homotrimer. Unfortunately, the solvent optimization did not yield promising spectra likely due to the dimer-trimer equilibrium previously observed in our SEC-MALS. The unstable nature of either the dimer or trimer likely contributed to H(N) peak broadening and reduced spectral quality for the $MCUR1_{161-230}$ construct.

Finally, I focused on the $MCUR1_{161-209}$ construct which did not contain any coiled coil domain and showed a stable dimeric molecular weight close to the expected theoretical mass of ~12.2 kDa (Figure 11D and Table 6). The initial $^{1}$H-$^{15}$N-HSQC spectrum obtained for $MCUR1_{161-209}$ at 35°C in 20 mM HEPES, 150 mM KCl and pH 7.5 provided a higher quality spectrum [i.e. exhibiting most of the expected H(N) crosspeaks] compared to the other constructs, but still needed further solvent optimization to improve peak intensity homogeneity and to resolve all the expected H(N) crosspeaks (Figure 14B). Ultimately, the use of 50 mM $NaH_2PO_4$ buffer at pH 6.5 allowed the visualization of missing H(N) crosspeaks and provided more homogeneous intensities. Interestingly, the relative position of many of the well-resolved downfield H(N) crosspeaks in the ~8.6-9.0 $^1$H ppm range was similar for all three MCUR1 constructs evaluated by NMR, suggesting that a core structure was maintained in all contexts.

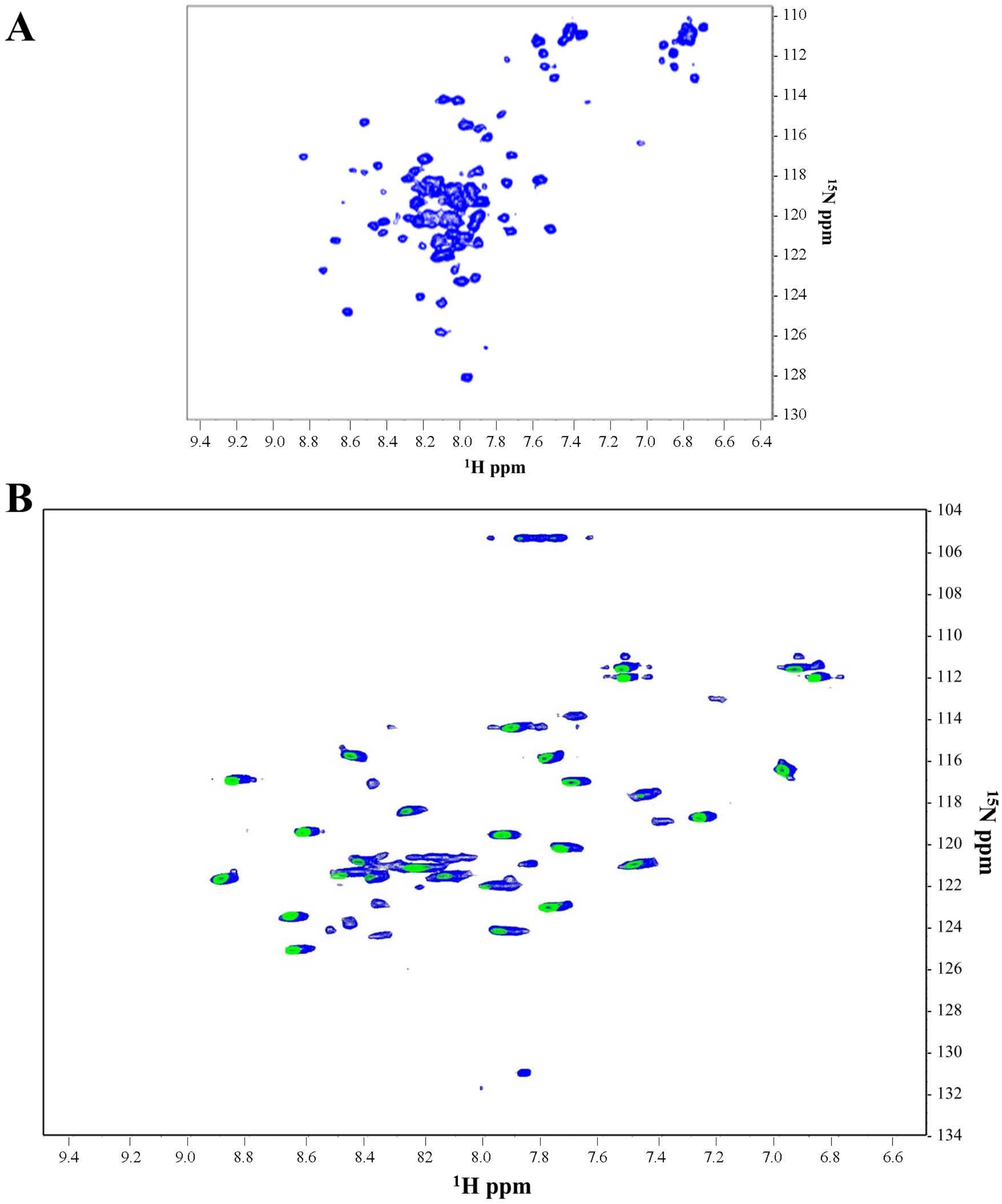

**Figure 14. Solution NMR $^1$H-$^{15}$N-HSQC spectra of the MCUR1$_{161\text{-}270}$ and MCUR1$_{161\text{-}209}$ constructs. A)** Representative $^1$H-$^{15}$N-HSQC spectrum of the MCUR1$_{161\text{-}270}$ construct acquired at 35 °C in 12 mM deoxycholate, 20 mM HEPES, 150 mM KCl, 1 mM DTT and pH 7.5. The poor peak dispersion in the central ~7.5-8.5 $^1$H ppm region and poor sample stability make high resolution structural determination by NMR improbable. **B)** Representative $^1$H-$^{15}$N-HSQC spectra of the MCUR1$_{161\text{-}209}$ construct. The $^1$H-$^{15}$N-HSQC acquired at 35°C in 20 mM HEPES, 150 mM NaCl, 1 mM DTT, and pH 7.5 (green crosspeaks) is shown overlaid with the $^1$H-$^{15}$N-HSQC acquired in 50 mM $NaH_2PO_4$, 1 mM DTT and pH 6.5 (blue crosspeaks).

## 3.6 The MCUR1$_{161-209}$ matrix region adopts a compact globular shape.

To solve the solution NMR structure of MCUR1$_{161-209}$, I prepared uniformly $^{15}N$, $^{13}C$-labeled MCUR1$_{161-209}$ protein and acquired a series of 3D NMR experiments aimed at assigning the backbone and side chain chemical shifts of each H, N and C atom. From these experiments (see Materials and Methods), I was able to assign ~91 % of the expected chemical shifts. Using distance-based NOESY and chemical shift-based torsion angle restraint derivations, I solved the high-resolution structure of MCUR1$_{161-209}$ with the CYANA 2.0 software (Table 7).

Overall, MCUR1$_{161-209}$ forms a compact triple-$\alpha$-helix structure with two loops (Figure 15). The backbone atom root mean square deviation (RMSD) for the 20 lowest energy structures is 0.9 Å and indicates a strong convergence of the restraints on a single conformation (Figure 15A). The compact structure consists of two nearly perpendicular $\alpha$-helices ($\alpha 1$: residues 166-177 and $\alpha 2$: residues 182-198). A third short helix ($\alpha 3$: residues 202-204) forms at the C terminal end of the protein (Figure 15B). A loop region joins $\alpha 1$ with $\alpha 2$ (L1: residues 178-181). Whereas, a second shorter linker joins the small $\alpha 3$ with the longer centrally located $\alpha 2$ (L2: residues 199-201) (Figure 15B). The 3D arrangement of the helices allows for close contacts between $\alpha 1$ and $\alpha 3$. Nevertheless, obtaining the chemical shift assignments at the C-terminal region were challenging, likely due to the dynamic nature of $\alpha 3$. These dynamics were supported by the systematically smaller order parameters ($S^2$) derived for the C-terminal residues based on the chemical shift information (Figure 15C).

**Table 7. Solution NMR structure statistics for the MCUR1$_{161-209}$ construct.**

| **All atom completeness of resonance assignments (%)** | | |
|---|---|---|
| H, N, C, O | 91 | |
| **Conformationally restricting restraints** | | |
| Total | 382 | |
| short range (\|i-j\|≤1) | 180 | |
| Medium range (1<\|i-j\|<5) | 107 | |
| Long range (\|i-j\|≥5) | 95 | |
| **Dihedral angle restraints** [a] | | |
| Phi | 44 | |
| Psi | 44 | |
| Hydrogen bond restraints | 23 | |
| **Residual restraint violations** [b] | | |
| Average number of distance violations per structure: | | |
| 0.1-0.2 Å | 0.95 | |
| 0.2-0.5 Å | 1.95 | |
| >0.5 Å | 0.20 | |
| Largest distance violation (Å) | 0.77 | |
| Average number of dihedral angle violations per structure: | | |
| 1-10 (degrees) | 0.65 | |
| >10 (degrees) | 0.10 | |
| Largest dihedral angle violation (degrees) | 17.22 | |
| **Model quality** [c] | **Global** [e] | **Ordered** [f] |
| RMSD backbone atoms (Å) | 0.90 | 0.10 |
| RMSD heavy atoms (Å) | 1.40 | 0.80 |
| RMSD bond lengths versus ideal (Å) | 0.00 | 0.00 |
| RMSD bond angles versus ideal (degrees) | 0.20 | 0.20 |
| **Ramachandran statistics** [d] | | |
| Residues in most favoured regions (%) | 90.6 | 97.1 |
| Residues in allowed regions (%) | 9.1 | 2.9 |
| Residues in generously allowed regions (%) | 0.2 | 0.0 |
| Residues in disallowed regions (%) | 0.0 | 0.0 |

[a] Derived from the chemical shift assignments using TALOS-N (Shen & Bax, 2015).

[b] Violations were identified if they occurred in 6 or more structures out of the 20 structure ensemble.

[c] Calculated by the Protein Structure Validation Server (PSVS-1.5) (Bhattacharya et al., 2007).

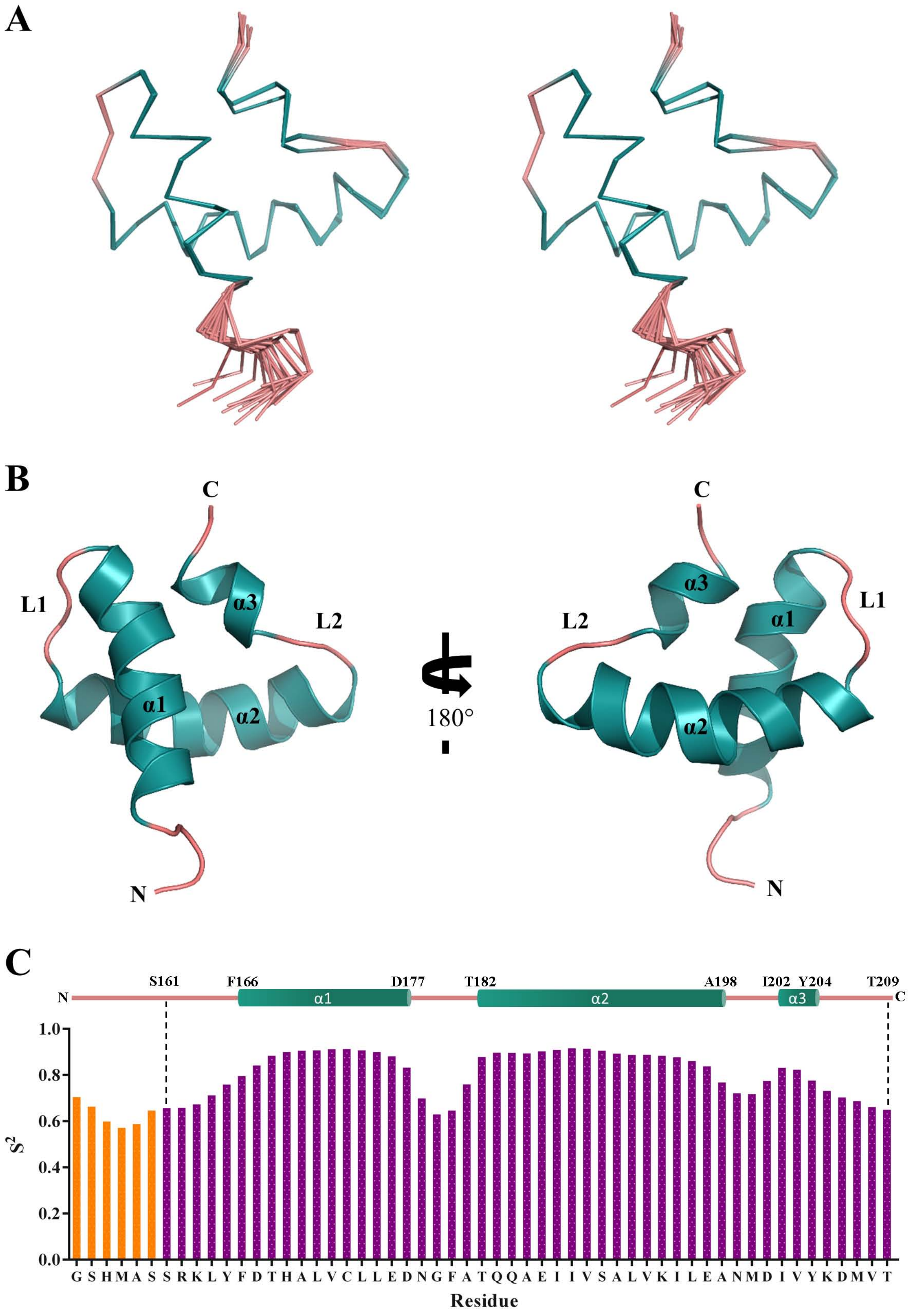
A
B
C
L1
L2
α1
α2
α3
N
180°
C
L2
L1
α3
α1
α2
N
C
S161
F166
D177
T182
A198
I202
Y204
T209
N
α1
α2
α3
C
1.0
0.8
0.6
0.4
0.2
0.0
S²
G S H M A S S R K L Y F D T H A L V C L L E D N G F A T Q Q A E I I V S A L V K I L E A N M D I V Y K D M V T
Residue

**Figure 15. Backbone conformation and dynamics of the MCUR1$_{161\text{-}209}$ solution NMR structure. A)** Backbone stereo view for the 20 lowest energy structures of MCUR1$_{161\text{-}209}$. The backbone atom root mean square deviation (RMSD) for the 20 lowest energy structure ensemble is 0.9 Å. **B)** Cartoon/ribbon view of the backbone structure of MCUR1$_{161\text{-}209}$. MCUR1$_{161\text{-}209}$ forms compact triple α-helix structure with two loops. Cyan and pink colors differentiate α-helix and loop secondary structures, respectively. **C)** Order parameter ($S^2$) distribution along the primary structure of MCUR1$_{161\text{-}209}$. $S^2$ was predicted from the chemical shift assignments using TALOS+. The C-terminal helix (i.e. α3) potentially exists in a more dynamic state compared to α1 and α2 which have systematically higher $S^2$ values.

## 3.7 The MCUR1$_{161\text{-}209}$ matrix region forms a large electronegative surface patch.

Next, I calculated the electrostatic surface potential of my MCUR1$_{161\text{-}209}$ structure using the adaptive Poisson Boltzmann solver (APBS) and partial charge assignment of each atom using the PDB2PQR server (Jurrus et al., 2018). The electrostatic surface potential of MCUR1$_{161\text{-}209}$ shows a large negatively charged surface patch on one side of the protein (Figure 16A). The prominent negatively charged residues contributing to this electronegative surface patch include E176 and D177 of α1, E197 of α2, D201 of L2 and the carboxyl terminus (Figure 16A). On the opposite face of the protein, a distinct electropositive patch is apparent (Figure 16B). This electropositive patch is primarily contributed to by the positively charged R162 and K163 residues near the amino terminus and K194 of α2. These regions may play a role in stabilizing the interactions between MCUR1 and other accessory proteins in the MCU complex via charge complementarity between the electropositive and electronegative patches (see below).

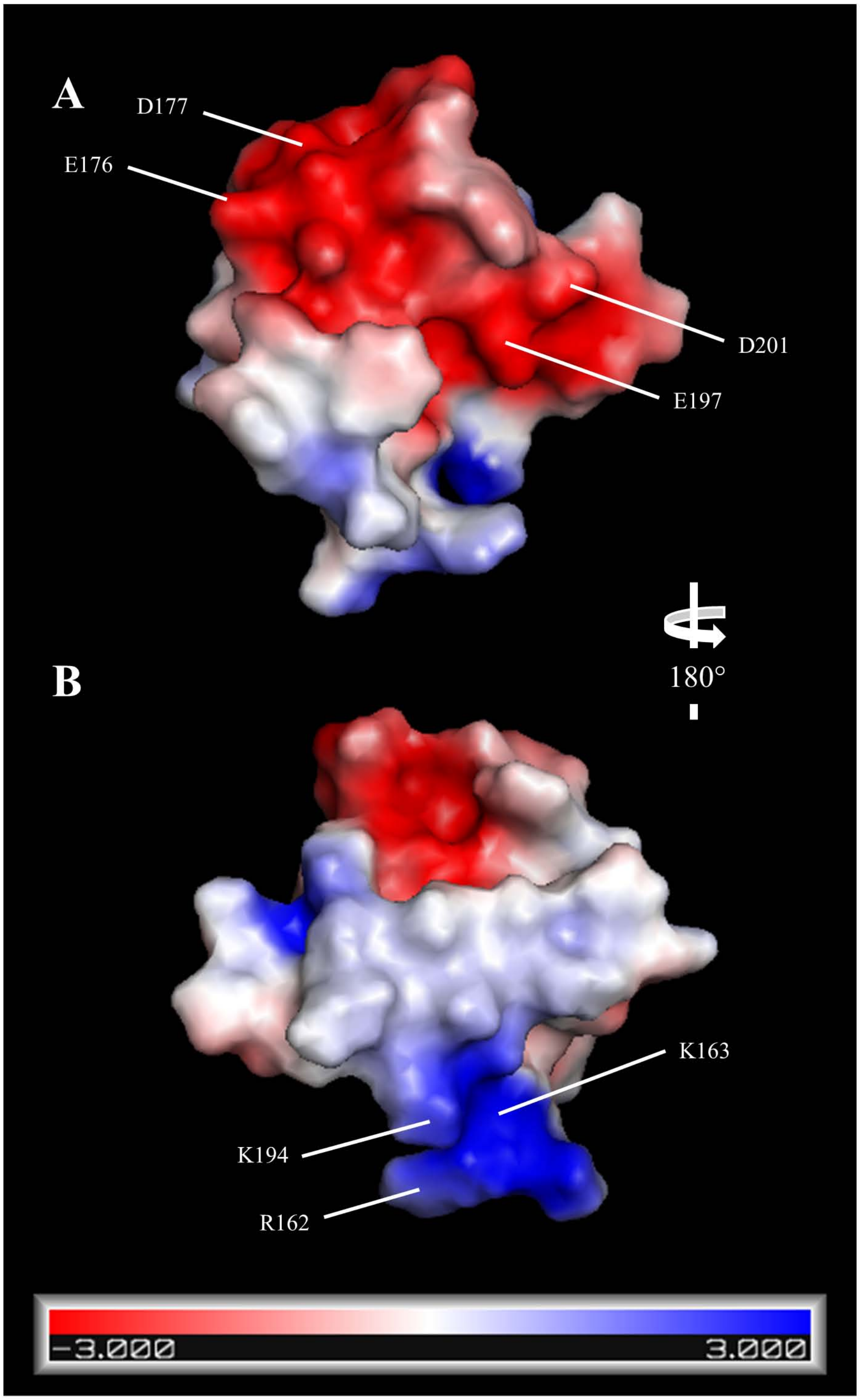

**Figure 16. Electrostatic surface potential of the MCUR1$_{161\text{-}209}$ construct.** Prominent charged residues contributing to the two predominant electropositive and electronegative patches are labelled. The electrostatic colour gradient applied ranges from -3 (red) to +3 (blue) kT/e.

## 3.8 The α1 and α3 helices of MCUR1$_{161\text{-}209}$ form the dimer interface.

Having solved the high-resolution structure for MCUR$_{161\text{-}209}$ construct and having revealed that this domain forms dimer in solution, I further aimed to elucidate the residues involved in forming the self-association interface. Given that MCUR1$_{161\text{-}209}$ contains a single Cys (i.e. C173) located in α1 of the globular structure, I used this unique feature as a tool to help map the location of the interface. Specifically, I used a PRE approach which nitroxide spin tagged the single cysteine residue [i.e. with MTSL] in an unlabeled MCUR1$_{161\text{-}209}$ sample. Subsequently, I mixed the nitroxide-tagged MCUR1$_{161\text{-}209}$ with uniformly $^{15}$N-labeled MCUR1$_{161\text{-}209}$ in an equimolar ratio (see Materials and Methods). Finally, I acquired $^{1}$H-$^{15}$N-HSQC spectra of the mixed sample in the absence and presence of 15 mM DTT. In the absence of the reducing agent, H($^{15}$N) in close proximity of the PRE tag showed crosspeaks with reduced intensities (Figure 17A). The addition of DTT then reduced the covalent bond between nitroxide spin tag and C173, and a subsequent $^{1}$H-$^{15}$N-HSQC acquisition provided the baseline H($^{15}$N) peak intensity reading. Thus, simple intensity ratios from these $^{1}$H-$^{15}$N-HSQC spectra helped establish the location of the interface, where the lowest intensity ratios suggest the closest H($^{15}$N) to the C173 probe location.

After acquiring the $^{1}$H-$^{15}$N-HSQC spectra in the presence and absence of the PRE-tagged protein, several H($^{15}$N) crosspeaks showed losses in peak intensity, consistent with the self-association of the protein construct. A plot of the intensity ratio versus residue number showed that many of the crosspeaks with the lowest intensity ratios clustered close together (Figure 17B). In particular, residues H169, A170, L171, V172, C173, L174, L175, and D177 located on α1 showed dramatic peak broadening [i.e. H($^{15}$N) crosspeak intensity ratios in the absence versus presence of DTT ($I_{PRE}/I_{DTT}$) $\leq 0.5$] (Figure 17B). Other residues that showed dramatic reduction in peak intensities included A198 and V203, present on α2 and α3, respectively.

Importantly, plotting the H($^{15}$N) $I_{PRE}/I_{DTT}$ ratios as a color gradient on the surface of the MCUR1$_{161\text{-}209}$ structure highlighted that many of the most broadened peaks cluster together in 3D space predominantly on $\alpha1$ and $\alpha3$ (Figure 17C). Interestingly, the identified interface appears to align with the electronegative surface patches of the MCUR1$_{161-209}$ construct (Figure 16A). Thus, my PRE data confirms that the MCUR1$_{161-209}$ protein construct self-associates under the NMR solution conditions, and the $\alpha1$ along with the $\alpha3$ helices form the interface which mediates this assembly.

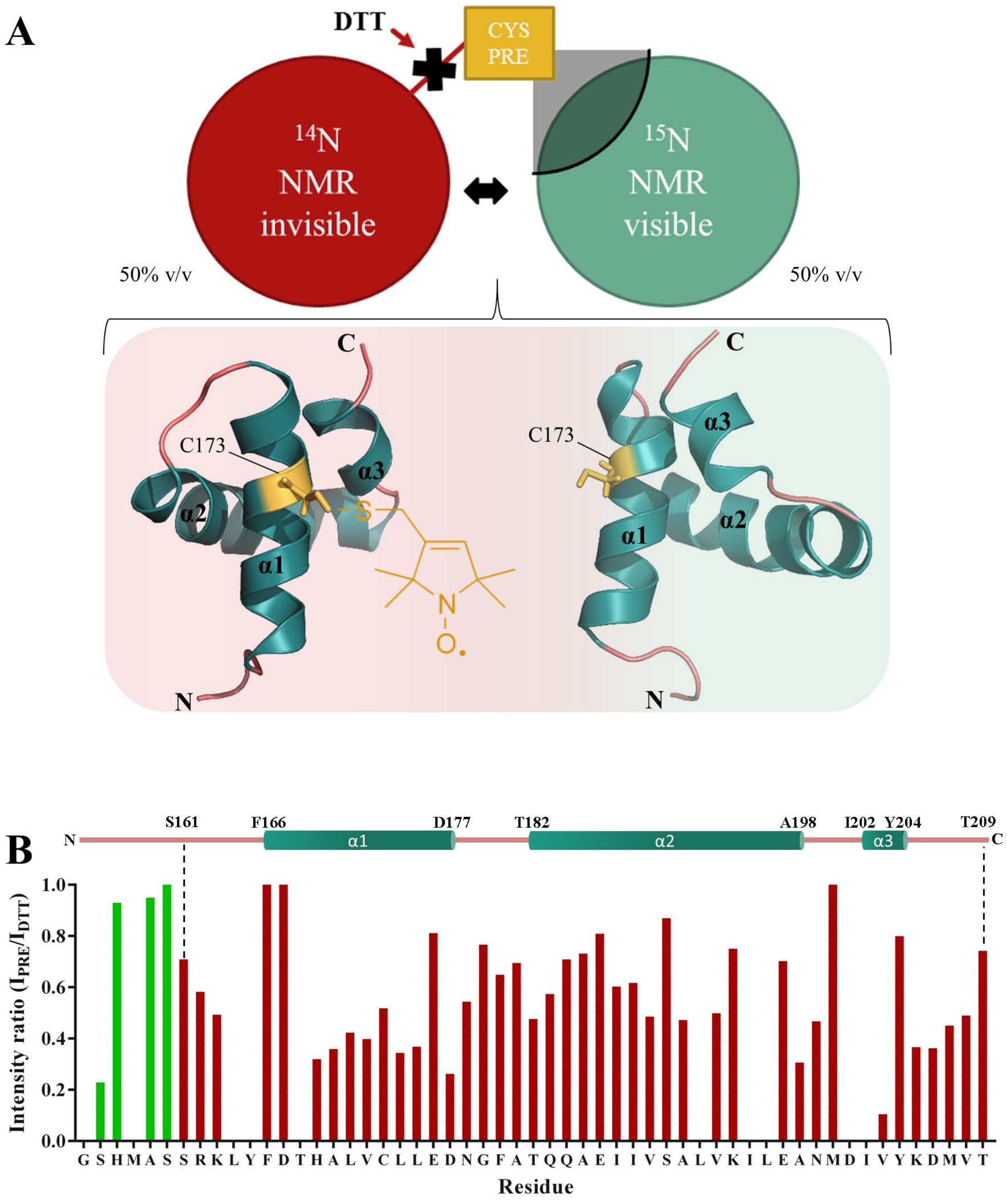
A
DTT
CYS PRE
$^{14}$N NMR invisible
$^{15}$N NMR visible
50% v/v
50% v/v
C
C173
α3
α2
α1
S
N
O
N
C
C173
α3
α1
α2
N
B
S161
F166
D177
T182
A198
I202
Y204
T209
N
α1
α2
α3
C
Intensity ratio ($I_{PRE}/I_{DTT}$)
1.0
0.8
0.6
0.4
0.2
0.0
G S H M A S S R K L Y F D T H A L V C L L E D N G F A T Q Q A E I I V S A L V K I L E A N M D I V Y K D M V T
Residue

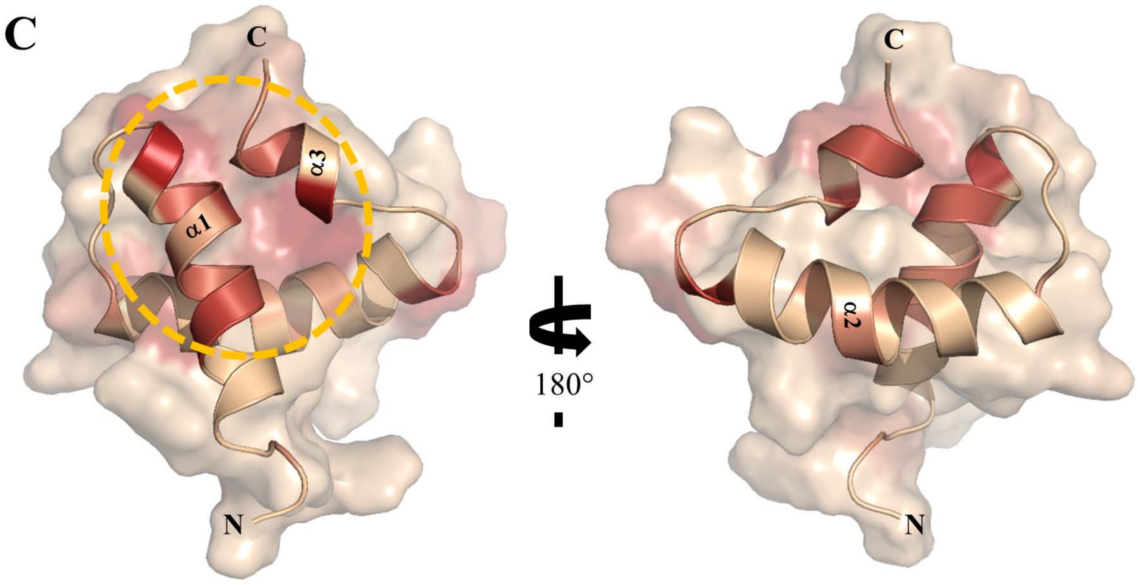

**Figure 17. PRE-NMR spectroscopy of the MCUR1$_{161\text{-}209}$. A)** Schematic representation of the PRE-NMR protocol used to identify the MCUR1$_{161\text{-}209}$ self-association interface. **B)** H($^{15}$N) amide crosspeak broadening calculated for each residue as a ratio of the intensity before and after the addition of DTT ($I_{PRE}/I_{DTT}$). A major cluster of residues from H169 to L175 corresponding to α1 of MCUR$_{161\text{-}209}$ show a > 50 % loss in intensity. V203 on α3 also displays a dramatic decrease in peak intensity. **C)** H($^{15}$N) amide crosspeak intensity ratios plotted as a color gradient on the surface (transparent) and backbone structure (ribbon) of MCUR1$_{161\text{-}209}$. The colour gradient is shown from red ruby/maroon (highest level of broadening) to wheat/beige (lowest level of broadening). Hotspot region of major broadening in three-dimensional space is highlighted by the yellow dashed circle.

## 3.9 The MCUR1$_{161\text{-}209}$ matrix region is structurally homologous to the bacterial acid chaperone HdeB.

Having solved the high resolution structure of the MCUR1$_{161\text{-}209}$ region and having established the location of the dimer interface, I next searched for structural homologs among the currently available high resolution structures deposited in the Research Collaboratory for Structural Bioinformatics (RCSB) protein databank. I used the DALI web server to search the database (Holm & Sander, 1995). My search revealed that the acid stress chaperone HdeB from *E. coli* as a close structural homolog to my MCUR1$_{161\text{-}209}$ construct (Figure 18A). Remarkably, the sequence similarity between the MCUR1$_{161\text{-}209}$ and HdeB is only 5 %, yet the backbone RMSD between the two proteins is 2.2 Å after aligning the 3 helices. The α1 and α2 of MCUR1$_{161\text{-}209}$ orient analogously with the two larger helices of HdeB. Additionally, although the α3 helix of MCUR1$_{161\text{-}209}$ does not superimpose well with the helical axis of the C-terminal helix of HdeB, α3 presents in very close proximity to this C-terminal helix (Figure 18A). The HdeB protein does contain some prominent distinctions. In particular, the HdeB contains an extra helix at the N-terminal end of the protein and a much longer linker region between the two large helices compared to L1 of MCUR1$_{161\text{-}209}$. Nevertheless, the overall structural similarity of HdeB to MCUR1$_{161\text{-}209}$ suggests some interesting physiological functions for MCUR1 which have not been previously explored or considered (see Discussion).

Excitingly, the acid stress chaperone HdeB also exists as a symmetrical homodimer (Figure 18B). Further, the crystal structure of HdeB shows that the helix which aligns with α1 in MCUR1$_{161\text{-}209}$ is central to the HdeB dimer interface, and the C-terminal helix of HdeB which aligns with MCUR1$_{161\text{-}209}$ α3 is also present in the interface (Figure 18B). Remarkably, based on my PRE data, α1 and α3 similarly forms the interface in MCUR1$_{161\text{-}209}$. In HdeB, the two subunits appear to interact with α1-like helices of HdeB oriented approximately perpendicular to each other. Overall, the structural homology between HdeB and MCUR1$_{161\text{-}209}$ strengthens the validity of the isolated structure and the relative location of the interface determined using the PRE approach.

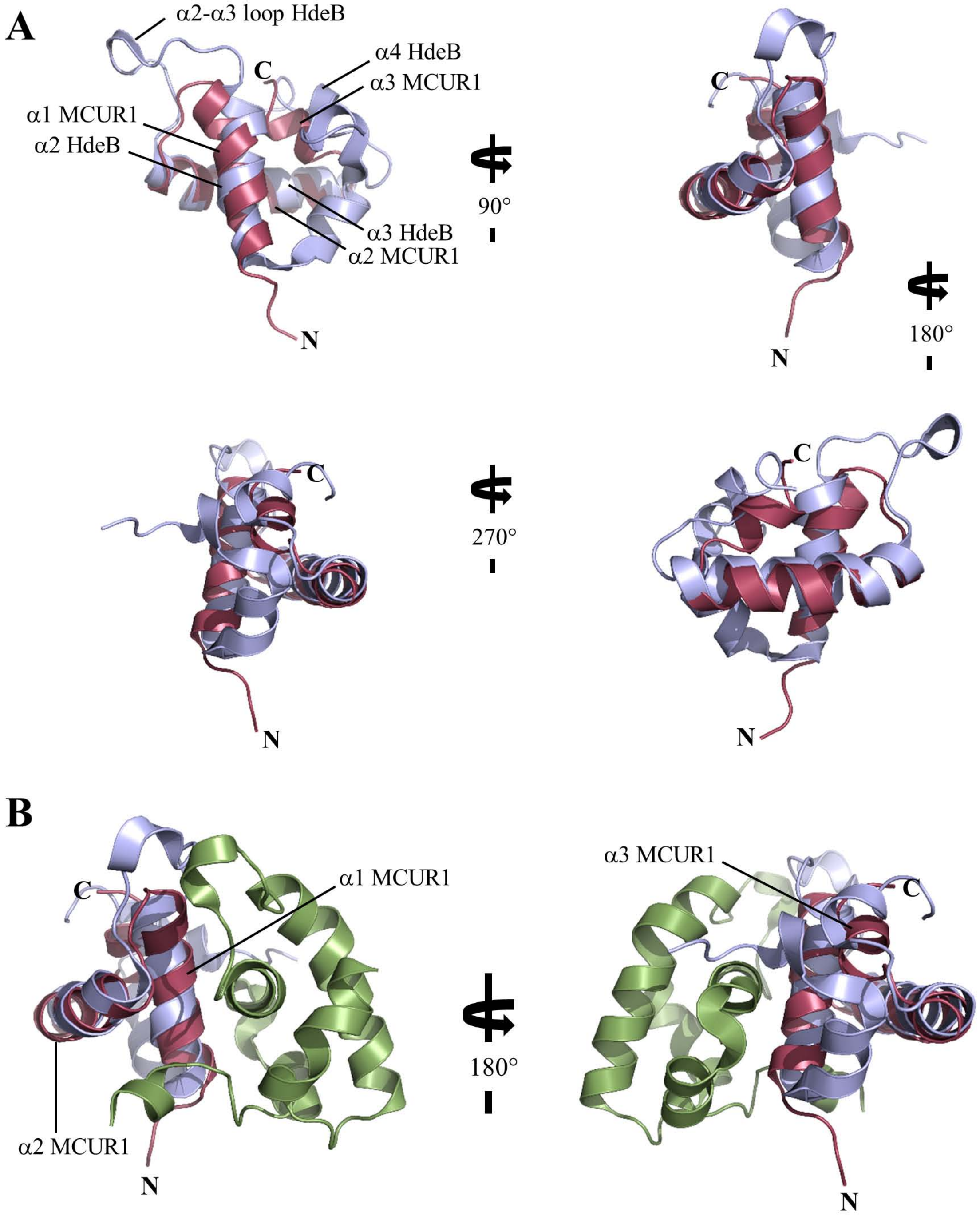

**Figure 18. Structural alignment of MCUR1$_{161\text{-}209}$ with HdeB.** HdeB was identified as a close structural homolog of MCUR1$_{161\text{-}209}$ using the online DALI server (PDB ID: 4XVV). **A)** Backbone structural alignment of the MCUR1$_{161\text{-}209}$ monomer (maroon) and HdeB monomer (blue). **B)** Backbone structural alignment of MCUR1$_{161\text{-}209}$ (maroon) with the HdeB dimer. The HdeB subunits are shown as blue and green. The backbone structural alignments shown are as outputted from DALI. All images are ribbon views of the backbone.

## 3.10 Point mutations in $\alpha1$ or $\alpha3$ perturbs MCUR1$_{161-209}$ and MCUR1$_{161-338}$ assembly.

Having defined the dimerization interface for the MCUR1$_{161-209}$ protein construct through PRE-NMR experiments and finding that this interface is remarkably homologous to the HdeB dimer interface, I next introduced point mutations in $\alpha1$ and $\alpha3$ to study their impact on self-association of the construct. I used PCR-mediated, site-directed mutagenesis to introduce the mutations. Two of the mutants were designed to target the residues identified on $\alpha1$, whereas one mutant targeted $\alpha3$ (Figure 19). More specifically the A170R/L174R double mutant was aimed to disrupt the adjacent hydrophobic interactions of $\alpha1$, whereas the aggressive C173P/L174P/L175P triple mutant was aimed at disrupting the $\alpha1$ helix formation entirely. The V203R/Y204R double mutant was introduced into $\alpha3$ to probe the role of this peripheral helix in self-association.

All three mutations in the MCUR1$_{161-209}$ construct led to dramatic reduction in protein yield as large amounts of aggregation and precipitation was observed. Additionally, the SEC elution profiles of each mutant changed in comparison to the wild-type MCUR1$_{161-209}$ profile. Specifically, the A170R/L174R mutation led to an earlier elution time (Figure 20A). Interestingly, the A170R/L174R mutant showed two overlapping major elution peaks; one with a similar elution volume as the aggressive C173P/L174P/L175P triple mutant peak and one with an elution volume similar to the wild-type (Figure 20A). Finally, the V203R/Y204R double mutation in $\alpha3$ also caused a shift in the major peak to an earlier elution time, similar to A170R/L174R.

To confirm that the shift to earlier elution times was not due to new charge interactions with the column resin introduced by the Arg mutations, I next assessed the elution profiles of the MCUR1$_{161-209}$ protein harboring A170S/L174S (i.e. in $\alpha1$) and V203S/Y204S (i.e. in $\alpha3$). Just as observed with the charge mutations, proteins with these neutral charge substitutions showed shifts to earlier elution volumes as well (Figure 20B). Additionally, these Ser mutants also displayed a highly reduced protein yield due to a tendency for protein aggregation and precipitation. Unfortunately, the tendency to aggregate for all MCUR1$_{161\text{-}209}$ mutant constructs meant that the protein yield was not high enough to quantify the oligomeric state of the mutants via SEC-MALS.

Finally, I introduced these mutations in the largest MCUR1$_{161\text{-}338}$ construct to examine the significance of the identified interface in the full matrix domain context. Intriguingly, these mutations also led to a drastic reduction in protein yield due to high levels of aggregation and precipitation, as observed for MCUR1$_{161\text{-}209}$ (Figure 20C). The A170R/L174R, V203R/Y204R and C173P/L174P/L175P mutant proteins all showed dramatic shifts to earlier elution times, as previously observed for the MCUR1$_{161\text{-}209}$ proteins. Unfortunately, quantification of MCUR1$_{161\text{-}338}$ mutant masses via SEC-MALS was not possible because the proteins eluted too close to the column void volume. Resin particles shedding off the column dominate the light scattering signal near the void volume, precluding accurate mass determinations. Collectively, my mutagenesis analysis showed that disrupting either $\alpha 1$ or $\alpha 3$ perturbs the elution volume of MCUR1$_{161\text{-}209}$. Remarkably, perturbations caused by mutations in these helices were also observed in the MCUR1$_{161\text{-}338}$ context, demonstrating the significance of the core MCUR1$_{161\text{-}209}$ structure elucidated to the assembly of the full structured matrix region of MCUR1 containing both coiled coils.

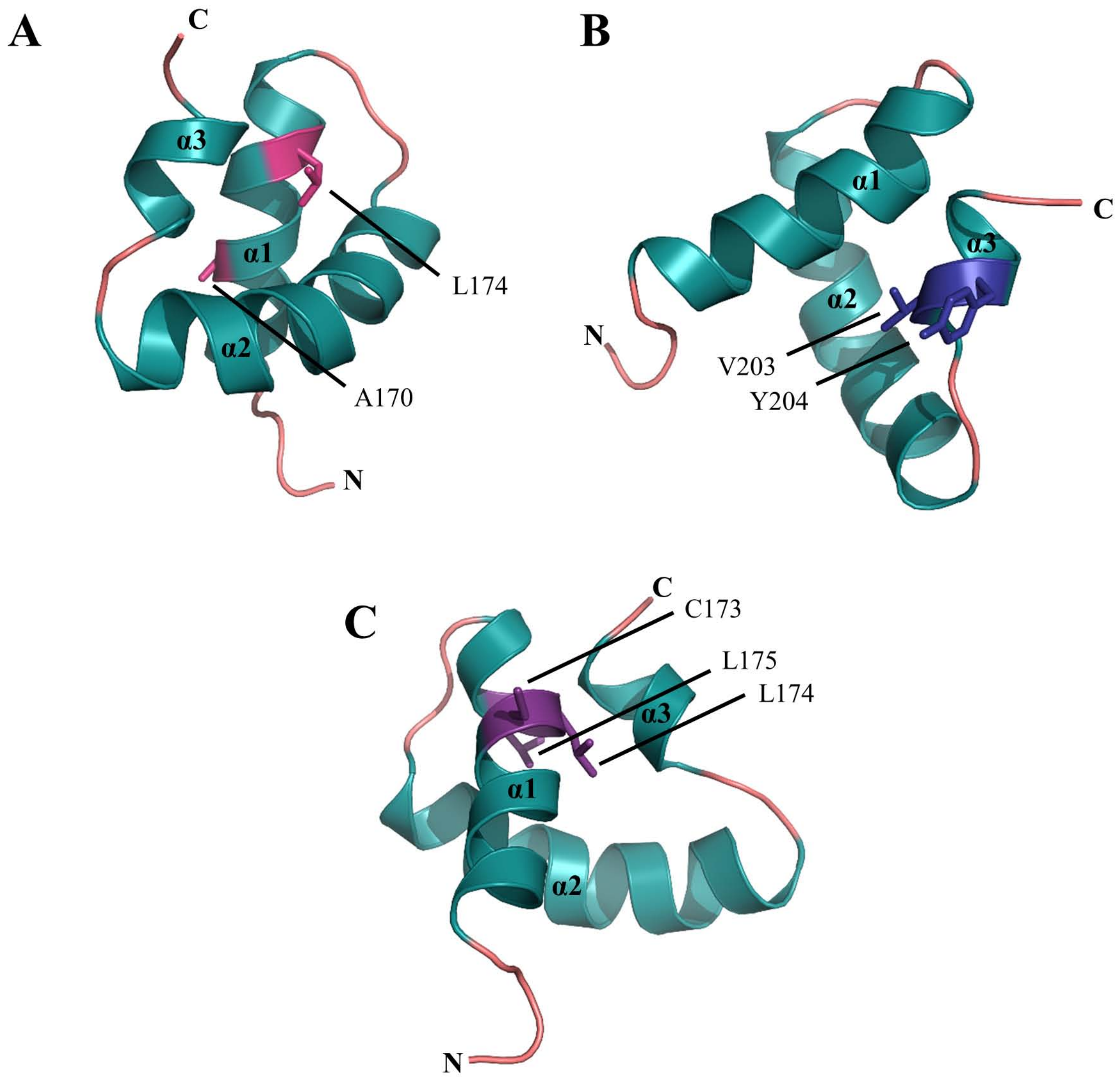

**Figure 19. Relative locations of the MCUR1$_{161\text{-}209}$ mutations designed to perturb quaternary structure. A)** The A170 and L174 residues (magenta stick representations) on $\alpha$1 of the MCUR1$_{161\text{-}209}$ construct. **B)** The V203 and Y204 residues (blue stick representations) on $\alpha$3 of the MCUR1$_{161\text{-}209}$ construct. **C)** The C173, L174, and L175 (purple stick representations) on the central region of $\alpha$1. Mutations in panel (*A)* and (*B*) were designed to perturb the self-association interface while mutations in (*C*) were engineered to disrupt $\alpha$1 helical folding.

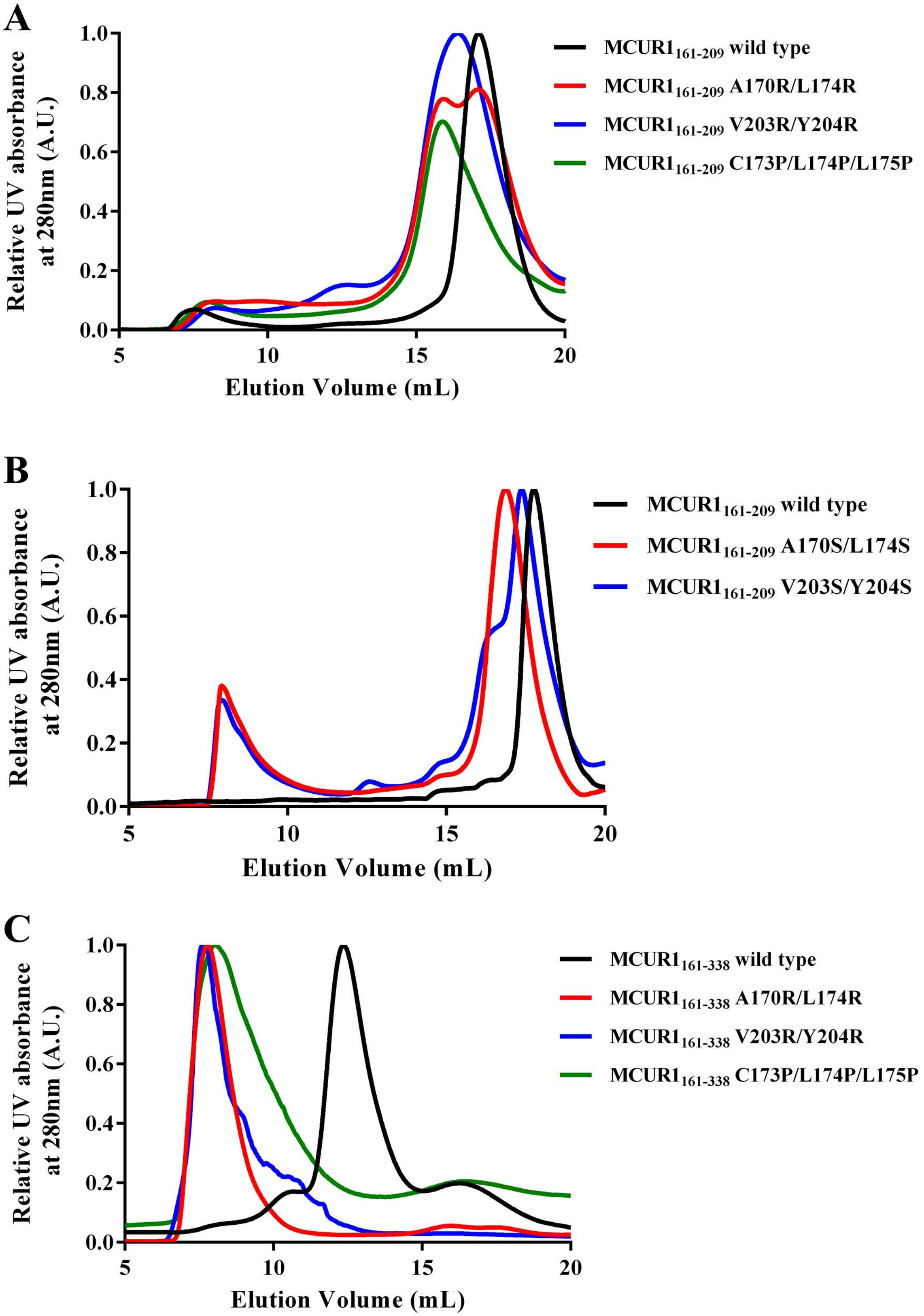
A
Relative UV absorbance at 280nm (A.U.)
1.0
0.8
0.6
0.4
0.2
0.0
5
10
15
20
Elution Volume (mL)
MCUR1$_{161-209}$ wild type
MCUR1$_{161-209}$ A170R/L174R
MCUR1$_{161-209}$ V203R/Y204R
MCUR1$_{161-209}$ C173P/L174P/L175P
B
Relative UV absorbance at 280nm (A.U.)
1.0
0.8
0.6
0.4
0.2
0.0
5
10
15
20
Elution Volume (mL)
MCUR1$_{161-209}$ wild type
MCUR1$_{161-209}$ A170S/L174S
MCUR1$_{161-209}$ V203S/Y204S
C
Relative UV absorbance at 280nm (A.U.)
1.0
0.8
0.6
0.4
0.2
0.0
5
10
15
20
Elution Volume (mL)
MCUR1$_{161-338}$ wild type
MCUR1$_{161-338}$ A170R/L174R
MCUR1$_{161-338}$ V203R/Y204R
MCUR1$_{161-338}$ C173P/L174P/L175P

**Figure 20. Size exclusion chromatography elution profiles of MCUR1$_{161\text{-}338}$ and MCUR1$_{161\text{-}209}$ wild-type and mutant protein constructs. A)** Overlay of wildtype (black), A170R/L174R (red), V203R/Y204R (blue) and C173P/L174P/L175P (green) MCUR1$_{161\text{-}209}$ elution chromatographs obtained by plotting the relative absorbance at 280 nm against the column elution volume. **B)** Overlay of wildtype (black), A170S/L174S (red) and V203S/Y204S (blue) elution chromatographs. **C)** Overlay of wildtype (black), A170R/L174R (red), V203R/Y204R (blue) and C173P/L174P/L175P (green) MCUR1$_{161\text{-}338}$ elution chromatographs. All mutations altered the elution profiles in both the MCUR1$_{161\text{-}209}$ and MCUR1$_{161\text{-}338}$ contexts, consistent with the important role in MCUR1 interface stability. Data were collected on a Superdex Increase 200 10/300 GL column using 1.5 µL injections of concentrated purified protein in 20 mM HEPES, 150 mM KCl, 1 mMDTT, and pH 7.5 (MCUR1$_{161\text{-}209}$) or pH 8.3 (MCUR1$_{161\text{-}338}$).

# Chapter 4

# 4 Discussion

## 4.1 Summary

The rapid uptake of $Ca^{2+}$ across the IMM not only modulates the cytosolic $Ca^{2+}$ transients which are integral to myriad signaling processes, but also leads to the increased production of ATP and can cause the activation of various cell death pathways (Gilabert & Parekh, 2000; Glancy & Balaban, 2012; Hoth et al., 1997; Lemasters et al., 1998; Nakagawa et al., 2005). The main driving force behind this influx of $Ca^{2+}$ into the mitochondrial matrix is the highly negative potential (~ -180 mV) established across the IMM which facilitates the movement of nearly 10,000 $Ca^{2+}$ ions per second through the MCU channel (Gunter & Pfeiffer, 1990). Additionally, MCU is a very selective ion channel with a high binding affinity for $Ca^{2+}$ (apparent equilibrium dissociation constant of $\leq 2$ nM), thus, preventing the unregulated uptake of other ions from the cytosol such as $Na^+$ and $K^+$ which could lead to a rapid loss of the negative potential across the IMM (Kirichok et al., 2004). The MCU channel also has a remarkable $Ca^{2+}$ carrying capacity with an experimentally determined midpoint of saturation occurring at ~20 mM cytosolic $[Ca^{2+}]$ (Kirichok et al., 2004).

MCUR1 was recently identified as a major positive regulator of MCU channel activity. The siRNA-mediated knockdown of MCUR1 in fibroblasts showed a dramatic reduction in MCU dependent mitochondrial $Ca^{2+}$ uptake (Mallilankaraman et al., 2012). MCUR1 has also been shown to interact directly with MCU and EMRE, another important regulator of the MCU complex (Mallilankaraman et al., 2012; Tomar et al., 2016). Furthermore, the knockdown of MCUR1 not only impacts the distribution of oligomeric MCU within the IMM, but also leads to a reduction in the absolute MCU heterooligomeric size (Tomar et al., 2016). Despite the demonstrated implications of MCUR1 in the regulation of the MCU complex formation and $Ca^{2+}$ uptake into the mitochondria, no high-resolution structural information is currently available. Consequently, my work focused on the structural and biophysical characterization of the highly conserved and structured matrix region of MCUR1 which includes residues 161-338 (Figure 21A), with the goal of elucidating new insights into the molecular mechanisms of MCUR1-mediated regulation of MCU.

I found the MCUR1 region encompassing residues 161-338 to be highly α-helical, consistent with the presence of the two, primary structure-predicted, coiled coil domains. Remarkably, I found that the thermal stability was reduced for MCUR1 matrix domain protein constructs containing the coiled coils compared to proteins with these domains deleted; however, despite the thermal destabilization, these coiled coils favoured homotrimer formation over lower order quaternary structures. More specifically, I found that constructs lacking the coiled coil domains existed primarily as homodimers. Furthermore, retaining both coiled coils within the matrix domain (i.e. my $\text{MCUR1}_{161\text{-}338}$ construct) was shown to confer a conformational sensitivity to $Ca^{2+}$. In particular, I found that increasing $[Ca^{2+}]$ enhanced the surface exposed hydrophobicity of the MCUR matrix domain construct encompassing residues 161-338.

Excitingly, I was able to elucidate the first high-resolution structure of any region of human MCUR1 using solution NMR spectroscopy. The compact, triple helix structure of $\text{MCUR1}_{161\text{-}209}$ contains distinct electronegative and electropositive regions formed by the contribution of residues found far apart in sequence space (i.e. > 5 residues apart). Furthermore, I was able to identify the α1 and α3 helices as the major contributors to the dimer formation interface for the construct. Mutations targeting the identified residues of interaction were shown to disrupt the normal oligomerization profile of the $\text{MCUR1}_{161\text{-}209}$ construct. Remarkably, despite the $\text{MCUR1}_{161\text{-}209}$ region being a relatively small portion of the MCUR1 matrix domain, I found the same mutations introduced into the larger $\text{MCUR1}_{161\text{-}338}$ construct containing both coiled coils also dramatically impacted the oligomerization profile of this structured MCUR1 matrix region. Collectively, my high-resolution structural data identify the α1 and α3 interface of the $\text{MCUR1}_{161\text{-}209}$ region as a crucial homomeric protein interaction location with demonstrated consequences on the assembly of the full structured MCUR1 matrix region. This mode of assembly has possible implications for the higher order heteromeric complex formation and thus, the function of MCU.

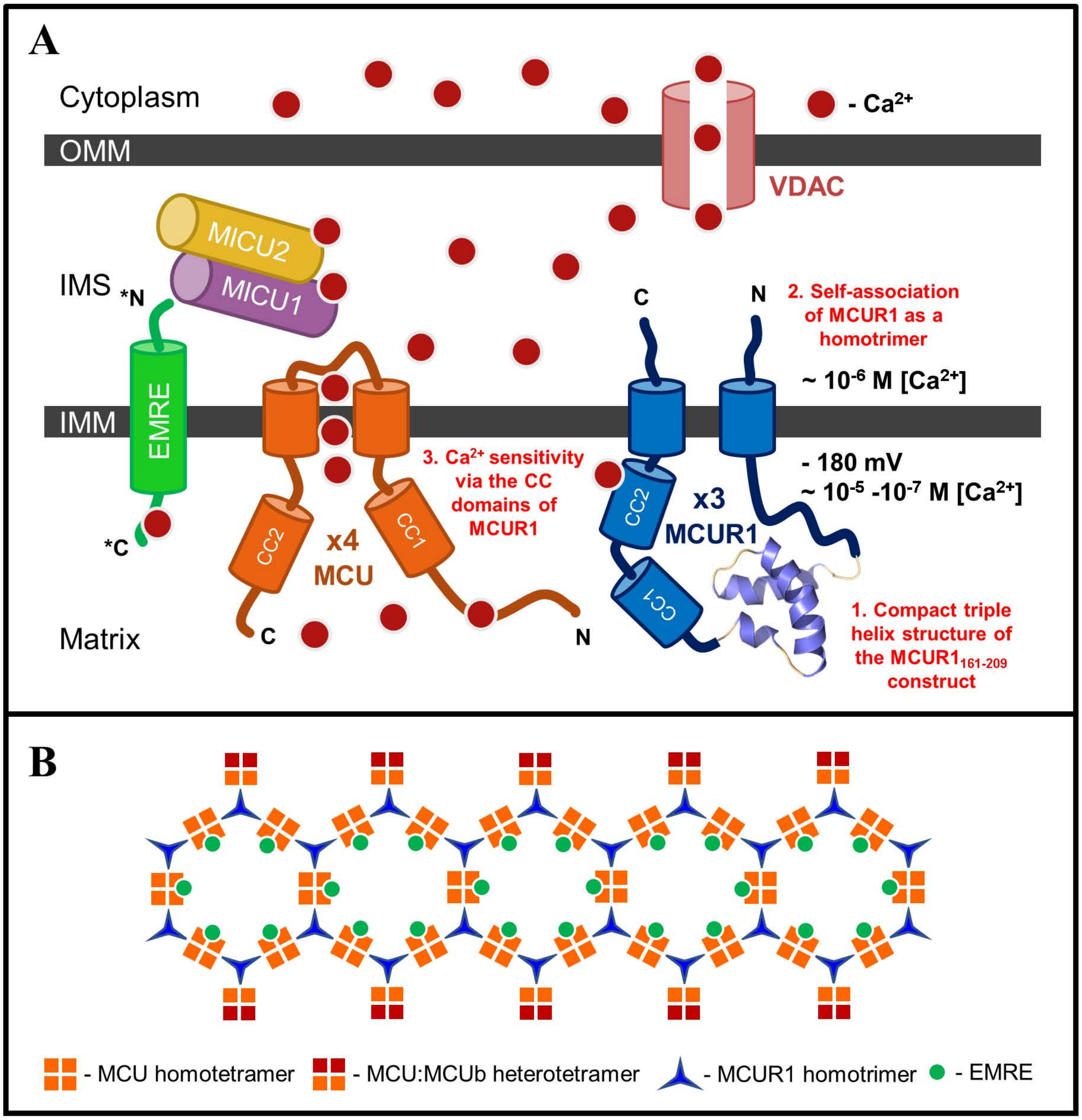

**Figure 21. Hypothetical models of MCUR1 and MCU complex assembly and regulation derived from the thesis data. A)** The elucidated high resolution structure of the conserved matrix facing region of MCUR1 (i.e. residue range 161-209) is shown as a ribbon view (1). The structured and evolutionarily conserved region of MCUR1 (i.e. residue range 161-338) with the coiled coil domains promotes trimer assembly (2). The coiled coil domains confer a structural sensitivity to Ca$^{2+}$ ions (3). **B)** A hypothesized model for MCUR1-mediated clustering of MCU. Each MCUR1 homotrimer is predicted to interact with three MCU dimers via the coiled coil domains of MCUR1 and the N-terminal domain of MCU (Tomar et al., 2016). The presence of EMRE is essential for Ca$^{2+}$ uptake via MCU channel, but the exact stoichiometry of interaction remains to be determined (Sancak et al., 2013). Lastly, MCUb, a dominant negative structural homolog of MCU, does not directly interact with MCUR1 and can thereby terminate clustering as well (Raffaello et al., 2013; Tomar et al., 2016).

## 4.2 The role of putative coiled coil domains in MCUR1 scaffolding function.

Part of the reason MCUR1 is believed to act as a scaffolding factor stems from its ability to interact with multiple proteins in the heteromeric MCU complex assembly. Coimmunoprecipitation studies have identified MCU and EMRE as proteins that interact with MCUR1, whereas MICU1 and LETM1 did not show an interaction with MCUR1 (Tomar et al., 2016). Furthermore, a biomolecular fluorescence complementation assay, which analyzes the topology based interaction of two proteins of interest by tagging parts of a fluorescent tag onto the C- or N-terminal of each protein, showed that the interaction of MCUR1 with EMRE occurs at the IMS while the interaction of MCU and MCUR1 is likely mediated by the matrix regions of both proteins (Tomar et al., 2016). Both MCU and MCUR1 contain two coiled coil domains facing the mitochondrial matrix (Figure 21A). Typically, coiled coil domains are composed of a heptad repeat sequence and have been shown to play numerous structural, regulatory and functional roles in eukaryotes, including protein-protein interactions (Rose & Meier, 2004). One important example of such an interaction can be seen between the coiled coil domains of STIM1 and Orai1 proteins which leads to the activation of $Ca^{2+}$-release activated channels (CRAC) channels (Stathopulos et al., 2013). Therefore, it is likely that the interaction of MCU and MCUR1 is regulated by the intermolecular coiled coil interactions between these proteins. Indeed, coimmunoprecipitation analysis conducted with truncation mutants of MCU and MCUR1 systematically eliminating the coiled coils showed that the N-terminal coiled coil domain of MCU and the putative coiled coil region of MCUR1 (i.e. CC1 and CC2) are essential for this heteromeric protein-protein interaction (Tomar et al., 2016).

Additionally, MCUR1 has been proposed to function as a scaffolding factor because of an ability to stabilize the MCU heteromeric complex. It has been shown that co-transfection of MCU and MCUR1 in HEK293T cells leads to larger heteromeric oligomers integrating MCU, as assessed via blue native PAGE and FPLC analysis (Tomar et al., 2016). The same study also showed that the knockout of MCUR1 in endothelial cells led to a significant disruption of the MCU heteromeric complex formation, consistent with a stabilizing role for MCUR1. Furthermore, the reduction in mitochondrial $Ca^{2+}$ uptake observed after MCUR1 knockdown concomitant with the disruption of MCU heteromeric complex formation reinforces the vital importance of MCUR1-mediated protein scaffolding in mitochondrial $Ca^{2+}$ uptake (Tomar et al., 2016).

According to my SEC-MALS data, MCUR1 matrix domains containing both coiled coils are homotrimeric, whereas $MCUR1_{161-209}$ forms a more stable dimer under similar solution conditions. This innate and high propensity for homo-oligomerization could be essential for multiple simultaneous MCUR1 interactions with MCU subunits, given that the MCU channel pore is likely made up of tetrameric MCU (see discussion section 4.5). Further, the oligomeric nature of the MCUR1 matrix domain may play a role in bridging interactions between multiple MCU subunits and other regulatory proteins identified in the MCU hetero-oligomeric complex, such as EMRE. Regardless, the coiled coils of MCUR1 clearly play a role in the stabilization of a higher order homomeric quaternary structure of MCUR1 as my SEC-MALS shows a favoured trimeric stoichiometry for $MCUR1_{161-338}$ (i.e. containing both coiled coils) compared to dimeric stoichiometry for $MCUR1_{161-209}$ (i.e. in the absence of the coiled coils).

Another potential function of MCUR1 oligomerization could be interactions and regulation of the proteins making up the mPTP. The molecular identity of mPTP remains an important question in the field with numerous proteins such as spastic paraplegia 7 (SPG7), cyclophilin D (CypD), voltage dependent anion channel (VDAC), adenine nucleotide translocator (ANT) and ATP-synthase, to name a few, having been pinpointed as contributors to the assembly and regulation of this pore (Biasutto et al., 2016; Leung & Halestrap, 2008; Zoratti & Szabo, 1995). Recently, knockdown of MCUR1 has been shown to confer an increased resistance to mitochondrial $Ca^{2+}$ overload-induced cell death in mammalian cells via the opening of mPTP (Chaudhuri et al., 2016). Therefore, MCUR1 may extend its scaffolding role by bridging MCU and mPTP complexes. In particular, CypD, a mitochondrial matrix chaperone that is also a key modulator of mPTP opening in mammalian cells (Baines et al., 2005; Basso et al., 2005), can potentially assist in the bridging of the these two complexes via interaction with the matrix region of MCUR1. Functionally, fixing MCU in close physical proximity to mPTP may expedite the signaling to mPTP opening under conditions of $Ca^{2+}$-overload.

The results from my ANS fluorescence experiments showed that MCUR1 exhibits a sensitivity to $Ca^{2+}$, much like many other proteins of the MCU complex including MICU1, MICU2, EMRE, and MCU itself (see introduction section 1.3 - 1.5). This $Ca^{2+}$ sensitivity has been proposed to finely regulate the function of MCU and $Ca^{2+}$ uptake into the mitochondrial matrix. In my studies, I found that the presence of the CC2 domain of MCUR1 provided the maximal sensitivity to $Ca^{2+}$. In fact, I carried out preliminary experiments aimed at identifying residues on the CC2 domain as potential $Ca^{2+}$ binding site(s). While charge neutralization mutations carried out on candidate acidic residues (i.e. D315, E318, and E321) did not show a statistically significant reduction in $Ca^{2+}$ sensitivity as determined by ANS binding, these mutants did show a trend to lower $Ca^{2+}$-mediated sensitivity. Further studies are required to ascertain the exact $Ca^{2+}$ binding site(s) and the functional significance of these divalent cation interactions. Additionally, $Ca^{2+}$-sensitive thermal stability was observed when both CC1-CC2 and CC1 alone were present. Thus, we deduce that both coiled coils are important for the $Ca^{2+}$ sensitive response.  Although, my thermal melt and ANS data indicates a conformational change in response to the divalent cations in the presence of both coiled coil domains, the oligomeric state observed via SEC-MALS is not impacted by the presence of $Ca^{2+}$ for the $MCUR1_{161-338}$ protein construct. This lack of change in quaternary structure suggests that the role of the coiled coils in the oligomerization of MCUR1 is not affected by $Ca^{2+}$; rather, $Ca^{2+}$ must be causing a conformational change elsewhere in the domain which is, nevertheless, still dependent on the coiled coils.

## 4.3 $MCUR1_{161-209}$ is structurally homologous to acid stress chaperone HdeB

According to the bioinformatics analysis of MCUR1, the region from residue 161 to 338 is highly α-helical and conserved across many higher order species. Conversely, the residual matrix facing region of MCUR1, starting at the end of first transmembrane domain (i.e. residue 86) and leading up to residue 160, is predicted to be unstructured and is not well conserved. Furthermore, my SEC-MALS data showed that the region comprising of residues 161 to 209 (i.e. $MCUR1_{161-209}$) is able to self-associate as a homodimer even in the absence of the putative coiled coil domains. Additionally, mutations incorporated into the characterized dimer interface of MCUR1$_{161-209}$ result in the assembly perturbation of the structured matrix region containing the coiled coils (i.e. MCUR1$_{161-338}$). Thus, the high-resolution structure obtained for MCUR1$_{161-209}$ provides valuable insights on a region that plays a key role in the oligomerization of MCUR1 mediated by the matrix-oriented region of the protein. I found that this ~6 kDa MCUR1$_{161-209}$ protein, sandwiched between the putative intrinsically disordered region and the coiled coils of MCUR1, folds into a compact, three helix conformation. My assessment using DALI revealed that the elucidated MCUR1$_{161-209}$ structure is homologous to the acid stress chaperone HdeB found in *E. coli*. Strikingly, the structural similarity between MCUR1$_{161-209}$ and HdeB does not stem from any sequence similarity, which is a meagre 5 %. The discovery of this structure in both prokaryotes and eukaryotes suggests that this fold may play a fundamental role in signaling and physiology of all cell types.

HdeB, along with its known structural homolog HdeA, provides the gram-negative *E. coli* with the ability to survive the extremely acidic environment of the human stomach (Hong et al., 2012). HdeA and HdeB act in concert by binding and reducing the exposed hydrophobic regions of the unfolded substrate/client proteins in response to the low pH environment of the stomach, thus preventing aberrant acid-induced unfolding and aggregation (Ding et al., 2015). HdeA has also been shown to assist in the ATP-independent refolding of these proteins via a ‘slow release mechanism’ upon neutralization of the acidic environment (Tapley et al., 2010). Substrate bound HdeA undergoes a much slower return to its inactive dimeric state in response to neutralization, thereby allowing the slow release and minimizing the generation of aggregation-sensitive folding intermediates for these substrates (Tapley et al., 2010). Interestingly, the two proteins function in different pH ranges, with HdeA showing optimal activity at pH ~2-3 and HdeB functioning more efficiently at pH ~4-5. Thus, the pair concertedly provide chaperonal activity over a wider environmental range (Dahl et al., 2015; Kern et al., 2007).

It is tempting to speculate that MCUR1$_{161-209}$ oligomerization and function may also exhibit a physiologically relevant pH sensitivity, as the mitochondrial matrix sees a large influx of $H^+$ ions from the IMS during ATP synthesis. Thus, $MCUR1_{161-209}$ may be exposed to pH fluctuations in the matrix which could affect its folding, self-association and function. In particular, the imidazole functional group found on the side chain of His is highly susceptible to protonation within the physiological pH range due to its pKa of ~6.5. At pH above 7.0, His exists primarily in a non-protonated hydrophobic form, whereas the protonated and charged hydrophilic form dominates below pH 6.0 (Rotzschke et al., 2002). The presence of a highly conserved His residue (i.e. H169) at the beginning of the important $\alpha 1$ of $MCUR1_{161-209}$ construct provides a putative mechanistic site for this proposed pH sensitivity (Figure 2).

Unlike HdeA that undergoes a partial unfolding event at pH ~2-3 in order to expose hydrophobic residues and function as a chaperone, HdeB maintains a dimeric state and utilizes the dynamic nature of its loop region between $\alpha 2$ and $\alpha 3$ (i.e. analogous to L1 between $\alpha 1$ and $\alpha 2$ of $MCUR1_{161-209}$) to achieve interactions with its client proteins (Ding et al., 2015). Interestingly, analytical centrifugation has shown that HdeB does not undergo monomerization but rather displays structural rearrangements in response to pH changes (Dahl et al., 2015). Analytical ultracentrifugation data at pH ~4-5 showed that HdeB occupies a larger volume than would be expected for a dimer, indicating the potential for higher order oligomerization. This arrangement of HdeB into a state larger than dimer is in-line with the compatibility of $MCUR1_{161-209}$ assembly into a molecular weight species greater than dimer in the presence of the coiled coil domains.

The binding interface contributed to by $\alpha 2$ of HdeB (i.e. analogous to the $\alpha 1$ of $MCUR1_{161-209}$) appears to be rigid at neutral pH; however, rapid movement of the long $\alpha 2$-$\alpha 3$ loop region occurs at pH ~4-5 (Ding et al., 2015). This dynamic nature of the $\alpha 2$-$\alpha 3$ loop region along with the presence of multiple hydrophobic residues on this linker is believed to confer HdeB with the conformational plasticity required to interact with multiple substrate/client proteins and function as a chaperone (Ding et al., 2015). Although $MCUR1_{161-209}$ contains a similar organization for the dimer interface, the L1 region of $MCUR1_{161-209}$ is not as dynamic as suggested by the $S^2$ values derived from my chemical shift assignments (Figure 15C). This marked difference could be due to the shorter nature of the L1 region of $MCUR1_{161-209}$ compared to the analogous loop in

HdeB. As a scaffold protein, MCUR1 must interact with multiple specific proteins simultaneously and thus, may not require a dynamically changing interface which allows chaperones like HdeB to bind multiple different proteins at the same interface. Furthermore, MCUR1 contains two coiled coils and a large unstructured domain that may also mediate protein-protein interactions.

## 4.4 The impact of targeted mutations on the self-association interface of MCUR1.

My work suggests that full-length human MCUR1 likely assembles into a higher order homo-oligomeric state, supporting its proposed role as a scaffolding factor in the higher order MCU heteromeric complex formation. My structural characterization of $MCUR1_{161-209}$ via solution NMR spectroscopy and my data showing that this construct readily self-associates, compelled me to study the potential homomeric binding interface of MCUR1. My PRE-NMR data acquired to identify the residues involved in this interface formation, highlighted $\alpha1$ as the chief contributor along with parts of $\alpha3$ (see results section 3.8). Based on my PRE data, mutations were designed to target the $MCUR1_{161-209}$ self-association interface. Strikingly, the SEC elution profile analysis for all mutant constructs targeting either the $\alpha2$ or $\alpha3$ interface components dramatically perturbated the higher order assembly of $MCUR1_{161-209}$. Additionally, these mutations incorporated into the $MCUR1_{161-338}$ resulted in similar perturbations, indicating that despite the diminutive size of the $MCUR1_{161-209}$ region, the interface discovered by solution NMR spectroscopy plays a prominent mechanistic role in the assembly of the entire structured MCUR1 matrix region. It is important to note that I observed a drastic reduction in protein yield of all mutants (i.e. in both the $MCUR1_{161-209}$ and $MCUR1_{161-338}$ contexts) due to high levels of aggregation and precipitation, precluding accurate determination of the oligomerization states via SEC-MALS.

Nevertheless, the existence of a higher order oligomer state for these mutants could potentially be explained by the weakening of the $\alpha1$-$\alpha3$ interface, permitting the insertion of additional subunits to form a higher order oligomer. This speculation is supported by my thermal melt data which shows the highest stability for the $MCUR1_{161-209}$ construct which exists as a homodimer and less stable MCUR1$_{161-338}$ construct which exist as a homotrimer. Thus, it is possible that the coiled coil domains may similarly pull apart the MCUR1$_{161-209}$ binding interface and promote the insertion of a third subunit. Collectively, the ability of the same mutations to drastically perturb the assembly of MCUR$_{161-209}$ and MCUR1$_{161-338}$ reaffirms the significance of the identified MCUR1$_{161-209}$ structure and self-association interface in the potential regulation of full length MCUR1 oligomerization.

## 4.5 Oligomeric state of the MCU channel pore.

Although the propensity of MCU to oligomerize and form the Ca$^{2+}$ selective pore has been well established, the precise MCU oligomer state required for function was the subject of debate (De Stefani et al., 2011; Kirichok et al., 2004; Oxenoid et al., 2016). Great strides were made in this regard recently with the cryo-EM driven full-length structural elucidation of four fungal and two metazoan (i.e. zebrafish and mosquito) MCU channels (Baradaran et al., 2018; Fan et al., 2018; Nguyen et al., 2018; Yoo et al., 2018). All six structures show a similar architecture with the functional MCU existing as a homotetramer. It is important to note that fungal MCU can form a functional channel in the absence of any regulatory proteins (i.e. EMRE or MCUR1). These recent elucidations are in contrast to the previously proposed pentameric assembly of *C. elegans* MCU structure which did not contain the N-terminal domain (Oxenoid et al., 2016). In humans, a 'DIME' motif (i.e. Asp-Ile-Met-Glu) is known to play a role in Ca$^{2+}$ selectivity through the pore (Bick et al., 2012). Based on the cryo-EM structures of other species, the motif has been extended to 'WDXXEPVTY', with 'XX' being any hydrophobic residues and 'DXXE' representing the DIME motif in humans. The tryptophan residue in this motif tightly interacts with the proline residue, helping to properly orient the glutamic acid that is critical in the selectivity filter configuration (Fan et al., 2018; Nguyen et al., 2018; Yoo et al., 2018).

The cryo-EM structure of the *Neurospora crassa* shows the formation of four dimeric coiled coils within the tetramer (Yoo et al., 2018). The N-terminal domain along with the coiled coil 1 forms a large interface of interaction between subunits (Yoo et al., 2018). Much like the other MCU structures, the *N. crassa* structure shows a 4-fold symmetry through the assembled TM domains, while the matrix-oriented N-terminal domains form a dimer of dimers (Yoo et al., 2018). The cryo-EM structures obtained for *Metarhizium acridum* and *Fusarium graminearum*, along with the crystal structure for *M. acridum*, not only show a similar N-terminal domain dimer of dimer architecture, but also reconstitute basic MCU channel activity when expressed in *E. coli* (Fan et al., 2018). In all the full-length structures, the TM1 of each subunit interacts with the TM2 of the adjacent subunit, TM2 lines the pore of the channel and the WDXXEPVTY motif forms part of the TM2 helix closest to the IMS (Fan et al., 2018).

Interestingly, the dimer of dimer organization of the N-terminal domain leads to the generation of two distinct interfaces of interaction (Fan et al., 2018). This can potentially be important for understanding the interaction of MCU with multiple regulatory factors such as MCUR1 and EMRE. It has previously been proposed that EMRE interacts with MCU via the TM1 domain (Vais et al., 2016), whereas coimmunoprecipitation analysis suggests that the N-terminal domain of MCU interacts with the structured matrix region of MCUR1 containing the putative coiled coil domains (i.e. 166-305) (Tomar et al., 2016). Based on the scaffolding role of MCUR1 (see discussion section 4.2), I speculate that MCUR1 interacts with MCU via the MCU N-terminal domain, and this interaction brings two or more dimers of MCU in close proximity (Figure 21B). Once in close proximity, I predict EMRE functions to regulate the channel formation by stabilizing the tetramerization of MCU via interactions with the MCU TM1 domain. The potential clustering of MCU tetrameric channels by the interaction with MCUR1 would allow for the efficient mitochondrial $Ca^{2+}$ uptake observed near $Ca^{2+}$ channels found on the plasma membrane and ER (see introduction section 1.2.1). This proposed clustering function of MCUR1 is analogous to the STIM-mediated crosslinking of Orai1 channels which drive robust $Ca^{2+}$ signal generation in the cytosol (Zhou et al., 2018). Recent work has shown that oxidative stress induced S-glutathionylation of the C97 residue on MCU can lead to a conformational change in the N-terminal domain of MCU that, in turn, promotes clustering of the MCU channel and enhances $Ca^{2+}$ uptake (Dong et al., 2017). The conformational change in the N-terminal domain of MCU may promote the interaction with positive regulators of the MCU complex such as MCUR1 and EMRE.

The cryo-EM structure of metazoan zebrafish MCU also showed a tetrameric organization, but the N-terminal domains assembled as an asymmetric tetramer as opposed to the dimer of dimers observed in fungal MCU structures (Baradaran et al., 2018). However, the low-resolution structure of metazoan mosquito MCU did show the N-terminal domain dimer of dimers assembly, much like that of the fungal structures (Fan et al., 2018). Given that fungal MCU does not require MCUR1, EMRE, or MICU1/MICU2 to reconstitute channel activity, the elucidation of the human MCU structure and the interactions with these crucial regulators represents a major knowledge gap in the field. My structural work elucidating a portion of the MCUR1 matrix domain has begun to unravel some of the molecular features underlying MCUR1 assembly and thus, MCU regulation.

## 4.6 Future directions and limitations

The relevance of the high-resolution $MCUR1_{161-209}$ structure and self-association interface as a vital structural feature in regulating MCU function needs to be corroborated by functional analyses using full-length human MCUR1 expressed in live cells. The perturbation of the oligomeric profile observed for the mutants targeting the self-association interface should potentially cause a significant change in $Ca^{2+}$ uptake characteristics mediated by the human MCU channel.

Additionally, numerous post-translational modifications have been identified in eukaryotic cells that critically modulate the cell signaling, structural, and biophysical properties of proteins (Hess & Stamler, 2012). In particular, Cys residues are highly susceptible to these modifications, undergoing S-glutathionylation, S-nitrosylation, disulfide formation, to name a few (Go et al., 2015). As mentioned above, the highly conserved C97 on the MCU N-terminal domain has recently been shown to undergo S-glutathionylation in response to oxidative stress, leading to an increase in oligomerization propensity and $Ca^{2+}$ uptake (Dong et al., 2017). It is interesting to note that $MCUR1_{161-209}$ also contains a highly conserved cysteine residue (i.e. C173) on the important $\alpha1$ which was implicated in forming the self-association interface in my studies. Thus, post translational modifications on this residue may have profound effects on the oligomerization of MCUR1, essential in scaffolding function. Furthermore, the pH dependent structural changes observed in HdeB, the structural homolog of $MCUR1_{161-209}$ (see discussion section 4.3), and the rapid influx of $H^+$ ions into the mitochondrial matrix from IMS during oxidative phosphorylation, makes it an intriguing area for further research.

The high-resolution solution NMR structure of $MCUR1_{161-209}$ elucidated in my study focuses primarily on the structured region of the MCUR1 matrix domain which is located between the putative coiled coils and a relatively large unstructured region. However, my biophysical analyses conducted on the coiled coil domains has revealed their potential role in stabilization of the homotrimer and $Ca^{2+}$ sensitivity. Moreover, these coiled coil domains have been implicated in the interaction with MCU via its N-terminal domain (Tomar et al., 2016). Future experiments should be designed to focus on the structural elucidation of these coiled coil domains with an aim to map out the MCUR1:MCUR1 and MCU:MCUR1 interfaces at the atomic level. Additionally, the effects of carefully designed charge neutralizing mutations within the CC2 domain of MCUR1 needs to be assessed further to identify the location of the potential $Ca^{2+}$ binding site(s) suggested by my ANS work.

Inherently, while conducting biochemical analysis focusing on a specific domain of interest, we run the risk of omitting long range associations which may play a role in the full-length structural organization and function of the protein. My study focused on characterizing the highly conserved and structured domains of the MCUR1 matrix region; however, the unstructured region located between residue 86 and 160 may also play vital roles in the functioning of MCUR1 as a scaffold for the MCU complex. Indeed, intrinsically disordered regions of proteins are known to mediate important protein network interactions and play a critical role in numerous signaling pathways and cellular processes which include transcription and translation (Dunker et al., 2005; Galea et al., 2008; Iakoucheva et al., 2002; Wright & Dyson, 1999). Some of the identified structural benefits of these intrinsically disordered regions include an ability to interact with targets with high specificity yet low affinity, the presence of easily accessible post-translational modification sites, and fast kinetics of interaction which allows for rapid signal initiation or termination (Dyson & Wright, 2005; Pontius, 1993).

Although most of my experiments, including ANS and solution NMR, were conducted at 35 °C, resembling physiological temperature of mammals, some experiments such as SEC-MALS were conducted at lower temperatures due to the operational setup of the instrumentation. Another digression from physiological norms was applied during my $Ca^{2+}$ sensitivity analysis of MCUR1. High levels of $Ca^{2+}$ (i.e. >10 mM) were used in my *in vitro* experiments to ascertain the maximal response caused by $Ca^{2+}$. The concentration of $Ca^{2+}$ inside the mitochondrial matrix normally ranges between 100 nM to 10 μM, with only certain cell types exceeding 100 μM upon stimulation (Montero et al., 2000). However, it is important to note that mitochondria are generally found in close proximity to the ER where they are exposed to a much higher [$Ca^{2+}$] than the average resting cytosolic levels (Marsault et al., 1997; Rizzuto et al., 1993). Indeed, the artificial shortening of these ER and mitochondrial interactions using synthetic linkers lead to a $Ca^{2+}$ overload in mitochondria, as mitochondria are exposed to these microdomains of much higher cytosolic [$Ca^{2+}$] (Csordas et al., 2006; Dorn & Scorrano, 2010). Additionally, the diffusion theory implies that $Ca^{2+}$ levels found at the base of channel pore may essentially reach the mM range (Bauer, 2001; Chad & Eckert, 1984; Simon & Llinas, 1985). Nonetheless, assessment of the structural and biophysical properties of the MCUR1 matrix domain under physiological environmental conditions may provide new insights into the mechanisms of MCUR1 and MCU regulation.

Currently work is being conducted at the Stathopulos laboratory to explore the identified areas of research. I hope to continue my contribution to the field by maintaining a close association with Dr. P.B. Stathopulos and colleagues.

## 4.7 Conclusion

$Ca^{2+}$ is a universal signaling molecule in the human body. The uptake of $Ca^{2+}$ into the mitochondrial matrix via the MCU complex is not only essential for the regulation of cytosolic $Ca^{2+}$ levels, but also for the proper regulation of vital bioenergetics and biochemical processes within mitochondria such as ATP synthesis and apoptosis. Consequently, the dysregulation of mitochondrial $Ca^{2+}$ uptake has been implicated in numerous diseases including diabetes, cancer, and learning disorders, to name a few (C. V. Logan et al., 2014; Pinton et al., 2008; Tarasov et al., 2012).

MCUR1 plays a crucial regulatory role in the formation and stabilization of the MCU complex. Recent work has demonstrated that an upregulation of MCUR1 protein in hepatocellular carcinomas (HCC) cells leads to increased mitochondrial $Ca^{2+}$ uptake and cell proliferation along with the inhibition of apoptotic pathways (Ren et al., 2018). The decreased apoptotic signaling in these HCC cells is believed to be achieved via the degradation of p53, a tumor suppressor protein, in response to enhanced production of reactive oxygen species (Ren et al., 2018). In contrast, MCUR1 knockdown has previously been shown to confer higher resistance to mPTP opening and cell death by increasing the threshold for mitochondrial $Ca^{2+}$ overload via the MCU complex (Chaudhuri et al., 2016). Indeed, numerous alterations in MCU function have been identified in various cancers, as the uptake of mitochondrial $Ca^{2+}$ appears to play a complex role in cell survival, proliferation, and migration depending on the type and stage of tumor (Vultur et al., 2018).

My high-resolution structure of $MCUR1_{161-209}$ provides the first insights into the atomic basis for the function of an important regulator of this MCU complex. More specifically, my study suggests the $\alpha 1$ and $\alpha 3$ of the compact triple helix domain forms a fundamental binding interface in MCUR1 self-association, while the coiled coil domains may fine tune further assembly into homotrimers. In addition to the previously suggested role in interactions with MCU, my work has now revealed the coiled coil domains also confer $Ca^{2+}$ sensitivity to the MCUR1 matrix region. Therefore, my data not only advances our structural and functional understanding of MCUR1, but also highlights new important questions which will help us better understand the molecular mechanisms underlying MCU function. For example, two prominent avenues of research borne out of my structural elucidation include understanding the impact of post translational modifications and the potential role of pH on MCUR1 assembly and function.

# References

Alam, M. R., Groschner, L. N., Parichatikanond, W., Kuo, L., Bondarenko, A. I., Rost, R., Waldeck-Weiermair, M., Malli, R., & Graier, W. F. (2012). Mitochondrial Ca2+ uptake 1 (MICU1) and mitochondrial ca2+ uniporter (MCU) contribute to metabolism-secretion coupling in clonal pancreatic beta-cells. *J Biol Chem, 287*(41), 34445-34454. doi: 10.1074/jbc.M112.392084

Bagur, R., & Hajnoczky, G. (2017). Intracellular Ca(2+) Sensing: Its Role in Calcium Homeostasis and Signaling. *Mol Cell, 66*(6), 780-788. doi: 10.1016/j.molcel.2017.05.028

Baines, C. P., Kaiser, R. A., Purcell, N. H., Blair, N. S., Osinska, H., Hambleton, M. A., Brunskill, E. W., Sayen, M. R., Gottlieb, R. A., Dorn, G. W., Robbins, J., & Molkentin, J. D. (2005). Loss of cyclophilin D reveals a critical role for mitochondrial permeability transition in cell death. *Nature, 434*(7033), 658-662. doi: 10.1038/nature03434

Bakowski, D., & Parekh, A. B. (2007). Regulation of store-operated calcium channels by the intermediary metabolite pyruvic acid. *Curr Biol, 17*(12), 1076-1081. doi: 10.1016/j.cub.2007.05.041

Baradaran, R., Wang, C., Siliciano, A. F., & Long, S. B. (2018). Cryo-EM structures of fungal and metazoan mitochondrial calcium uniporters. *Nature, 559*(7715), 580-584. doi: 10.1038/s41586-018-0331-8

Barbato, G., Ikura, M., Kay, L. E., Pastor, R. W., & Bax, A. (1992). Backbone dynamics of calmodulin studied by 15N relaxation using inverse detected two-dimensional NMR spectroscopy: the central helix is flexible. *Biochemistry, 31*(23), 5269-5278.

Bartels, C., Xia, T. H., Billeter, M., Guntert, P., & Wuthrich, K. (1995). The program XEASY for computer-supported NMR spectral analysis of biological macromolecules. *J Biomol NMR, 6*(1), 1-10. doi: 10.1007/BF00417486

Basso, E., Fante, L., Fowlkes, J., Petronilli, V., Forte, M. A., & Bernardi, P. (2005). Properties of the permeability transition pore in mitochondria devoid of Cyclophilin D. *J Biol Chem, 280*(19), 18558-18561. doi: 10.1074/jbc.C500089200

Bauer, P. J. (2001). The local Ca concentration profile in the vicinity of a Ca channel. *Cell Biochem Biophys, 35*(1), 49-61. doi: 10.1385/CBB:35:1:49

Baughman, J. M., Perocchi, F., Girgis, H. S., Plovanich, M., Belcher-Timme, C. A., Sancak, Y., Bao, X. R., Strittmatter, L., Goldberger, O., Bogorad, R. L., Koteliansky, V., & Mootha, V. K. (2011). Integrative genomics identifies MCU as an essential component of the mitochondrial calcium uniporter. *Nature, 476*(7360), 341-345. doi: 10.1038/nature10234

Berridge, M. J., Bootman, M. D., & Roderick, H. L. (2003). Calcium signalling: dynamics, homeostasis and remodelling. *Nat Rev Mol Cell Biol, 4*(7), 517-529. doi: 10.1038/nrm1155

Berridge, M. J., Lipp, P., & Bootman, M. D. (2000). The versatility and universality of calcium signalling. *Nat Rev Mol Cell Biol, 1*(1), 11-21. doi: 10.1038/35036035

Bezprozvanny, I., Watras, J., & Ehrlich, B. E. (1991). Bell-shaped calcium-response curves of Ins(1,4,5)P3- and calcium-gated channels from endoplasmic reticulum of cerebellum. *Nature, 351*(6329), 751-754. doi: 10.1038/351751a0

Bhattacharya, A., Tejero, R., & Montelione, G. T. (2007). Evaluating protein structures determined by structural genomics consortia. *Proteins, 66*(4), 778-795. doi: 10.1002/prot.21165

Biasutto, L., Azzolini, M., Szabo, I., & Zoratti, M. (2016). The mitochondrial permeability transition pore in AD 2016: An update. *Biochim Biophys Acta, 1863*(10), 2515-2530. doi: 10.1016/j.bbamcr.2016.02.012

Bick, A. G., Calvo, S. E., & Mootha, V. K. (2012). Evolutionary diversity of the mitochondrial calcium uniporter. *Science, 336*(6083), 886. doi: 10.1126/science.1214977

Billups, B., & Forsythe, I. D. (2002). Presynaptic mitochondrial calcium sequestration influences transmission at mammalian central synapses. *J Neurosci, 22*(14), 5840-5847. doi: 20026597

Bootman, M. D., Higazi, D. R., Coombes, S., & Roderick, H. L. (2006). Calcium signalling during excitation-contraction coupling in mammalian atrial myocytes. *J Cell Sci, 119*(Pt 19), 3915-3925. doi: 10.1242/jcs.03223

Buchan, D. W., Minneci, F., Nugent, T. C., Bryson, K., & Jones, D. T. (2013). Scalable web services for the PSIPRED Protein Analysis Workbench. *Nucleic Acids Res, 41*(Web Server issue), W349-357. doi: 10.1093/nar/gkt381

Carafoli, E. (1987). Intracellular calcium homeostasis. *Annu Rev Biochem, 56*, 395-433. doi: 10.1146/annurev.bi.56.070187.002143

Celsi, F., Pizzo, P., Brini, M., Leo, S., Fotino, C., Pinton, P., & Rizzuto, R. (2009). Mitochondria, calcium and cell death: a deadly triad in neurodegeneration. *Biochim Biophys Acta, 1787*(5), 335-344. doi: 10.1016/j.bbabio.2009.02.021

Chad, J. E., & Eckert, R. (1984). Calcium domains associated with individual channels can account for anomalous voltage relations of CA-dependent responses. *Biophys J, 45*(5), 993-999. doi: 10.1016/S0006-3495(84)84244-7

Chami, M., Ferrari, D., Nicotera, P., Paterlini-Brechot, P., & Rizzuto, R. (2003). Caspase-dependent alterations of Ca2+ signaling in the induction of apoptosis by hepatitis B virus X protein. *J Biol Chem, 278*(34), 31745-31755. doi: 10.1074/jbc.M304202200

Chaudhuri, D., Artiga, D. J., Abiria, S. A., & Clapham, D. E. (2016). Mitochondrial calcium uniporter regulator 1 (MCUR1) regulates the calcium threshold for the mitochondrial permeability transition. *Proc Natl Acad Sci U S A, 113*(13), E1872-1880. doi: 10.1073/pnas.1602264113

Chen, H., & Chan, D. C. (2009). Mitochondrial dynamics--fusion, fission, movement, and mitophagy--in neurodegenerative diseases. *Hum Mol Genet, 18*(R2), R169-176. doi: 10.1093/hmg/ddp326

Clapham, D. E. (2007). Calcium signaling. *Cell, 131*(6), 1047-1058. doi: 10.1016/j.cell.2007.11.028

Combet, C., Blanchet, C., Geourjon, C., & Deleage, G. (2000). NPS@: network protein sequence analysis. *Trends Biochem Sci, 25*(3), 147-150.

Csordas, G., Golenar, T., Seifert, E. L., Kamer, K. J., Sancak, Y., Perocchi, F., Moffat, C., Weaver, D., de la Fuente Perez, S., Bogorad, R., Koteliansky, V., Adijanto, J., Mootha, V. K., & Hajnoczky, G. (2013). MICU1 controls both the threshold and cooperative activation of the mitochondrial Ca(2)(+) uniporter. *Cell Metab, 17*(6), 976-987. doi: 10.1016/j.cmet.2013.04.020

Csordas, G., Renken, C., Varnai, P., Walter, L., Weaver, D., Buttle, K. F., Balla, T., Mannella, C. A., & Hajnoczky, G. (2006). Structural and functional features and significance of the physical linkage between ER and mitochondria. *J Cell Biol, 174*(7), 915-921. doi: 10.1083/jcb.200604016

Csordas, G., Thomas, A. P., & Hajnoczky, G. (1999). Quasi-synaptic calcium signal transmission between endoplasmic reticulum and mitochondria. *EMBO J, 18*(1), 96-108. doi: 10.1093/emboj/18.1.96

Cuervo, A. M. (2010). The plasma membrane brings autophagosomes to life. *Nat Cell Biol, 12*(8), 735-737. doi: 10.1038/ncb0810-735

Dahl, J. U., Koldewey, P., Salmon, L., Horowitz, S., Bardwell, J. C., & Jakob, U. (2015). HdeB functions as an acid-protective chaperone in bacteria. *J Biol Chem, 290*(16), 9950. doi: 10.1074/jbc.A114.612986

De Stefani, D., Raffaello, A., Teardo, E., Szabo, I., & Rizzuto, R. (2011). A forty-kilodalton protein of the inner membrane is the mitochondrial calcium uniporter. *Nature, 476*(7360), 336-340. doi: 10.1038/nature10230

De Stefani, D., Rizzuto, R., & Pozzan, T. (2016). Enjoy the Trip: Calcium in Mitochondria Back and Forth. *Annu Rev Biochem, 85*, 161-192. doi: 10.1146/annurev-biochem-060614-034216

Decuypere, J. P., Monaco, G., Bultynck, G., Missiaen, L., De Smedt, H., & Parys, J. B. (2011). The IP(3) receptor-mitochondria connection in apoptosis and autophagy. *Biochim Biophys Acta, 1813*(5), 1003-1013. doi: 10.1016/j.bbamcr.2010.11.023

Delaglio, F., Grzesiek, S., Vuister, G. W., Zhu, G., Pfeifer, J., & Bax, A. (1995). NMRPipe: a multidimensional spectral processing system based on UNIX pipes. *J Biomol NMR, 6*(3), 277-293.

Ding, J., Yang, C., Niu, X., Hu, Y., & Jin, C. (2015). HdeB chaperone activity is coupled to its intrinsic dynamic properties. *Sci Rep, 5*, 16856. doi: 10.1038/srep16856

Dolmetsch, R. E., Xu, K., & Lewis, R. S. (1998). Calcium oscillations increase the efficiency and specificity of gene expression. *Nature, 392*(6679), 933-936. doi: 10.1038/31960

Dong, Z., Shanmughapriya, S., Tomar, D., Siddiqui, N., Lynch, S., Nemani, N., Breves, S. L., Zhang, X., Tripathi, A., Palaniappan, P., Riitano, M. F., Worth, A. M., Seelam, A., Carvalho, E., Subbiah, R., Jana, F., Soboloff, J., Peng, Y., Cheung, J. Y., Joseph, S. K., Caplan, J., Rajan, S., Stathopulos, P. B., & Madesh, M. (2017). Mitochondrial Ca(2+) Uniporter Is a Mitochondrial Luminal Redox Sensor that Augments MCU Channel Activity. *Mol Cell, 65*(6), 1014-1028 e1017. doi: 10.1016/j.molcel.2017.01.032

Dorn, G. W., 2nd, & Scorrano, L. (2010). Two close, too close: sarcoplasmic reticulum-mitochondrial crosstalk and cardiomyocyte fate. *Circ Res, 107*(6), 689-699. doi: 10.1161/CIRCRESAHA.110.225714

Du, C., Fang, M., Li, Y., Li, L., & Wang, X. (2000). Smac, a mitochondrial protein that promotes cytochrome c-dependent caspase activation by eliminating IAP inhibition. *Cell, 102*(1), 33-42.

Dunker, A. K., Cortese, M. S., Romero, P., Iakoucheva, L. M., & Uversky, V. N. (2005). Flexible nets. The roles of intrinsic disorder in protein interaction networks. *FEBS J, 272*(20), 5129-5148. doi: 10.1111/j.1742-4658.2005.04948.x

Dyson, H. J., & Wright, P. E. (2005). Intrinsically unstructured proteins and their functions. *Nat Rev Mol Cell Biol, 6*(3), 197-208. doi: 10.1038/nrm1589

Emanuelsson, O., Brunak, S., von Heijne, G., & Nielsen, H. (2007). Locating proteins in the cell using TargetP, SignalP and related tools. *Nat Protoc, 2*(4), 953-971. doi: 10.1038/nprot.2007.131

Endo, M. (1977). Calcium release from the sarcoplasmic reticulum. *Physiol Rev, 57*(1), 71-108. doi: 10.1152/physrev.1977.57.1.71

Fan, C., Fan, M., Orlando, B. J., Fastman, N. M., Zhang, J., Xu, Y., Chambers, M. G., Xu, X., Perry, K., Liao, M., & Feng, L. (2018). X-ray and cryo-EM structures of the mitochondrial calcium uniporter. *Nature, 559*(7715), 575-579. doi: 10.1038/s41586-018-0330-9

Feske, S., Gwack, Y., Prakriya, M., Srikanth, S., Puppel, S. H., Tanasa, B., Hogan, P. G., Lewis, R. S., Daly, M., & Rao, A. (2006). A mutation in Orai1 causes immune deficiency by abrogating CRAC channel function. *Nature, 441*(7090), 179-185. doi: 10.1038/nature04702

Franzini-Armstrong, C. (2007). ER-mitochondria communication. How privileged? *Physiology (Bethesda), 22*, 261-268. doi: 10.1152/physiol.00017.2007

Galea, C. A., Wang, Y., Sivakolundu, S. G., & Kriwacki, R. W. (2008). Regulation of cell division by intrinsically unstructured proteins: intrinsic flexibility, modularity, and signaling conduits. *Biochemistry, 47*(29), 7598-7609. doi: 10.1021/bi8006803

Gilabert, J. A., & Parekh, A. B. (2000). Respiring mitochondria determine the pattern of activation and inactivation of the store-operated Ca(2+) current I(CRAC). *EMBO J, 19*(23), 6401-6407. doi: 10.1093/emboj/19.23.6401

Glancy, B., & Balaban, R. S. (2012). Role of mitochondrial Ca2+ in the regulation of cellular energetics. *Biochemistry, 51*(14), 2959-2973. doi: 10.1021/bi2018909

Go, Y. M., Chandler, J. D., & Jones, D. P. (2015). The cysteine proteome. *Free Radic Biol Med, 84*, 227-245. doi: 10.1016/j.freeradbiomed.2015.03.022

Gomes, L. C., Di Benedetto, G., & Scorrano, L. (2011). During autophagy mitochondria elongate, are spared from degradation and sustain cell viability. *Nat Cell Biol, 13*(5), 589-598. doi: 10.1038/ncb2220

Grzesiek, S., & Bax, A. (1992). Correlating backbone amide and side chain resonances in larger proteins by multiple relayed triple resonance NMR. *J Am Chem Soc, 114*(16), 6291-6293. doi: 10.1021/ja00042a003

Grzesiek, S., & Bax, A. (1992). Improved 3D triple-resonance NMR techniques applied to a 31 kDa protein. *Journal of Magnetic Resonance (1969), 96*(2), 432-440. doi: https://doi.org/10.1016/0022-2364(92)90099-S

Grzesiek, S., & Bax, A. (1993). Amino acid type determination in the sequential assignment procedure of uniformly 13C/15N-enriched proteins. *J Biomol NMR, 3*(2), 185-204.

Gunter, T. E., Buntinas, L., Sparagna, G., Eliseev, R., & Gunter, K. (2000). Mitochondrial calcium transport: mechanisms and functions. *Cell Calcium, 28*(5-6), 285-296. doi: 10.1054/ceca.2000.0168

Gunter, T. E., & Pfeiffer, D. R. (1990). Mechanisms by which mitochondria transport calcium. *Am J Physiol, 258*(5 Pt 1), C755-786. doi: 10.1152/ajpcell.1990.258.5.C755

Guntert, P. (2004). Automated NMR structure calculation with CYANA. *Methods Mol Biol, 278*, 353-378. doi: 10.1385/1-59259-809-9:353

Hailey, D. W., Rambold, A. S., Satpute-Krishnan, P., Mitra, K., Sougrat, R., Kim, P. K., & Lippincott-Schwartz, J. (2010). Mitochondria supply membranes for autophagosome biogenesis during starvation. *Cell, 141*(4), 656-667. doi: 10.1016/j.cell.2010.04.009

Hao, L., Rigaud, J. L., & Inesi, G. (1994). Ca2+/H+ countertransport and electrogenicity in proteoliposomes containing erythrocyte plasma membrane Ca-ATPase and exogenous lipids. *J Biol Chem, 269*(19), 14268-14275.

He, C., & Klionsky, D. J. (2009). Regulation mechanisms and signaling pathways of autophagy. *Annu Rev Genet, 43*, 67-93. doi: 10.1146/annurev-genet-102808-114910

Hess, D. T., & Stamler, J. S. (2012). Regulation by S-nitrosylation of protein post-translational modification. *J Biol Chem, 287*(7), 4411-4418. doi: 10.1074/jbc.R111.285742

Hoeflich, K. P., & Ikura, M. (2002). Calmodulin in action: diversity in target recognition and activation mechanisms. *Cell, 108*(6), 739-742.

Hofmann, K., & Stoffel, W. (1992). PROFILEGRAPH: an interactive graphical tool for protein sequence analysis. *Comput Appl Biosci, 8*(4), 331-337.

Holm, L., & Sander, C. (1995). Dali: a network tool for protein structure comparison. *Trends Biochem Sci, 20*(11), 478-480.

Holzwarth, G., & Doty, P. (1965). The Ultraviolet Circular Dichroism of Polypeptides. *J Am Chem Soc, 87*, 218-228.

Hong, W., Wu, Y. E., Fu, X., & Chang, Z. (2012). Chaperone-dependent mechanisms for acid resistance in enteric bacteria. *Trends Microbiol, 20*(7), 328-335. doi: 10.1016/j.tim.2012.03.001

Hoth, M., Fanger, C. M., & Lewis, R. S. (1997). Mitochondrial regulation of store-operated calcium signaling in T lymphocytes. *J Cell Biol, 137*(3), 633-648.

Hung, V., Zou, P., Rhee, H. W., Udeshi, N. D., Cracan, V., Svinkina, T., Carr, S. A., Mootha, V. K., & Ting, A. Y. (2014). Proteomic mapping of the human mitochondrial intermembrane space in live cells via ratiometric APEX tagging. *Mol Cell, 55*(2), 332-341. doi: 10.1016/j.molcel.2014.06.003

Iakoucheva, L. M., Brown, C. J., Lawson, J. D., Obradovic, Z., & Dunker, A. K. (2002). Intrinsic disorder in cell-signaling and cancer-associated proteins. *J Mol Biol, 323*(3), 573-584.

Ikemoto, N., Antoniu, B., Kang, J. J., Meszaros, L. G., & Ronjat, M. (1991). Intravesicular calcium transient during calcium release from sarcoplasmic reticulum. *Biochemistry, 30*(21), 5230-5237.

Ikura, M., Kay, L. E., & Bax, A. (1990). A novel approach for sequential assignment of 1H, 13C, and 15N spectra of proteins: heteronuclear triple-resonance three-dimensional NMR spectroscopy. Application to calmodulin. *Biochemistry, 29*(19), 4659-4667.

Jiang, D., Zhao, L., & Clapham, D. E. (2009). Genome-wide RNAi screen identifies Letm1 as a mitochondrial Ca2+/H+ antiporter. *Science, 326*(5949), 144-147. doi: 10.1126/science.1175145

John, B. K., Plant, D., & Hurd, R. E. (1993). Improved Proton-Detected Heteronuclear Correlation Using Gradient-Enhanced z and zz Filters. *Journal of Magnetic Resonance, Series A, 101*(1), 113-117. doi: https://doi.org/10.1006/jmra.1993.1019

Jouaville, L. S., Pinton, P., Bastianutto, C., Rutter, G. A., & Rizzuto, R. (1999). Regulation of mitochondrial ATP synthesis by calcium: evidence for a long-term metabolic priming. *Proc Natl Acad Sci U S A, 96*(24), 13807-13812.

Jousset, H., Frieden, M., & Demaurex, N. (2007). STIM1 knockdown reveals that store-operated Ca2+ channels located close to sarco/endoplasmic Ca2+ ATPases (SERCA) pumps silently refill the endoplasmic reticulum. *J Biol Chem, 282*(15), 11456-11464. doi: 10.1074/jbc.M609551200

Jurrus, E., Engel, D., Star, K., Monson, K., Brandi, J., Felberg, L. E., Brookes, D. H., Wilson, L., Chen, J., Liles, K., Chun, M., Li, P., Gohara, D. W., Dolinsky, T., Konecny, R., Koes, D. R., Nielsen, J. E., Head-Gordon, T., Geng, W., Krasny, R., Wei, G. W., Holst, M. J., McCammon, J. A., & Baker, N. A. (2018). Improvements to the APBS biomolecular solvation software suite. *Protein Sci, 27*(1), 112-128. doi: 10.1002/pro.3280

Kamer, K. J., & Mootha, V. K. (2014). MICU1 and MICU2 play nonredundant roles in the regulation of the mitochondrial calcium uniporter. *EMBO Rep, 15*(3), 299-307. doi: 10.1002/embr.201337946

Kay, L., Keifer, P., & Saarinen, T. (1992). Pure absorption gradient enhanced heteronuclear single quantum correlation spectroscopy with improved sensitivity. *J Am Chem Soc, 114*(26), 10663-10665. doi: 10.1021/ja00052a088

Kay, L. E., Clore, G. M., Bax, A., & Gronenborn, A. M. (1990). Four-dimensional heteronuclear triple-resonance NMR spectroscopy of interleukin-1 beta in solution. *Science, 249*(4967), 411-414.

Kay, L. E., Ikura, M., Tschudin, R., & Bax, A. (2011). Three-dimensional triple-resonance NMR Spectroscopy of isotopically enriched proteins. 1990. *J Magn Reson, 213*(2), 423-441. doi: 10.1016/j.jmr.2011.09.004

Kay, L. E., Torchia, D. A., & Bax, A. (1989). Backbone dynamics of proteins as studied by 15N inverse detected heteronuclear NMR spectroscopy: application to staphylococcal nuclease. *Biochemistry, 28*(23), 8972-8979.

Kay, L. E., Xu, G. Y., Singer, A. U., Muhandiram, D. R., & Formankay, J. D. (1993). A Gradient-Enhanced HCCH-TOCSY Experiment for Recording Side-Chain <SUP>1</SUP>H and <SUP>13</SUP>C Correlations in H <SUB>2</SUB>O Samples of Proteins. *Journal of Magnetic Resonance, Series B, Volume 101, Issue 3, p. 333-337., 101*, 333-337. doi: 10.1006/jmrb.1993.1053

Kay, L. E., Xu, G. Y., & Yamazaki, T. (1994). Enhanced-Sensitivity Triple-Resonance Spectroscopy with Minimal H <SUB>2</SUB>O Saturation. *Journal of Magnetic Resonance, Series A, Volume 109, Issue 1, p. 129-133., 109*, 129-133. doi: 10.1006/jmra.1994.1145

Keller, R. L. J., Meier, B. H., & Pervushin, K. *Optimizing the process of nuclear magnetic resonance spectrum analysis and computer aided resonance assignment.* (Diss , Naturwissenschaften, Eidgenössische Technische Hochschule ETH Zürich, Nr 15947, 2005).

Kern, R., Malki, A., Abdallah, J., Tagourti, J., & Richarme, G. (2007). Escherichia coli HdeB is an acid stress chaperone. *J Bacteriol, 189*(2), 603-610. doi: 10.1128/JB.01522-06

Kirichok, Y., Krapivinsky, G., & Clapham, D. E. (2004). The mitochondrial calcium uniporter is a highly selective ion channel. *Nature, 427*(6972), 360-364. doi: 10.1038/nature02246

Kupce, E. (1997). Effect of sweep direction on sidebands in adiabatic decoupling. *J Magn Reson, 129*(2), 219-221. doi: 10.1006/jmre.1997.1279

Kuwana, T., Mackey, M. R., Perkins, G., Ellisman, M. H., Latterich, M., Schneiter, R., Green, D. R., & Newmeyer, D. D. (2002). Bid, Bax, and lipids cooperate to form supramolecular openings in the outer mitochondrial membrane. *Cell, 111*(3), 331-342.

Lanner, J. T., Georgiou, D. K., Joshi, A. D., & Hamilton, S. L. (2010). Ryanodine receptors: structure, expression, molecular details, and function in calcium release. *Cold Spring Harb Perspect Biol, 2*(11), a003996. doi: 10.1101/cshperspect.a003996

Lasorsa, F. M., Pinton, P., Palmieri, L., Fiermonte, G., Rizzuto, R., & Palmieri, F. (2003). Recombinant expression of the Ca(2+)-sensitive aspartate/glutamate carrier increases mitochondrial ATP production in agonist-stimulated Chinese hamster ovary cells. *J Biol Chem, 278*(40), 38686-38692. doi: 10.1074/jbc.M304988200

Lee, S. K., Shanmughapriya, S., Mok, M. C. Y., Dong, Z., Tomar, D., Carvalho, E., Rajan, S., Junop, M. S., Madesh, M., & Stathopulos, P. B. (2016). Structural Insights into Mitochondrial Calcium Uniporter Regulation by Divalent Cations. *Cell Chem Biol, 23*(9), 1157-1169. doi: 10.1016/j.chembiol.2016.07.012

Lee, Y., Min, C. K., Kim, T. G., Song, H. K., Lim, Y., Kim, D., Shin, K., Kang, M., Kang, J. Y., Youn, H. S., Lee, J. G., An, J. Y., Park, K. R., Lim, J. J., Kim, J. H., Kim, J. H., Park, Z. Y., Kim, Y. S., Wang, J., Kim, D. H., & Eom, S. H. (2015). Structure and function of the N-terminal domain of the human mitochondrial calcium uniporter. *EMBO Rep, 16*(10), 1318-1333. doi: 10.15252/embr.201540436

Lemasters, J. J. (2005). Selective mitochondrial autophagy, or mitophagy, as a targeted defense against oxidative stress, mitochondrial dysfunction, and aging. *Rejuvenation Res, 8*(1), 3-5. doi: 10.1089/rej.2005.8.3

Lemasters, J. J., Nieminen, A. L., Qian, T., Trost, L. C., Elmore, S. P., Nishimura, Y., Crowe, R. A., Cascio, W. E., Bradham, C. A., Brenner, D. A., & Herman, B. (1998). The mitochondrial permeability transition in cell death: a common mechanism in necrosis, apoptosis and autophagy. *Biochim Biophys Acta, 1366*(1-2), 177-196.

Leung, A. W., & Halestrap, A. P. (2008). Recent progress in elucidating the molecular mechanism of the mitochondrial permeability transition pore. *Biochim Biophys Acta, 1777*(7-8), 946-952. doi: 10.1016/j.bbabio.2008.03.009

Liou, J., Kim, M. L., Heo, W. D., Jones, J. T., Myers, J. W., Ferrell, J. E., Jr., & Meyer, T. (2005). STIM is a Ca2+ sensor essential for Ca2+-store-depletion-triggered Ca2+ influx. *Curr Biol, 15*(13), 1235-1241. doi: 10.1016/j.cub.2005.05.055

Liu, X., Kim, C. N., Yang, J., Jemmerson, R., & Wang, X. (1996). Induction of apoptotic program in cell-free extracts: requirement for dATP and cytochrome c. *Cell, 86*(1), 147-157.

Logan, C. V., Szabadkai, G., Sharpe, J. A., Parry, D. A., Torelli, S., Childs, A. M., Kriek, M., Phadke, R., Johnson, C. A., Roberts, N. Y., Bonthron, D. T., Pysden, K. A., Whyte, T., Munteanu, I., Foley, A. R., Wheway, G., Szymanska, K., Natarajan, S., Abdelhamed, Z. A., Morgan, J. E., Roper, H., Santen, G. W., Niks, E. H., van der Pol, W. L., Lindhout, D., Raffaello, A., De Stefani, D., den Dunnen, J. T., Sun, Y., Ginjaar, I., Sewry, C. A., Hurles, M., Rizzuto, R., Consortium, U. K., Duchen, M. R., Muntoni, F., & Sheridan, E. (2014). Loss-of-function mutations in MICU1 cause a brain and muscle disorder linked to primary alterations in mitochondrial calcium signaling. *Nat Genet, 46*(2), 188-193. doi: 10.1038/ng.2851

Logan, T. M., Olejniczak, E. T., Xu, R. X., & Fesik, S. W. (1992). Side chain and backbone assignments in isotopically labeled proteins from two heteronuclear triple resonance experiments. *FEBS Lett, 314*(3), 413-418.

Lupas, A., Van Dyke, M., & Stock, J. (1991). Predicting coiled coils from protein sequences. *Science, 252*(5009), 1162-1164. doi: 10.1126/science.252.5009.1162

Madesh, M., & Hajnoczky, G. (2001). VDAC-dependent permeabilization of the outer mitochondrial membrane by superoxide induces rapid and massive cytochrome c release. *J Cell Biol, 155*(6), 1003-1015. doi: 10.1083/jcb.200105057

Mal, T. K., Bagby, S., & Ikura, M. (2002). Protein structure calculation from NMR data. *Methods Mol Biol, 173*, 267-283. doi: 10.1385/1-59259-184-1:267

Malli, R., Naghdi, S., Romanin, C., & Graier, W. F. (2008). Cytosolic Ca2+ prevents the subplasmalemmal clustering of STIM1: an intrinsic mechanism to avoid Ca2+ overload. *J Cell Sci, 121*(Pt 19), 3133-3139. doi: 10.1242/jcs.034496

Mallilankaraman, K., Cardenas, C., Doonan, P. J., Chandramoorthy, H. C., Irrinki, K. M., Golenar, T., Csordas, G., Madireddi, P., Yang, J., Muller, M., Miller, R., Kolesar, J. E., Molgo, J., Kaufman, B., Hajnoczky, G., Foskett, J. K., & Madesh, M. (2012). MCUR1 is an essential component of mitochondrial Ca2+ uptake that regulates cellular metabolism. *Nat Cell Biol, 14*(12), 1336-1343. doi: 10.1038/ncb2622

Mallilankaraman, K., Doonan, P., Cardenas, C., Chandramoorthy, H. C., Muller, M., Miller, R., Hoffman, N. E., Gandhirajan, R. K., Molgo, J., Birnbaum, M. J., Rothberg, B. S., Mak, D. O., Foskett, J. K., & Madesh, M. (2012). MICU1 is an essential gatekeeper for MCU-mediated mitochondrial Ca(2+) uptake that regulates cell survival. *Cell, 151*(3), 630-644. doi: 10.1016/j.cell.2012.10.011

Mammucari, C., Raffaello, A., Vecellio Reane, D., & Rizzuto, R. (2016). Molecular structure and pathophysiological roles of the Mitochondrial Calcium Uniporter. *Biochim Biophys Acta, 1863*(10), 2457-2464. doi: 10.1016/j.bbamcr.2016.03.006

Marchi, S., Lupini, L., Patergnani, S., Rimessi, A., Missiroli, S., Bonora, M., Bononi, A., Corra, F., Giorgi, C., De Marchi, E., Poletti, F., Gafa, R., Lanza, G., Negrini, M., Rizzuto, R., & Pinton, P. (2013). Downregulation of the mitochondrial calcium uniporter by cancer-related miR-25. *Curr Biol, 23*(1), 58-63. doi: 10.1016/j.cub.2012.11.026

Marsault, R., Murgia, M., Pozzan, T., & Rizzuto, R. (1997). Domains of high Ca2+ beneath the plasma membrane of living A7r5 cells. *EMBO J, 16*(7), 1575-1581. doi: 10.1093/emboj/16.7.1575

Martell, J. D., Deerinck, T. J., Sancak, Y., Poulos, T. L., Mootha, V. K., Sosinsky, G. E., Ellisman, M. H., & Ting, A. Y. (2012). Engineered ascorbate peroxidase as a genetically encoded reporter for electron microscopy. *Nat Biotechnol, 30*(11), 1143-1148. doi: 10.1038/nbt.2375

Matesanz-Isabel, J., Arias-del-Val, J., Alvarez-Illera, P., Fonteriz, R. I., Montero, M., & Alvarez, J. (2016). Functional roles of MICU1 and MICU2 in mitochondrial Ca(2+) uptake. *Biochim Biophys Acta, 1858*(6), 1110-1117. doi: 10.1016/j.bbamem.2016.02.022

Mayrleitner, M., Chandler, R., Schindler, H., & Fleischer, S. (1995). Phosphorylation with protein kinases modulates calcium loading of terminal cisternae of sarcoplasmic reticulum from skeletal muscle. *Cell Calcium, 18*(3), 197-206.

McStay, G. P. (2017). Complex formation and turnover of mitochondrial transporters and ion channels. *J Bioenerg Biomembr, 49*(1), 101-111. doi: 10.1007/s10863-016-9648-x

Montalvo, G. B., Artalejo, A. R., & Gilabert, J. A. (2006). ATP from subplasmalemmal mitochondria controls Ca2+-dependent inactivation of CRAC channels. *J Biol Chem, 281*(47), 35616-35623. doi: 10.1074/jbc.M603518200

Montero, M., Alonso, M. T., Carnicero, E., Cuchillo-Ibanez, I., Albillos, A., Garcia, A. G., Garcia-Sancho, J., & Alvarez, J. (2000). Chromaffin-cell stimulation triggers fast millimolar mitochondrial Ca2+ transients that modulate secretion. *Nat Cell Biol, 2*(2), 57-61. doi: 10.1038/35000001

Montero, M., Lobaton, C. D., Moreno, A., & Alvarez, J. (2002). A novel regulatory mechanism of the mitochondrial Ca2+ uniporter revealed by the p38 mitogen-activated protein kinase inhibitor SB202190. *FASEB J, 16*(14), 1955-1957. doi: 10.1096/fj.02-0553fje

Muhandiram, D. R., & Kay, L. E. (1994). Gradient-Enhanced Triple-Resonance Three-Dimensional NMR Experiments with Improved Sensitivity. *Journal of Magnetic Resonance, Series B, 103*(3), 203-216. doi: https://doi.org/10.1006/jmrb.1994.1032

Mungai, P. T., Waypa, G. B., Jairaman, A., Prakriya, M., Dokic, D., Ball, M. K., & Schumacker, P. T. (2011). Hypoxia triggers AMPK activation through reactive oxygen species-mediated activation of calcium release-activated calcium channels. *Mol Cell Biol, 31*(17), 3531-3545. doi: 10.1128/MCB.05124-11

Nakagawa, T., Shimizu, S., Watanabe, T., Yamaguchi, O., Otsu, K., Yamagata, H., Inohara, H., Kubo, T., & Tsujimoto, Y. (2005). Cyclophilin D-dependent mitochondrial permeability transition regulates some necrotic but not apoptotic cell death. *Nature, 434*(7033), 652-658. doi: 10.1038/nature03317

Nakai, J., Sekiguchi, N., Rando, T. A., Allen, P. D., & Beam, K. G. (1998). Two regions of the ryanodine receptor involved in coupling with L-type Ca2+ channels. *J Biol Chem, 273*(22), 13403-13406.

Nguyen, N. X., Armache, J. P., Lee, C., Yang, Y., Zeng, W., Mootha, V. K., Cheng, Y., Bai, X. C., & Jiang, Y. (2018). Cryo-EM structure of a fungal mitochondrial calcium uniporter. *Nature, 559*(7715), 570-574. doi: 10.1038/s41586-018-0333-6

O'Rourke, B. (2000). Pathophysiological and protective roles of mitochondrial ion channels. *J Physiol, 529 Pt 1*, 23-36.

Oxenoid, K., Dong, Y., Cao, C., Cui, T., Sancak, Y., Markhard, A. L., Grabarek, Z., Kong, L., Liu, Z., Ouyang, B., Cong, Y., Mootha, V. K., & Chou, J. J. (2016). Architecture of the mitochondrial calcium uniporter. *Nature, 533*(7602), 269-273. doi: 10.1038/nature17656

Pacher, P., Thomas, A. P., & Hajnoczky, G. (2002). Ca2+ marks: miniature calcium signals in single mitochondria driven by ryanodine receptors. *Proc Natl Acad Sci U S A, 99*(4), 2380-2385. doi: 10.1073/pnas.032423699

Pagliarini, D. J., Calvo, S. E., Chang, B., Sheth, S. A., Vafai, S. B., Ong, S. E., Walford, G. A., Sugiana, C., Boneh, A., Chen, W. K., Hill, D. E., Vidal, M., Evans, J. G., Thorburn, D. R., Carr, S. A., & Mootha, V. K. (2008). A mitochondrial protein compendium elucidates complex I disease biology. *Cell, 134*(1), 112-123. doi: 10.1016/j.cell.2008.06.016

Palty, R., Ohana, E., Hershfinkel, M., Volokita, M., Elgazar, V., Beharier, O., Silverman, W. F., Argaman, M., & Sekler, I. (2004). Lithium-calcium exchange is mediated by a distinct potassium-independent sodium-calcium exchanger. *J Biol Chem, 279*(24), 25234-25240. doi: 10.1074/jbc.M401229200

Patergnani, S., Suski, J. M., Agnoletto, C., Bononi, A., Bonora, M., De Marchi, E., Giorgi, C., Marchi, S., Missiroli, S., Poletti, F., Rimessi, A., Duszynski, J., Wieckowski, M. R., & Pinton, P. (2011). Calcium signaling around Mitochondria Associated Membranes (MAMs). *Cell Commun Signal, 9*, 19. doi: 10.1186/1478-811X-9-19

Patron, M., Checchetto, V., Raffaello, A., Teardo, E., Vecellio Reane, D., Mantoan, M., Granatiero, V., Szabo, I., De Stefani, D., & Rizzuto, R. (2014). MICU1 and MICU2 finely tune the mitochondrial Ca2+ uniporter by exerting opposite effects on MCU activity. *Mol Cell, 53*(5), 726-737. doi: 10.1016/j.molcel.2014.01.013

Paupe, V., Prudent, J., Dassa, E. P., Rendon, O. Z., & Shoubridge, E. A. (2015). CCDC90A (MCUR1) is a cytochrome c oxidase assembly factor and not a regulator of the mitochondrial calcium uniporter. *Cell Metab, 21*(1), 109-116. doi: 10.1016/j.cmet.2014.12.004

Perocchi, F., Gohil, V. M., Girgis, H. S., Bao, X. R., McCombs, J. E., Palmer, A. E., & Mootha, V. K. (2010). MICU1 encodes a mitochondrial EF hand protein required for Ca(2+) uptake. *Nature, 467*(7313), 291-296. doi: 10.1038/nature09358

Pinton, P., Ferrari, D., Rapizzi, E., Di Virgilio, F., Pozzan, T., & Rizzuto, R. (2001). The Ca2+ concentration of the endoplasmic reticulum is a key determinant of ceramide-induced apoptosis: significance for the molecular mechanism of Bcl-2 action. *EMBO J, 20*(11), 2690-2701. doi: 10.1093/emboj/20.11.2690

Pinton, P., Giorgi, C., Siviero, R., Zecchini, E., & Rizzuto, R. (2008). Calcium and apoptosis: ER-mitochondria Ca2+ transfer in the control of apoptosis. *Oncogene, 27*(50), 6407-6418. doi: 10.1038/onc.2008.308

Pinton, P., Leo, S., Wieckowski, M. R., Di Benedetto, G., & Rizzuto, R. (2004). Long-term modulation of mitochondrial Ca2+ signals by protein kinase C isozymes. *J Cell Biol, 165*(2), 223-232. doi: 10.1083/jcb.200311061

Plovanich, M., Bogorad, R. L., Sancak, Y., Kamer, K. J., Strittmatter, L., Li, A. A., Girgis, H. S., Kuchimanchi, S., De Groot, J., Speciner, L., Taneja, N., Oshea, J., Koteliansky, V., & Mootha, V. K. (2013). MICU2, a paralog of MICU1, resides within the mitochondrial uniporter complex to regulate calcium handling. *PLoS One, 8*(2), e55785. doi: 10.1371/journal.pone.0055785

Pontius, B. W. (1993). Close encounters: why unstructured, polymeric domains can increase rates of specific macromolecular association. *Trends Biochem Sci, 18*(5), 181-186.

Pozzan, T., Bragadin, M., & Azzone, G. F. (1977). Disequilibrium between steady-state Ca2+ accumulation ratio and membrane potential in mitochondria. Pathway and role of Ca2+ efflux. *Biochemistry, 16*(25), 5618-5625.

Pozzan, T., Rizzuto, R., Volpe, P., & Meldolesi, J. (1994). Molecular and cellular physiology of intracellular calcium stores. *Physiol Rev, 74*(3), 595-636. doi: 10.1152/physrev.1994.74.3.595

Prakriya, M., & Lewis, R. S. (2015). Store-Operated Calcium Channels. *Physiol Rev, 95*(4), 1383-1436. doi: 10.1152/physrev.00020.2014

Quintana, A., Schwarz, E. C., Schwindling, C., Lipp, P., Kaestner, L., & Hoth, M. (2006). Sustained activity of calcium release-activated calcium channels requires translocation of mitochondria to the plasma membrane. *J Biol Chem, 281*(52), 40302-40309. doi: 10.1074/jbc.M607896200

Raffaello, A., De Stefani, D., & Rizzuto, R. (2012). The mitochondrial Ca(2+) uniporter. *Cell Calcium, 52*(1), 16-21. doi: 10.1016/j.ceca.2012.04.006

Raffaello, A., De Stefani, D., Sabbadin, D., Teardo, E., Merli, G., Picard, A., Checchetto, V., Moro, S., Szabo, I., & Rizzuto, R. (2013). The mitochondrial calcium uniporter is a multimer that can include a dominant-negative pore-forming subunit. *EMBO J, 32*(17), 2362-2376. doi: 10.1038/emboj.2013.157

Ren, T., Wang, J., Zhang, H., Yuan, P., Zhu, J., Wu, Y., Huang, Q., Guo, X., Zhang, J., Ji, L., Li, J., Zhang, H., Yang, H., & Xing, J. (2018). MCUR1-Mediated Mitochondrial Calcium Signaling Facilitates Cell Survival of Hepatocellular Carcinoma via Reactive Oxygen Species-Dependent P53 Degradation. *Antioxid Redox Signal, 28*(12), 1120-1136. doi: 10.1089/ars.2017.6990

Rios, E., & Brum, G. (1987). Involvement of dihydropyridine receptors in excitation-contraction coupling in skeletal muscle. *Nature, 325*(6106), 717-720. doi: 10.1038/325717a0

Rizzuto, R., Brini, M., Murgia, M., & Pozzan, T. (1993). Microdomains with high Ca2+ close to IP3-sensitive channels that are sensed by neighboring mitochondria. *Science, 262*(5134), 744-747.

Rizzuto, R., De Stefani, D., Raffaello, A., & Mammucari, C. (2012). Mitochondria as sensors and regulators of calcium signalling. *Nat Rev Mol Cell Biol, 13*(9), 566-578. doi: 10.1038/nrm3412

Rizzuto, R., Marchi, S., Bonora, M., Aguiari, P., Bononi, A., De Stefani, D., Giorgi, C., Leo, S., Rimessi, A., Siviero, R., Zecchini, E., & Pinton, P. (2009). Ca(2+) transfer from the ER to mitochondria: when, how and why. *Biochim Biophys Acta, 1787*(11), 1342-1351. doi: 10.1016/j.bbabio.2009.03.015

Rizzuto, R., & Pozzan, T. (2006). Microdomains of intracellular Ca2+: molecular determinants and functional consequences. *Physiol Rev, 86*(1), 369-408. doi: 10.1152/physrev.00004.2005

Rose, A., & Meier, I. (2004). Scaffolds, levers, rods and springs: diverse cellular functions of long coiled-coil proteins. *Cell Mol Life Sci, 61*(16), 1996-2009. doi: 10.1007/s00018-004-4039-6

Rotzschke, O., Lau, J. M., Hofstatter, M., Falk, K., & Strominger, J. L. (2002). A pH-sensitive histidine residue as control element for ligand release from HLA-DR molecules. *Proc Natl Acad Sci U S A, 99*(26), 16946-16950. doi: 10.1073/pnas.212643999

Sabatini, B. L., Oertner, T. G., & Svoboda, K. (2002). The life cycle of Ca(2+) ions in dendritic spines. *Neuron, 33*(3), 439-452.

Sancak, Y., Markhard, A. L., Kitami, T., Kovacs-Bogdan, E., Kamer, K. J., Udeshi, N. D., Carr, S. A., Chaudhuri, D., Clapham, D. E., Li, A. A., Calvo, S. E., Goldberger, O., & Mootha, V. K. (2013). EMRE is an essential component of the mitochondrial calcium uniporter complex. *Science, 342*(6164), 1379-1382. doi: 10.1126/science.1242993

Sattler, M., Schwendinger, M. G., Schleucher, J., & Griesinger, C. (1995). Novel strategies for sensitivity enhancement in heteronuclear multi-dimensional NMR experiments employing pulsed field gradients. *J Biomol NMR, 6*(1), 11-22. doi: 10.1007/BF00417487

Schnell, J. R., Zhou, G. P., Zweckstetter, M., Rigby, A. C., & Chou, J. J. (2005). Rapid and accurate structure determination of coiled-coil domains using NMR dipolar couplings: application to cGMP-dependent protein kinase Ialpha. *Protein Sci, 14*(9), 2421-2428. doi: 10.1110/ps.051528905

Schrodinger, LLC. (2015). *The PyMOL Molecular Graphics System, Version 1.8*.

Shen, Y., & Bax, A. (2015). Protein structural information derived from NMR chemical shift with the neural network program TALOS-N. *Methods Mol Biol, 1260*, 17-32. doi: 10.1007/978-1-4939-2239-0_2

Shen, Y., Delaglio, F., Cornilescu, G., & Bax, A. (2009). TALOS+: a hybrid method for predicting protein backbone torsion angles from NMR chemical shifts. *J Biomol NMR, 44*(4), 213-223. doi: 10.1007/s10858-009-9333-z

Sievers, F., Wilm, A., Dineen, D., Gibson, T. J., Karplus, K., Li, W., Lopez, R., McWilliam, H., Remmert, M., Soding, J., Thompson, J. D., & Higgins, D. G. (2011). Fast, scalable generation of high-quality protein multiple sequence alignments using Clustal Omega. *Mol Syst Biol, 7*, 539. doi: 10.1038/msb.2011.75

Simon, S. M., & Llinas, R. R. (1985). Compartmentalization of the submembrane calcium activity during calcium influx and its significance in transmitter release. *Biophys J, 48*(3), 485-498. doi: 10.1016/S0006-3495(85)83804-2

Singh, R., & Cuervo, A. M. (2011). Autophagy in the cellular energetic balance. *Cell Metab, 13*(5), 495-504. doi: 10.1016/j.cmet.2011.04.004

Smith, J. S., Coronado, R., & Meissner, G. (1986). Single channel measurements of the calcium release channel from skeletal muscle sarcoplasmic reticulum. Activation by Ca2+ and ATP and modulation by Mg2+. *J Gen Physiol, 88*(5), 573-588.

Stathopulos, P. B., Schindl, R., Fahrner, M., Zheng, L., Gasmi-Seabrook, G. M., Muik, M., Romanin, C., & Ikura, M. (2013). STIM1/Orai1 coiled-coil interplay in the regulation of store-operated calcium entry. *Nat Commun, 4*, 2963. doi: 10.1038/ncomms3963

Stathopulos, P. B., Zheng, L., Li, G. Y., Plevin, M. J., & Ikura, M. (2008). Structural and mechanistic insights into STIM1-mediated initiation of store-operated calcium entry. *Cell, 135*(1), 110-122. doi: 10.1016/j.cell.2008.08.006

Susin, S. A., Zamzami, N., Castedo, M., Hirsch, T., Marchetti, P., Macho, A., Daugas, E., Geuskens, M., & Kroemer, G. (1996). Bcl-2 inhibits the mitochondrial release of an apoptogenic protease. *J Exp Med, 184*(4), 1331-1341.

Tanford, C. (1982). Steady state of an ATP-driven calcium pump: limitations on kinetic and thermodynamic parameters. *Proc Natl Acad Sci U S A, 79*(20), 6161-6165.

Tapley, T. L., Franzmann, T. M., Chakraborty, S., Jakob, U., & Bardwell, J. C. (2010). Protein refolding by pH-triggered chaperone binding and release. *Proc Natl Acad Sci U S A, 107*(3), 1071-1076. doi: 10.1073/pnas.0911610107

Tarasov, A. I., Semplici, F., Ravier, M. A., Bellomo, E. A., Pullen, T. J., Gilon, P., Sekler, I., Rizzuto, R., & Rutter, G. A. (2012). The mitochondrial Ca2+ uniporter MCU is essential for glucose-induced ATP increases in pancreatic beta-cells. *PLoS One, 7*(7), e39722. doi: 10.1371/journal.pone.0039722

Tomar, D., Dong, Z., Shanmughapriya, S., Koch, D. A., Thomas, T., Hoffman, N. E., Timbalia, S. A., Goldman, S. J., Breves, S. L., Corbally, D. P., Nemani, N., Fairweather, J. P., Cutri, A. R., Zhang, X., Song, J., Jana, F., Huang, J., Barrero, C., Rabinowitz, J. E., Luongo, T. S., Schumacher, S. M., Rockman, M. E., Dietrich, A., Merali, S., Caplan, J., Stathopulos, P., Ahima, R. S., Cheung, J. Y., Houser, S. R., Koch, W. J., Patel, V., Gohil, V. M., Elrod, J. W., Rajan, S., & Madesh, M. (2016). MCUR1 Is a Scaffold Factor for the MCU Complex Function and Promotes Mitochondrial Bioenergetics. *Cell Rep, 15*(8), 1673-1685. doi: 10.1016/j.celrep.2016.04.050

Tsai, M. F., Phillips, C. B., Ranaghan, M., Tsai, C. W., Wu, Y., Willliams, C., & Miller, C. (2016). Dual functions of a small regulatory subunit in the mitochondrial calcium uniporter complex. *Elife, 5*. doi: 10.7554/eLife.15545

Vais, H., Mallilankaraman, K., Mak, D. D., Hoff, H., Payne, R., Tanis, J. E., & Foskett, J. K. (2016). EMRE Is a Matrix Ca(2+) Sensor that Governs Gatekeeping of the Mitochondrial Ca(2+) Uniporter. *Cell Rep, 14*(3), 403-410. doi: 10.1016/j.celrep.2015.12.054

Vais, H., Tanis, J. E., Muller, M., Payne, R., Mallilankaraman, K., & Foskett, J. K. (2015). MCUR1, CCDC90A, Is a Regulator of the Mitochondrial Calcium Uniporter. *Cell Metab, 22*(4), 533-535. doi: 10.1016/j.cmet.2015.09.015

van Vliet, A. R., Verfaillie, T., & Agostinis, P. (2014). New functions of mitochondria associated membranes in cellular signaling. *Biochim Biophys Acta, 1843*(10), 2253-2262. doi: 10.1016/j.bbamcr.2014.03.009

Verhagen, A. M., Ekert, P. G., Pakusch, M., Silke, J., Connolly, L. M., Reid, G. E., Moritz, R. L., Simpson, R. J., & Vaux, D. L. (2000). Identification of DIABLO, a mammalian protein that promotes apoptosis by binding to and antagonizing IAP proteins. *Cell, 102*(1), 43-53.

Voronina, S., Sukhomlin, T., Johnson, P. R., Erdemli, G., Petersen, O. H., & Tepikin, A. (2002). Correlation of NADH and Ca2+ signals in mouse pancreatic acinar cells. *J Physiol, 539*(Pt 1), 41-52.

Vultur, A., Gibhardt, C. S., Stanisz, H., & Bogeski, I. (2018). The role of the mitochondrial calcium uniporter (MCU) complex in cancer. *Pflugers Arch*. doi: 10.1007/s00424-018-2162-8

Wallace, D. C. (2012). Mitochondria and cancer. *Nat Rev Cancer, 12*(10), 685-698. doi: 10.1038/nrc3365

Wang, A. C., Lodi, P. J., Qin, J., Vuister, G. W., Gronenborn, A. M., & Clore, G. M. (1994). An efficient triple-resonance experiment for proton-directed sequential backbone assignment of medium-sized proteins. *J Magn Reson B, 105*(2), 196-198.

Wang, J., & Best, P. M. (1992). Inactivation of the sarcoplasmic reticulum calcium channel by protein kinase. *Nature, 359*(6397), 739-741. doi: 10.1038/359739a0

Wang, L., Yang, X., Li, S., Wang, Z., Liu, Y., Feng, J., Zhu, Y., & Shen, Y. (2014). Structural and mechanistic insights into MICU1 regulation of mitochondrial calcium uptake. *EMBO J, 33*(6), 594-604. doi: 10.1002/embj.201386523

Wei, M. C., Zong, W. X., Cheng, E. H., Lindsten, T., Panoutsakopoulou, V., Ross, A. J., Roth, K. A., MacGregor, G. R., Thompson, C. B., & Korsmeyer, S. J. (2001). Proapoptotic BAX and BAK: a requisite gateway to mitochondrial dysfunction and death. *Science, 292*(5517), 727-730. doi: 10.1126/science.1059108

Wishart, D. S., & Sykes, B. D. (1994). Chemical shifts as a tool for structure determination. *Methods Enzymol, 239*, 363-392.

Wittekind, M., & Mueller, L. (1993). HNCACB, a High-Sensitivity 3D NMR Experiment to Correlate Amide-Proton and Nitrogen Resonances with the Alpha- and Beta-Carbon Resonances in Proteins. *Journal of Magnetic Resonance, Series B, 101*(2), 201-205. doi: https://doi.org/10.1006/jmrb.1993.1033

Wright, P. E., & Dyson, H. J. (1999). Intrinsically unstructured proteins: re-assessing the protein structure-function paradigm. *J Mol Biol, 293*(2), 321-331. doi: 10.1006/jmbi.1999.3110

Yoo, J., Wu, M., Yin, Y., Herzik, M. A., Jr., Lander, G. C., & Lee, S. Y. (2018). Cryo-EM structure of a mitochondrial calcium uniporter. *Science, 361*(6401), 506-511. doi: 10.1126/science.aar4056

Zhang, O., Kay, L. E., Olivier, J. P., & Forman-Kay, J. D. (1994). Backbone 1H and 15N resonance assignments of the N-terminal SH3 domain of drk in folded and unfolded states using enhanced-sensitivity pulsed field gradient NMR techniques. *J Biomol NMR, 4*(6), 845-858.

Zhou, Y., Nwokonko, R. M., Cai, X., Loktionova, N. A., Abdulqadir, R., Xin, P., Niemeyer, B. A., Wang, Y., Trebak, M., & Gill, D. L. (2018). Cross-linking of

Orai1 channels by STIM proteins. *Proc Natl Acad Sci U S A, 115*(15), E3398-E3407. doi: 10.1073/pnas.1720810115

Zoratti, M., & Szabo, I. (1995). The mitochondrial permeability transition. *Biochim Biophys Acta, 1241*(2), 139-176.

# Curriculum Vitae

| | |
|---|---|
| **Name:** | Naveed Siddiqui |
| **Post-secondary Education and Degrees:** | University of Toronto<br>Toronto, Ontario, Canada<br>2009-2014 B.Sc.<br>“Biotechnology” and “Cell and Systems Biology” |
| | University of Western Ontario<br>London, Ontario, Canada<br>2016-2018 M.Sc.<br>“Physiology and Pharmacology” |
| **Honours and Awards:** | St. Michael’s College In-Course Scholarship<br>2011-2014 |
| | Dean’s List Scholar<br>2012-2014 |
| | Province of Ontario Graduate Scholarship/QEII-GSST<br>2017-2018 |
| | Western Graduate Research Scholarship<br>2016-2018 |
| **Related Work Experience** | Teaching Assistant<br>University of Western Ontario<br>Physiology 3130z lab<br>2016-2017<br>Cellular Physiology 3140a<br>2017 |
| | Work Study<br>Multi-Organ Transplant Student Research Trainee Program<br>Toronto General Hospital<br>2013-2014 |

**Publications:**

Choi, Y. J., Zhu, J., Chung, S., Siddiqui, N., Feng, Q., & Stathopulos, P. B. (2017). Targeting Cysteine Thiols for in Vitro Site-specific Glycosylation of Recombinant Proteins. *J Vis Exp*(128). doi: 10.3791/56302

Enomoto, M., Nishikawa, T., Siddiqui, N., Chung, S., Ikura, M., & Stathopulos, P. B. (2017). From Stores to Sinks: Structural Mechanisms of Cytosolic Calcium Regulation. *Adv Exp Med Biol*, 981, 215-251. doi: 10.1007/978-3-319-55858-5_10

Dong, Z., Shanmughapriya, S., Tomar, D., Siddiqui, N., Lynch, S., Nemani, N., Breves, S. L., Zhang, X., Tripathi, A., Palaniappan, P., Riitano, M. F., Worth, A. M., Seelam, A., Carvalho, E., Subbiah, R., Jana, F., Soboloff, J., Peng, Y., Cheung, J. Y., Joseph, S. K., Caplan, J., Rajan, S., Stathopulos, P. B., & Madesh, M. (2017). Mitochondrial Ca(2+) Uniporter Is a Mitochondrial Luminal Redox Sensor that Augments MCU Channel Activity. *Mol Cell, 65*(6), 1014-1028 e1017. doi: 10.1016/j.molcel.2017.01.032

**Presentations:**

The 10th Annual Department of Physiology and Pharmacology Research Day, Western University, London, ON, 2016.
Title: Structural basis for mitochondrial calcium uniporter (MCU) interactions with the MCU regulator-1 scaffold factor (MCUR1)

London Health Research Day, London, ON 2016
Title: Structural basis for mitochondrial calcium uniporter (MCU) interactions with the MCU regulator 1 (MCUR1) scaffold factor

Cardiovascular Journal Club, Western University, London ON, 2017
Title: Structural basis for mitochondrial calcium uniporter (MCU) interactions with the MCU regulator 1 (MCUR1) scaffold factor

The 11th Annual Department of Physiology and Pharmacology Research Day, Western University, London, ON, 2017.
Title: The conserved mitochondrial calcium uniporter regulator 1 (MCUR1) matrix domain is a highly alpha-helical trimer sensitive to calcium ions

London Health Research Day, London, ON 2017
Title: The conserved mitochondrial calcium uniporter regulator 1 (MCUR1) matrix domain is a highly alpha-helical homotrimer sensitive to calcium ions